DEVELOPMENT OF OPTICAL FIBER LASER ARRAY METHOD FOR ASSESSING QUALITY OF CHIP PACKAGES

A Thesis
Presented to
The Academic Faculty

By

Aaron M. Mebane

In Partial Fulfillment
Of the Requirement for the Degree
Master of Science in Mechanical Engineering

Georgia Institute of Technology

May, 2018

INSTRUCTIONS: This is a writable pdf file. Use the tab key to navigate through form, and type in information.

GEORGIA INSTITUTE OF TECHNOLOGY
Office of Graduate Studies & Research

CERTIFICATE OF THESIS APPROVAL FOR MASTER STUDENTS

GTID# 903165396

Name: Aaron (First) Michael (Middle) Mebane (Last)

Thesis Title:
Development of optical Fiber Array Method for Assessing Quality of Chip Packages.

We, the below signed, hereby state our full approval of the thesis submitted by the above student in partial fulfillment of the requirements for the degree of Masters in the School/College of Mechanical Engineering

APPROVED BY:

I Ume — Chair, Thesis Reading Committee

Ume — Member, Reading Committee

I Ume — Member, Reading Committee

Akinade — Member, Reading Committee

I Ume — Member, Reading Committee

Sitaraman — Member, Reading Committee

The above named student has completed all departmental requirements and oral presentation, if applicable.

FOR WILLIAM HOFFECK — School Chair/Graduate Coordinator

1/11/18 — Date

* * * \

ACKNOWLEDGEMENTS

There are many people whom I would like to thank for all of their support and encouragement that they gave to me throughout this research project. Most of all to my advisor, Dr. I. Charles Ume, for his guidance and support and for the life experience he has taught me. Additionally, I offer my most sincere gratitude to my reading committee Dr. Kola Akinade and Dr. Suresh Sitaraman. I also would like to thank the former and current members of the Laser Ultrasonic Research Lab at Georgia Tech without which these advancements would not be possible.

My gratitude to Dr. Kola, Bryan, Mark, and all the people at CISCO for their support, suggestions, and assistance, without them this research would not have been possible.

A large portion of the improvements to the system would not have been possible without the resources of the Department of Mechanical Engineering machine shop and the people therein. I am especially thankful to Nathan, Frank, and Louie for their training and suggestions.

To my parents who have always encouraged my love of building things and who have supplied me with the upbringing that has carried me throughout my life and academic career. And for wonderful fiancée, Clarisse, whose incredible love and support has meant more to me than I can possibly convey. I am forever grateful.

This work was supported under the National Science Foundation award number 1536342. Any opinions, findings, conclusions, or recommendations in this thesis are those of the author and do not necessarily reflect the views of the National Science Foundation.

TABLE OF CONTENTS

LIST OF TABLES

LIST OF FIGURES

SUMMARY

The long term goal of this research is to assist in the development of a fast, robust, low-cost, non-contact, nondestructive system for the inspection of solder joints in microelectronic chip packages. The goal of the work described in this thesis is to develop a dual fiber array system for delivery of the excitation laser from its source to the chip package under inspection. The dual fiber array is important because it allows greater laser energies to be used in the inspections - resulting in a stronger vibrational response of the chip package. This allows the system to inspect larger packages, as well as those with greater density of solder joints, without the need to subdivide the package into smaller subsections. Additionally, splitting of laser energy into two beams allows optical fibers with smaller core diameters to be used in the laser delivery system. Smaller core diameters correlate to decreased minimum fiber bend radii, and therefore construction of a more compact system is possible. As part of the upgraded laser delivery system, new adjustable end effectors (which collimate and focus the laser exiting the fiber) were implemented which allow greater control over the excitation spot size. With the addition of the improvements described in this work, the system was able to inspect a large chip package that could not be inspected by a system with a single excitation point.

A number of new hardware and software safety features were also implemented, as well as program modifications to fix a number of issues found in the system's operation. A Hall Effect sensor base proximity detector was devised and affixed to the interferometer probe. This measures the strength of the magnetic field produced by an

array of magnets on the laser positioning stage. If the magnetic field exceeds a set threshold (because the laser positioning stage has moved too close the interferometer probe and a crash is imminent), power will be cut to the system by means of a relay. In addition, a new stage homing routine was written to reduce the likelihood that circumstances leading to a collision will occur.

An array of tests was conducted to evaluate the improvements to the system. Tests showed that the dual fiber system could indeed generate stronger ultrasounds than its single fiber predecessor, leading to the ability to inspect larger chip packages. Repeatability experiments were conducted, and after an issue with the preloading in the positioning stage's bearings was fixed, the system showed good repeatability. In addition, small package sizes might benefit from using a single excitation point rather than the two points the new system was designed for. Therefore, experiments were undertaken to show that overlapping the excitation points (one from each fiber) was equivalent to a single point generated from a single beam. This was successfully shown.

CHAPTER 1
INTRODUCTION

1.1 Trends in Microelectronics

Since the advent of the first transistor at Bell Labs in 1948 the semiconductor industry has grown to touch almost every aspect of modern day life. One of the main uses of semiconductors is to build up integrated circuits (IC). ICs, which can incorporate both active components (transistors and diodes) and passive components (capacitors and resistors) onto a single silicon die, form the brains of all smart electronics ranging from singing birthday cards to super computers. IC packaging is the interface that combines IC and other components into a single, ready to use package that is used to form electrical products [1]. This packaging provides the electrical pathways to connect to the outside world as well as improved thermal and mechanical properties [2]. One of the first of the packages was the dual in-line package, or DIP, which had the external connections in the form of pins lining opposite sides of the package. As seen in Figure 1.1, these packages consisted of the active device (i.e. die) embedded in a plastic or epoxy compound and wired to a lead-frame which facilitated the external connections to the printed circuit board (PCB). In the 1980s a transition was made to quad flat pack (QFP) and small-outline integrated circuit (SOIC) packages. These surface mount devices (SMD) improved the electrical performance and increased the density of packages per PCB which lead to their widespread use [3]. Examples of these two types of packages can be seen in Figures 1.2 and 1.3.

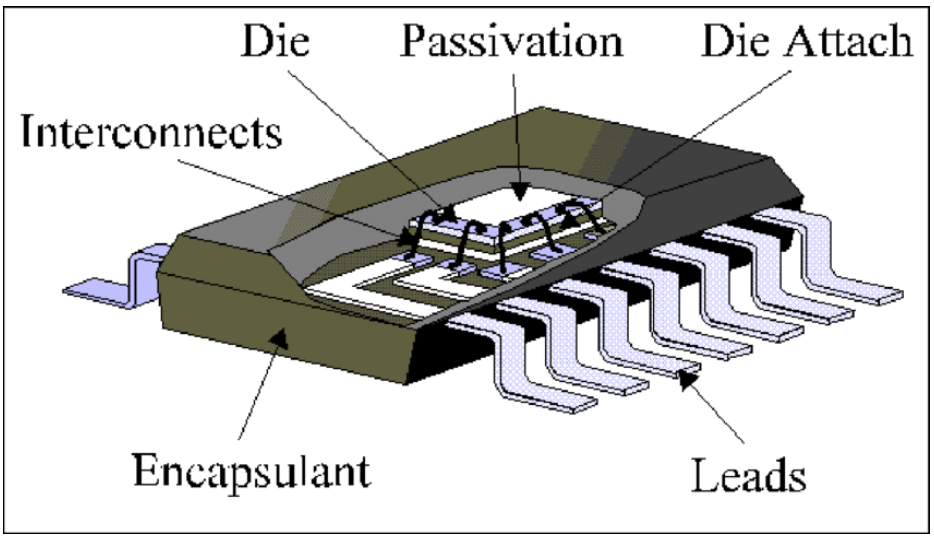

Figure 1.1: Cutaway view of an IC package showing the die, interconnects (wire bonding) and lead-frame. (Source: Engineering Magazine)

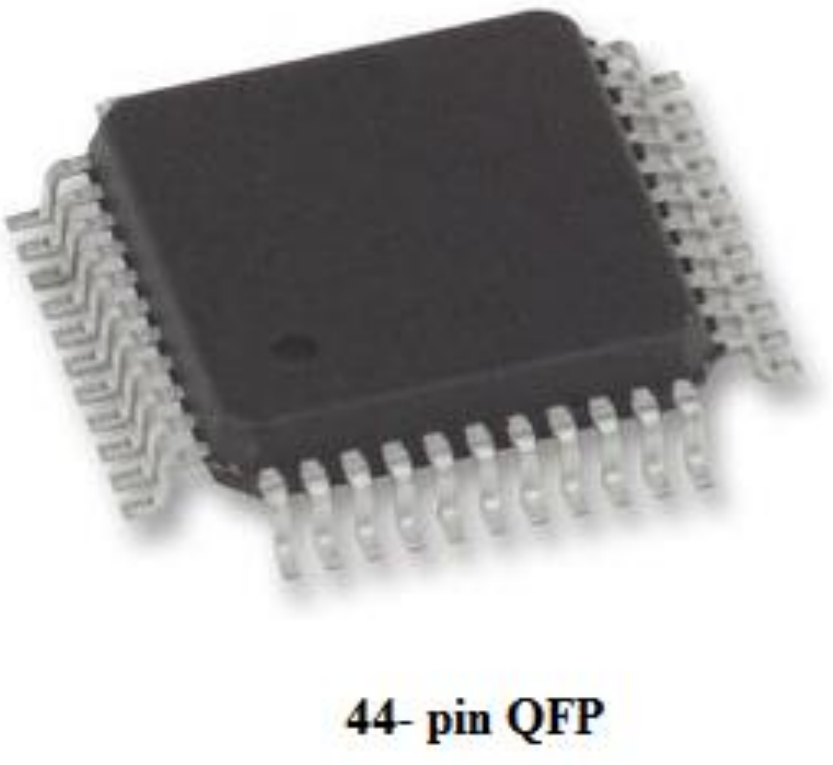

Figure 1.2: Image of a QFP. (Source: OurPCB)

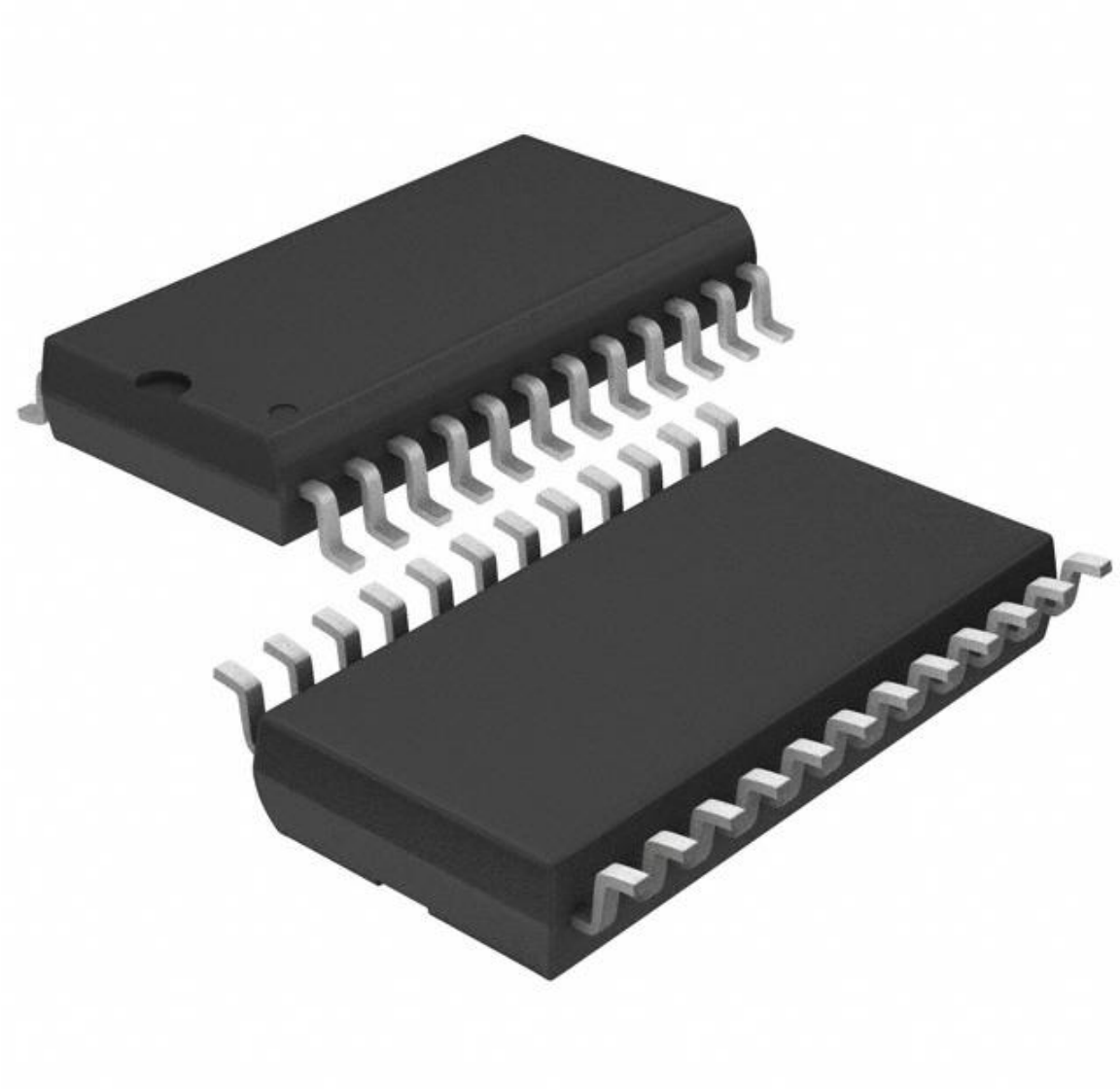

Figure 1.3: Image of SOIC package (Source: DigiKey)

However, these advances were still not enough for demands of the modern world. The long signal pathways of these packages limited the maximum signal speeds while the large amount of encapsulant impeded proper thermal management, thus making the form factor impractical for the emerging handheld electronics market. Additionally, the use of device-to-board connections along only two sides of the chip, as for DIP packages, or

along the four sides, as in QFP packages, left large amounts of space underneath the chip unutilized. Therefore, an area array type package was invented, of which the ball grid array (BGA) is the most notable. In the BGA, Figure 1.4, instead of the wire-bonding going to leads along the sides of the package, connections are made to an array of solder balls on the underside of an interface layer called the interposer. Even with BGA packages, however, the ratio of die to package area was still inadequate so further advancements were desired. Thus the flip chip (FC) and chip-scale packages (CSP) entered the scene.

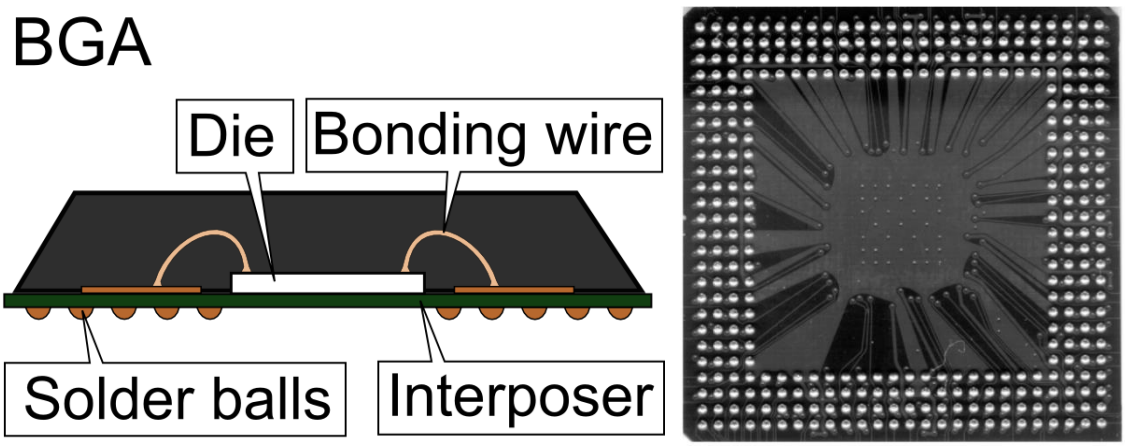

Figure 1.4: Left, Cut-away side view of a BGA package showing the internal die and wire connections. Source: Tosaka. Right, view of the underside of a BGA package. The array of gray solder balls is clearly seen (Source: Texas Instruments).

FC technology was first successfully developed by IBM and is a descriptive term which indicates how the die is connected to the package substrate. Previously, packages such as SOICs and QFP used a wire-bonded method, in which the pads on the die are placed facing up and small wires are used to make the electrical connections to the carrier

package. In contrast, as seen in Figure 1.5, for FC technology solder bumps are deposited on the die's I/O pads and the die is flipped over active side down on either a carrier package or PCB directly. The assembly is then passed through a reflow oven to melt the solder, providing a secure electrical connection. An example of a FC inside a carrier BGA package is shown in Figure 1.5. When the FC is directly attached to the PCB it is more properly known as direct chip attach (DCA) [4].

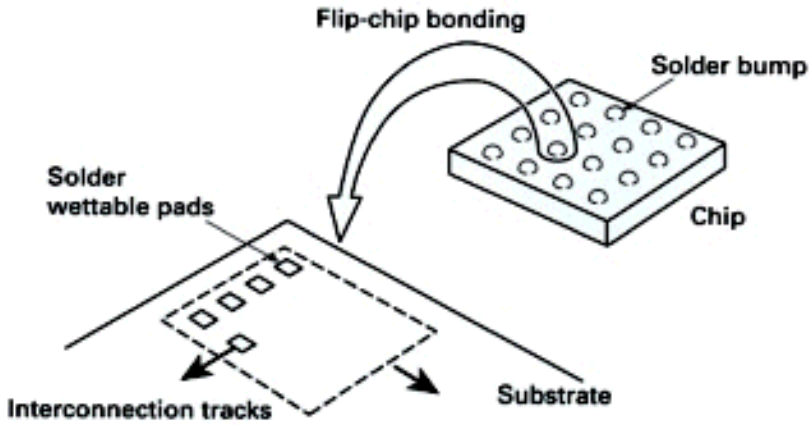

Figure 1.5: Flip chip with solder bumps being placed on substrate (Source: TWI)

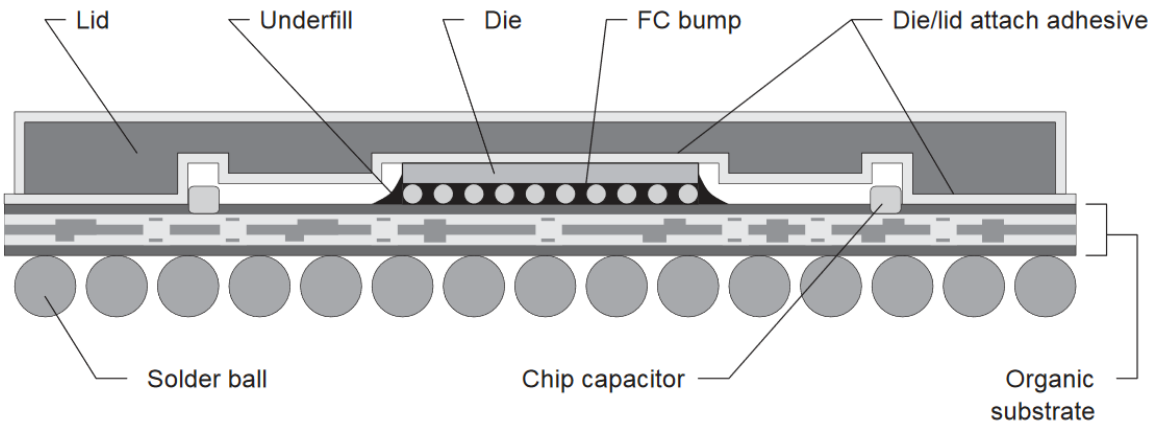

Figure 1.6: A cutaway showing the FC inside a BGA package. Note the bumps used on the underside of the die instead of wire-bonding (Source: Texas Instruments).

With these advances, however, came the problem of coefficient of thermal expansion (CTE) mismatch. Because of the differences in materials used for the die and substrate, and the high temperatures needed to melt the solder, there is significate stress developed when the device cools. This can lead to crack formation in the solder connections and a defective/reduced device life. The developers at IBM originally used only small chips, fatigue resistant solder, and ceramic substrates to minimize the problem with CTE mismatch [5]. While this method proved to be quite reliable, many of today's applications of DCAs use alternative substrate materials which increase the CTE mismatch and result in a much lower reliability of the solder joint due to the increased stresses developed. To help mitigate this problem and improve solder joint longevity, an adhesive underfill, usually epoxy acid anhydride based [6], is injected into the space between the die and the substrate.

CSP is a form of packaging that provides all the basic functions of IC packaging in a size as small as 1.2 times that of the die itself [7]. Wafer level chip scale packages

(WLCSP) are true chip scale packages, where the finished device is the same size as the wafer itself [8]. One difference between WLCSPs and other CSPs is that WLCSPs are processed almost entirely before the wafers are diced, as opposed to normal CSPs. The minimal package design cuts down on manufacturing costs and has many of the benefits of FCs such as high I/O density, excellent electrical characteristics, small size, and low weight. FC and WLCSP are so similar, in fact, that sometimes the names are used interchangeably [9]. The major difference is that FCs typically use greater solder ball pitches and larger solder balls to lessen the problems of excess stress and as such greatly reduce the need for underfill [9].

With the maturing of smartphones and the explosive growth of the Internet of Things (IoT), manufactures are ever being pushed to create smaller, more reliable packages [10]. One of the responses to these demands is the development of 2.5D and 3D chip technology. As shown in Figure 1.6, 2.5D technology combines multiple dies in the same package by stacking the dies on an interposer layer which interconnects the dies together and provides the pathways to the lowest level of the package with the connections to the board [11].

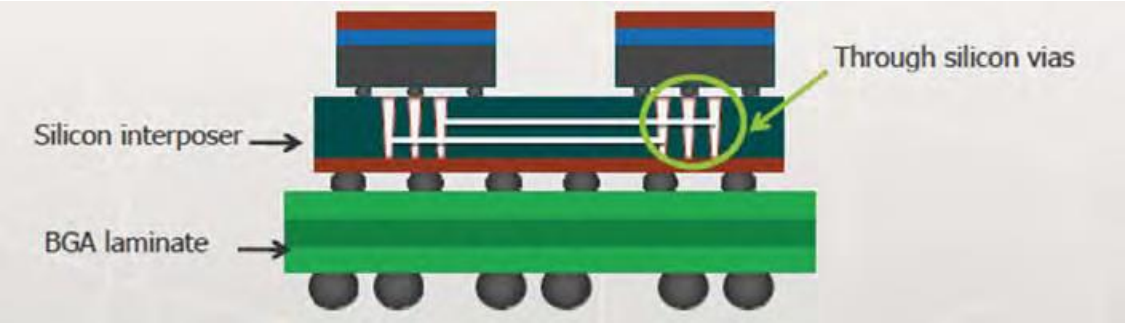

Figure 1.7: 2.5D technology allows multiple dies to be integrated together into a single package by means of an interposer layer (Source Mentor Graphics).

As shown in Figure 1.7, 3D technology takes this a step further by stacking the silicon wafers themselves on top of each other, grinding off the excess silicon, and providing a means of interconnection between them, such as silicon side-through, through-hole, and interposer [12 – 17].

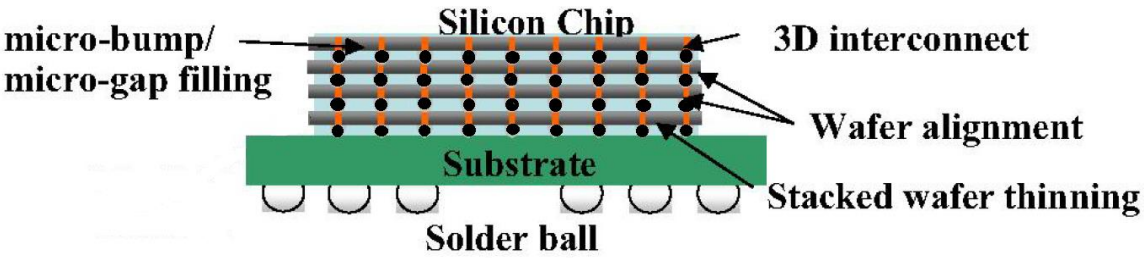

Figure 1.8: Diagram of 3D IC made up of stacked silicon wafers (Source: ITRI).

2.5D and 3D chip technology offer many benefits over traditional packaging such as a dramatic increase in space efficiency and reduced power consumption [12]. As consumers continue to demand devices of ever increasing power and functionality, 3D chip technology will only continue to grow and develop.

1.2 Solder joint Reliability

While IC packages that use solder balls as the means to connect the active device to the PCB have many important advantages over the older lead-frame technology, there remain serious concerns, such as solder joint defects and thermomechanical reliability.

The large temperature range experienced by the PCB and device during the reflow soldering process causes both the device and PCB to expand. Once out of the reflow oven, the solder quickly solidifies, locking the PCB and device together. As the assembly cools further a large amount of strain can develop in the solder balls due to coefficient of thermal expansion (CTE) mismatch between the PCB and device. This can lead to defects such as cracks and laminate separation [18].

As IC technology advances and packages continue to shrink and as active component density increases, reliable chip-to-PCB solder connections become more difficult to achieve. In addition, the increase in active component density leads to greater heating of the device during use and as a result increased stress due to thermal loading. Given these challenges, many prevalent processing defects and field failure modes for devices using wafer-level packages are related to the solder joint interconnections.

There is data to suggest that 40% of all PCB/IC assembly defects are related to the soldering [19]. As such, it is imperative to monitor the solder joint quality during the assembly process. Consumers demand reliable, long-lived devices, and therefore device manufacturers have a great need for reliable inspection methods and tools to not only find solder joint faults as early in the manufacturing process as possible, but also to detect defects to prevent premature device failure once the product has been sold. Some of these inspection techniques will be discussed in the following sections.

1.3 Solder joint inspection techniques

1.3.1 Visual Testing

Visual testing of microelectronic chip packages uses optical wavelengths to examine the solder joints by either computer or manual techniques. As shown in Figure 1.8, one such technique uses a domed shaped LED ring to illuminate the solder joint while a 3 charge-coupled devices (CCD) camera takes in the reflected light. The data is processed using a neural network combined with a genetic algorithm to extract the features of the solder connection and compare them to a set of input features. This method has proven successful in recognizing good solder joints, insufficient solder, cold solder joints, and component misalignment [20]. However, this method is limited by the need to have a direct line of sight to the solder joint under examination and therefore cannot be used with flip chip (FC) and ball grid array (BGA) type packages. Endoscopy is a method that has been tried for these types of microelectronic packages; however, this is only useful for peripheral solder balls. As such, visual testing is of limited use in the inspection of FC and BGA solder balls.

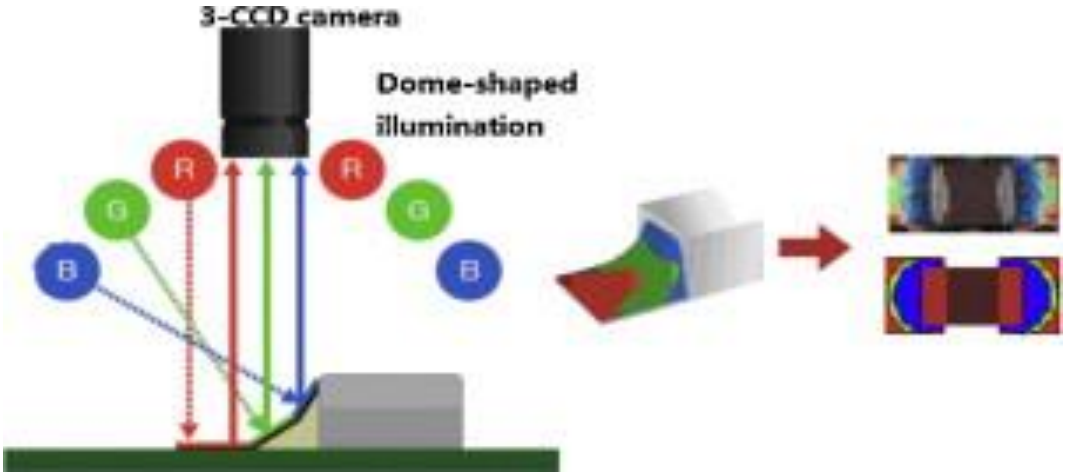

Figure 1.9: Visual Inspection of the solder joint of surface mount capacitor

1.3.2 Electrical Testing

At the basic level, electrical testing involves electrically probing the device under test (DUT) and measuring the response. The response for a particular stimulus is compared to the expected range of responses and any device with a response outside this range is deemed defective.

Electrical testing can be broken down into two main methods: functional testing and in-circuit testing. Functional testing, as the name implies, consists of testing the operation of every function of the device while under all reasonable environmental variations, and the device must be confirmed to operate as expected. The limitation of this form of testing is that normally the failure site and mode cannot be determined. Moreover, defects that can shorten the life of the device but do not render it immediately inoperable (such as small cracks) cannot be detected by this method. In-circuit testing, i.e. “bed-of-nails” testing, evaluates the DUT from a circuit perspective rather than an operational one. As seen in Figure 1.10, in this test contact is made with conductive pads

on the substrate, which are electrically connected to different parts of the DUT. A stimulus is applied and the response measured, usually in the form of a resistance or capacitance. This is compared to the expected range of values and a pass or fail assigned. The advantage of in-circuit testing is that the circuit of the DUT can be broken down into smaller subdivisions that are tested so as to isolate the region where the defect resides. The disadvantages are that the test pads can use a significant amount of board space, and that failure modes such as poor wetting and bridging cannot be detected.

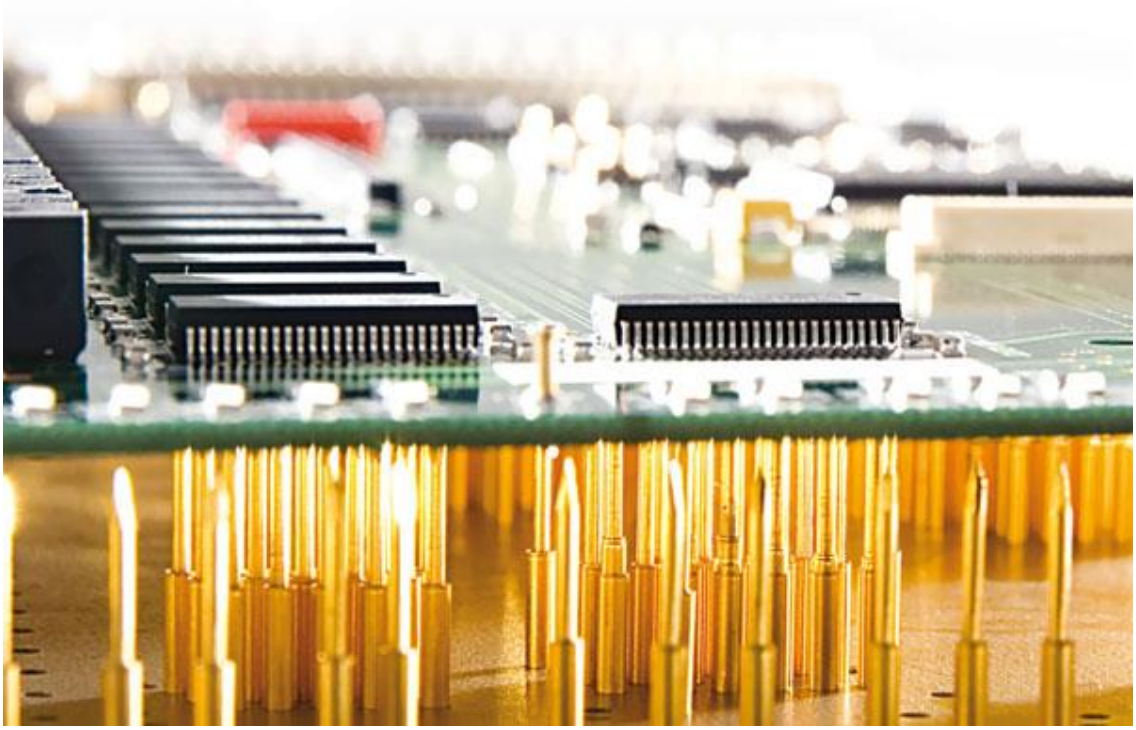

Figure 1.10: PCB atop the conductive probes of a bed-of-nails test equipment (Source: SPEA)

1.3.3 X-Ray Inspection

X-rays have been used extensively for imaging and inspection ever since their discovery in 1895. First used mainly in the medical realm, in the past decades they have become invaluable in the field of microelectronic inspection. X-rays are electromagnetic waves which occupy the 30 petahertz to 30 exahertz part of the electromagnetic frequency spectrum. Their short wavelengths of between 0.01nm – 10nm make them able to penetrate most materials. While many factors such as x-ray flux and distance between sample and source can affect the resolution of x-ray inspection, resolution in the 1~2um range is common. A typical x-ray system consists of an x-ray source, which generates the x-rays by means of the Bremsstrahlung effect, a detector to convert the x-rays to visible light, and a camera to capture the light which becomes the final result. The different properties of the materials in the sample under inspection (SUI) cause the x-rays to be absorbed by differing amounts; higher density materials typically absorb more x-rays than less dense materials. This leads to an image of the sample showing the absorption pattern being produced. The three x-ray inspection methods are: radiography, laminography, and tomography and each has its own advantages and disadvantages.

Radiography produces the 2D x-ray images that are most commonly thought of when the average person thinks of an x-ray. As shown in Figure 1.11, the SUI is placed between stationary x-ray source and detector. This produces a grayscale absorption image for the sample as a whole without regard to spatial details along the source to detector axis. An example of a 2D image of a BGA package taken with such a method is shown in Figure 1.12.

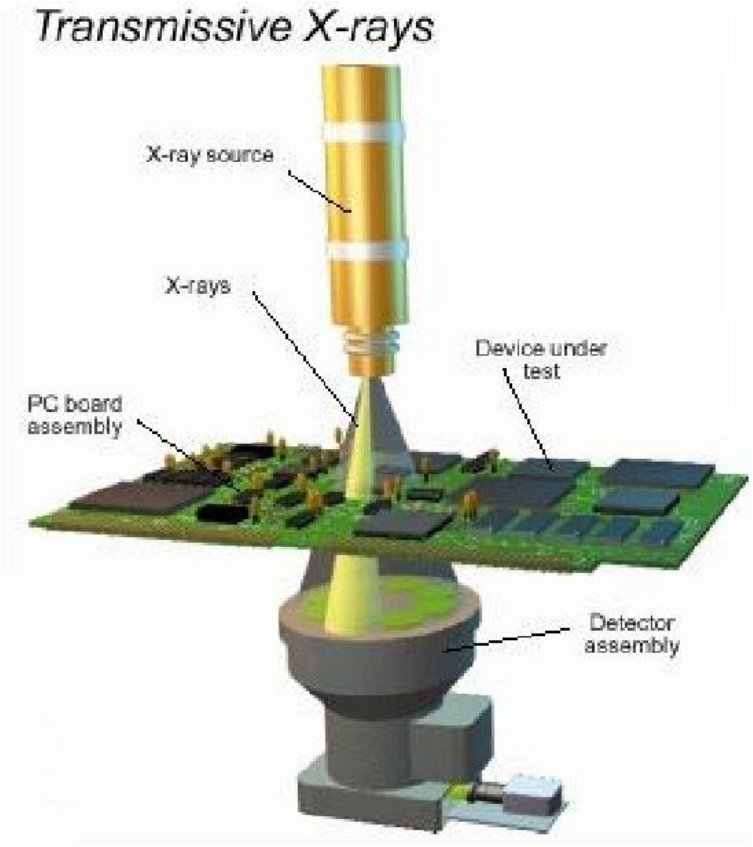

Figure 1.11: X-ray radiography (Source: Machinedesign®)

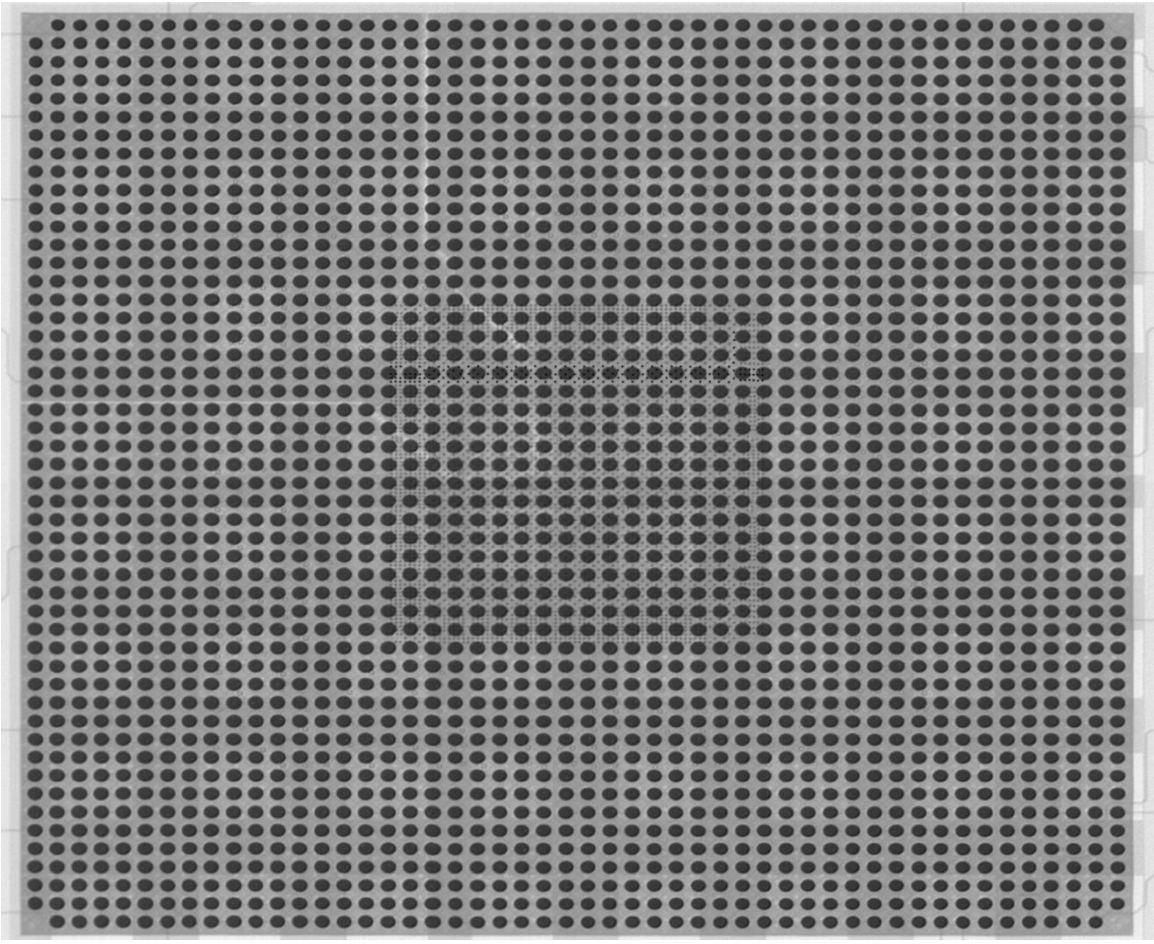

Figure 1.12: 2D X-ray image of BGA chip package. The black circles are the solder balls.

X-ray radiography has been successful in detecting the presence of voids, solder bridges, missing solder balls, solder ball misalignment, and missing or broken internal connections. One of the main disadvantages of 2D x-ray radiography is that other components on the board can absorb the x-rays thus casting a shadow over the point of interest. In addition, depending on the orientation of cracks in the solder balls, the cracks can remain invisible to 2D radiography because the amount of material that is absorbing the x-rays does not change.

Laminography is a combination of two Latin words *lamina* meaning “a thin layer”, and *graphia* meaning “to write” or “recording of instrument measurements”. In this technique the x-ray source and detector are moved in opposite circular patterns while the sample of interest remains at rest. In doing so, the layer in the sample (known as the focal plane) is projected at the same position on the detector and therefore remains in sharp focus while the rest of the layers in the sample are blurred. The concept is shown in Figure 1.13. Originally, when film was used, only one plane could be imaged at a time. With the advent of digital flat panel detectors many different images can be can be captured during the same scan and then superimposed on each other to blur out all but one layer of the sample. By applying the appropriate shift before superimposing the images, different layers can be brought into relief. These can then be combined to construct a 3D image of the sample. An example of an image produced by this technique is shown in Figure 1.14. The main drawbacks of this technique are low spatial resolution [21] and the high equipment and operational costs.

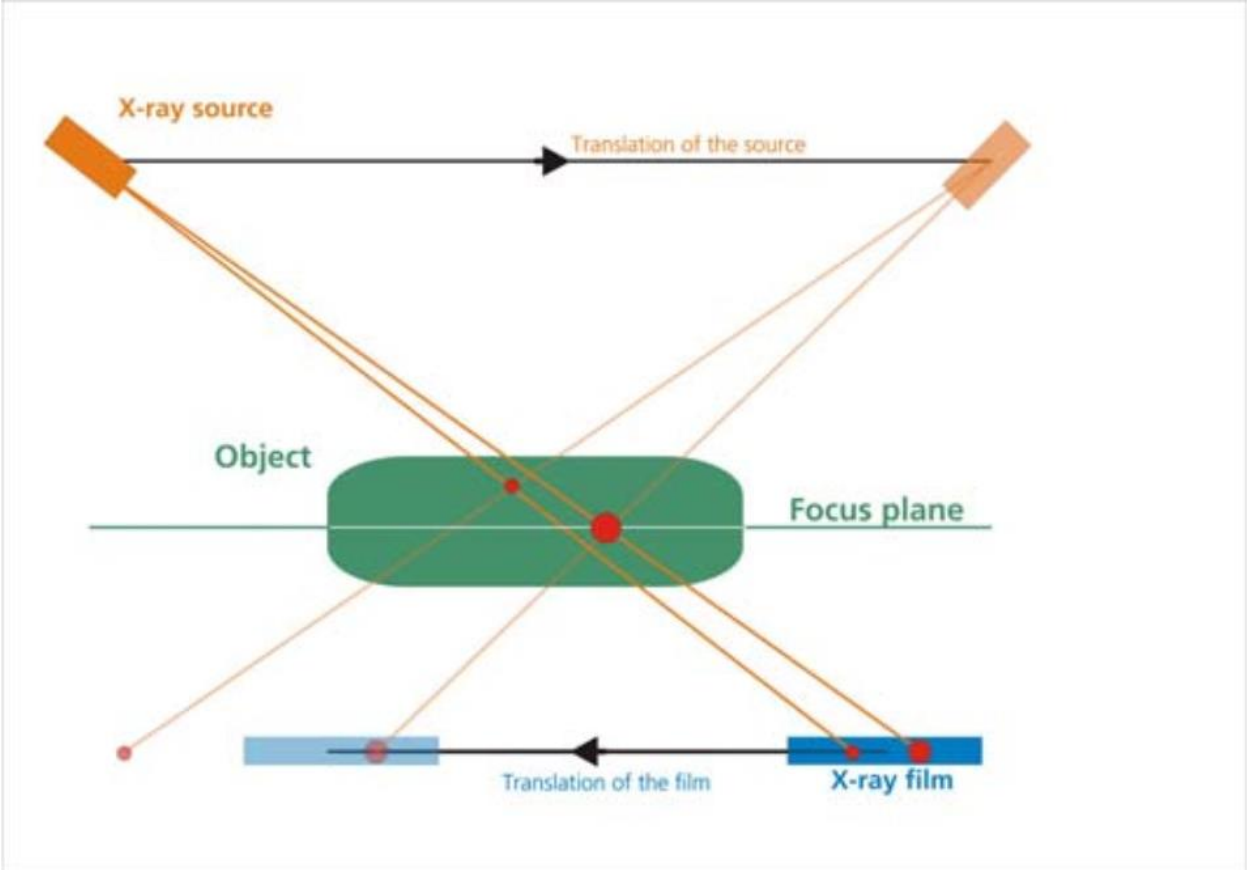

Figure 1.13: Principle of laminography technique. (Source: [21])

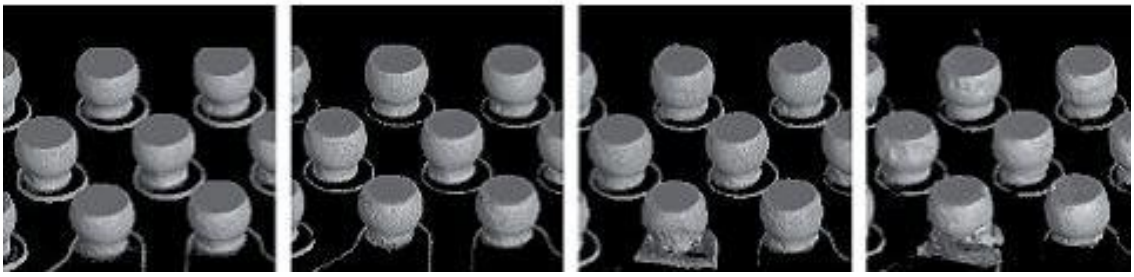
Figure 1.14: X-ray laminography of solder balls at different stages in their life (Source: Karlsruhe Institute of Technology)

As shown in Figure 1.15, X-Ray tomography generates a 3D image by taking multiple captures as the DUI rotates between the X-Ray source and detector. The

individual 2D images are then computationally stitched together. The result is a 3D image that can be virtually cross-sectioned to reveal any defects.

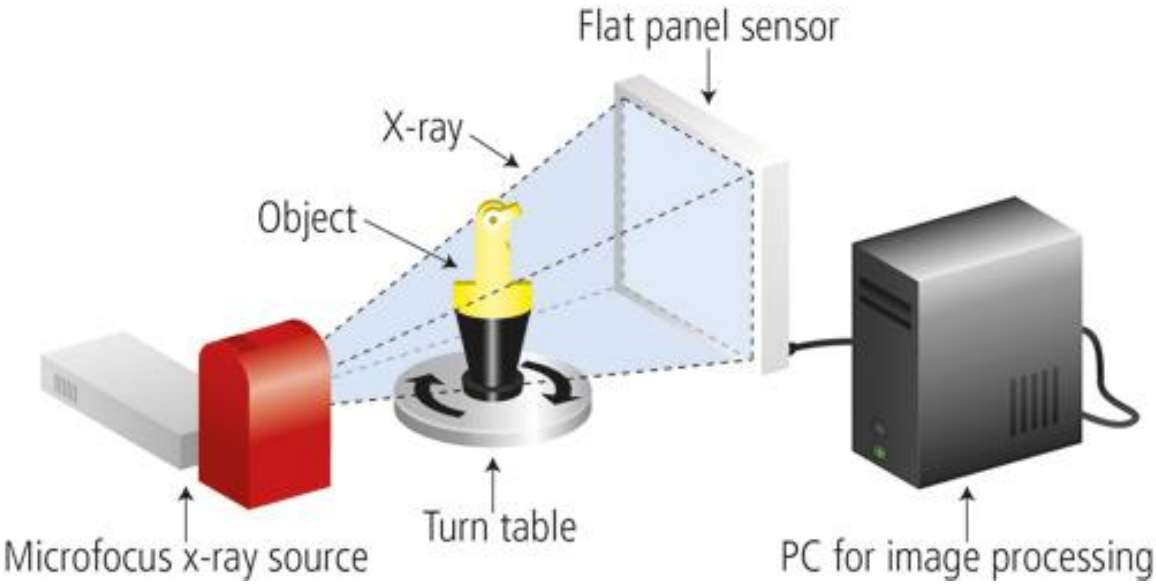

Figure 1.15: Principle of X-Ray tomography (Source: Hamamatsu Photonics)

Figure 1.16 shows the 3D image produced from X-Ray tomography. In it one can clearly see the solder bridge. X-Ray tomography is very powerful technique that is theoretically capable of inspecting all types of solder joint/solder bump defects. Practically, sometimes it can be very difficult to interpret the images. Due to the necessity to rotate the sample during the inspection process, it is difficult to inspect large and/or complex boards. Additionally, because of the time required for data acquisition and processing, it is considered unsuitable for online applications. Advances in computer processing power and image reconstruction techniques are helping to alleviate these

impediments to a degree. However, initial investment and operational costs for X-Ray tomography systems remain prohibitive.

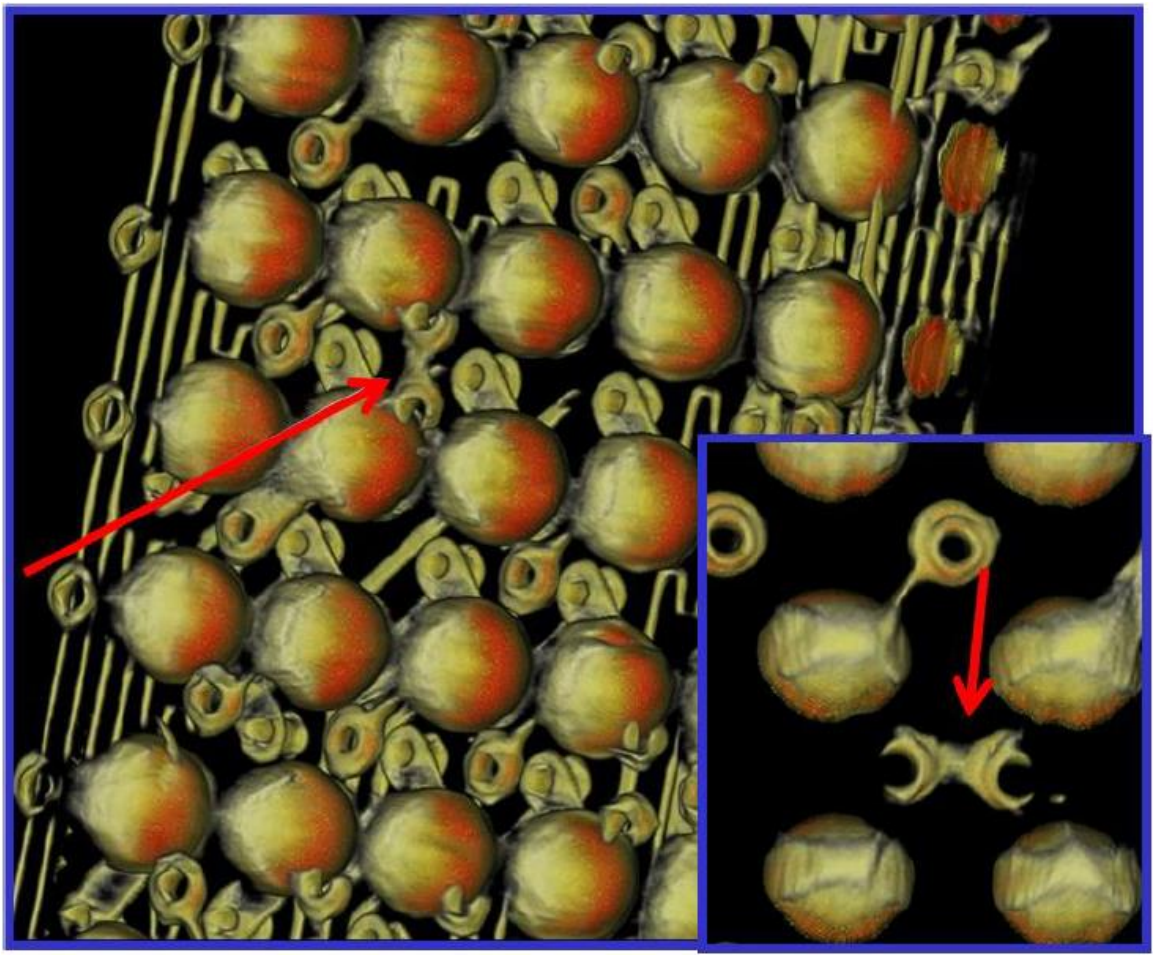

Figure 1.16: X-Ray tomography image showing solder bridge [22]

1.3.4 Scanning Acoustic Microcopy (SAM)

Acoustic inspection is a widely used technique for the non-destructive evaluation of microelectronic chip packages. In this technique, a high frequency ultrasonic pulse is generated by means of a piezoelectric transducer and focused down on the DUI. Depending on the operating mode, either the reflected or transmitted signal is detected by and information about the internal structure of the DUI is extracted. The working principle is that the propagation and reflection of the acoustic waves will be altered at the interface of two materials with different acoustic impedances (e.g. substrate to solder bump, solder bump to air, etc.). This makes acoustic inspection extremely useful for the detection of defects such as cracking, voids, and/or delamination. When one of these defects forms, the open space is filled with air. The acoustic impedance of air increases with the frequency of the ultrasound; above ~10MHz the acoustic impedance is such that the ultrasounds cannot propagate.

Scanning acoustic microscopy (SAM) is an acoustic technique in which the ultrasonic point source is moved across the surface of a sample while either the reflected or transmitted wave is captured. This scanning motion allows data from the entire area of the DUI to be taken. Typical operating frequencies range from 10MHz to 2GHz.

There are several different operating modes of SAM. If the same transducer is used to capture the reflected wave, the imaging mode is known as pulse-echo mode. If a separate transducer, opposite the DUI, is used to capture the transmitted wave the imaging mode is known as transmission mode. C-mode SAM (CSAM) is the most commonly form of SAM and can be conducted in pulse-echo or transmission mode,

pulse-echo mode being the most commonly used. In this form of CSAM, images are formed by capturing the acoustic wave reflected from a certain depth within the DUI. Figure 1.17 shows a typical setup of a CSAM system. Any defect in the DUI, such as a crack, void, or delamination, reflects a different echo than would otherwise be expected. The amplitude of the reflected signal is proportional to the difference in the acoustic impedance between the defect and the adjacent material.

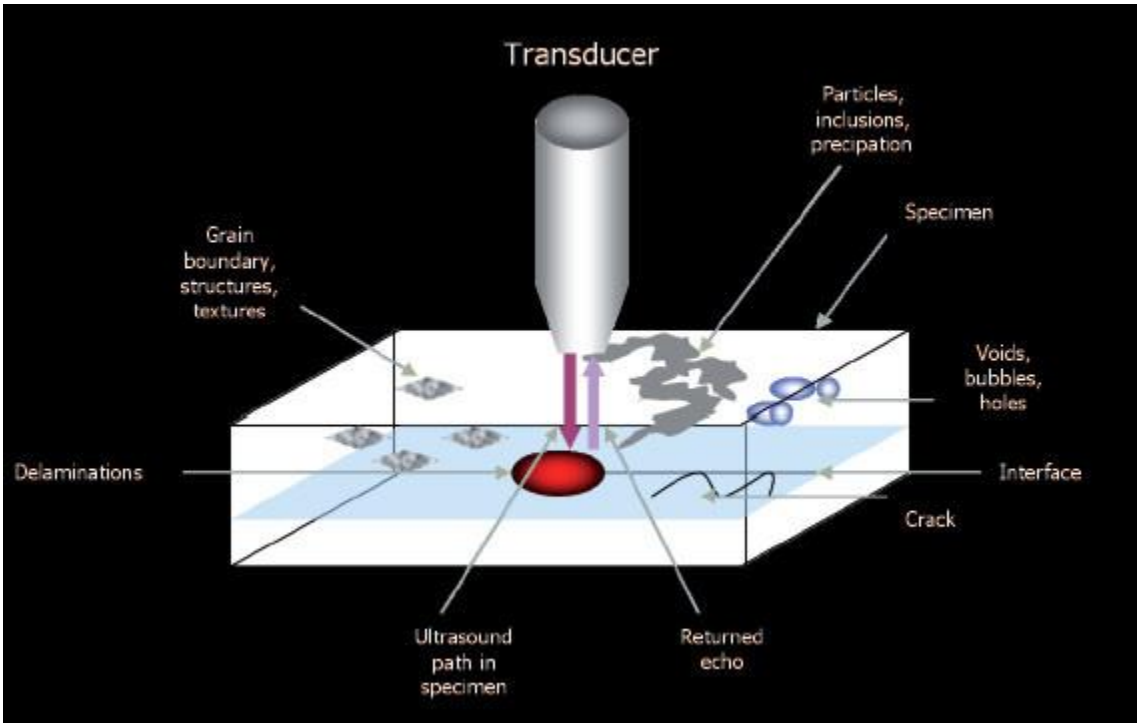

Figure 1.17:Diagram of CSAM (Source: KSI)

As useful as it is, CSAM has many limitations. Because of its principle of operation, only interfacial defects, such as the aforementioned cracks, voids, and delamination can be detected. Additionally, effects such as frequency downshifting can significantly reduce the detection resolution [23]. Frequency downshifting is the

phenomenon in which the peak of the frequency bell curve is shifted towards the lower frequencies due to the fact that attenuation increases proportional to frequency. Edge effects also cause a decrease in measurement resolution along the edge of the DUI [24]. As seen in Figure 1.18, this is due to the ultrasonic wave being scattered. Another downside is that the DUI must always be submersed in a coupling medium - usually deionized water.

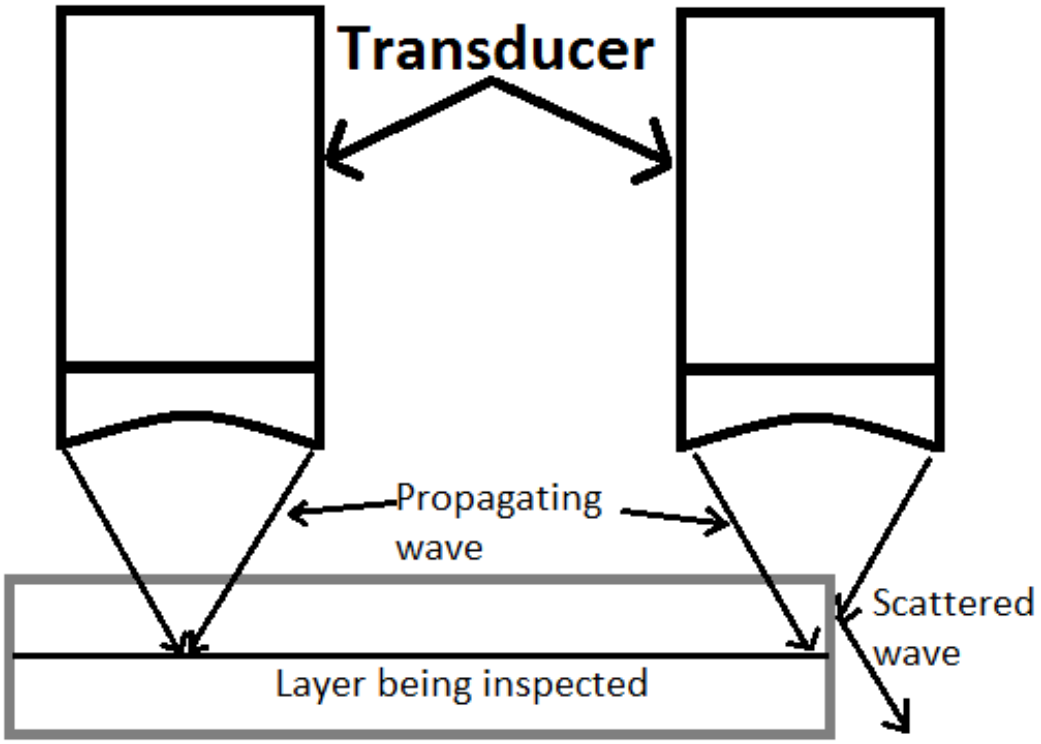

Figure 1.18: Schematic diagram showing how edge effects occur

If an additional transducer is placed opposite the DUI (relative to the ultrasonic source) and used as a receiver, a transmission image can be produced. This technique is known as through scanning acoustic microscopy (TSAM). The images produced are of the absorption of the ultrasonic wave as it passes through the sample, similar to how 2D

x-ray radiography works. While TSAM is simpler than CSAM, it produces lower resolution images and cannot provide any information about the depth of the defect.

There are 2 main parameters used to characterize an ultrasonic transducer: depth of field and resolution. Depth of field refers to the effective depth of penetration of the ultrasonic signal. Resolution refers to the minimum size of defect that can be resolved. Equation 1 describes the relationship between resolution and frequency, while Equation 2 shows the relationship between depth of field and frequency. It is seen that resolution can be improved with an increase in frequency. However, an increase in transducer frequency leads to a corresponding decrease in penetration depth. Table 1.1 lists some calculated resolutions and penetration depths for an assortment of transducer frequencies.

$$Resolution = 0.707 * 1.22F^{\#}\lambda \quad (1)$$

$$Depth\ of\ field = 7.1(F^{\#})^2\lambda \quad (2)$$

where $F^{\#} = \frac{Focal\ length}{Diameter}$ and $\lambda = \frac{Velocity}{Frequency}$ in mm.

Table 1.1: Resolution and depth of field for a range of transducer frequencies

Frequency (MHz)	$F^{\#}$	**Resolution (microns)**	**Depth of field (mm)**
50	2	50.6	0.833
100	2	25.3	0.416
150	2	16.9	0.278
200	2	12.6	0.208

Therefore, it can be seen that SAM has limited use for the inspection of solder joints in thick packages. As noted previously, higher frequency ultrasounds are attenuated

more rapidly than lower frequency. This leads to a decrease in resolution the deeper the signal propagates into the DUI. Consequently, defects deep within the DUI might not be detected. Additionally, the orientation of the defect can impact its detectability. For example, a crack that runs perpendicular to the transducer axis might be able to be detected while the same size crack running parallel to the axis might be completely missed. As such, SAM of BGA packages is limited to detection of failures isolated in the upper regions of the package such as popcorn failures [25] and die interfacial delamination [26].

1.4 Laser Ultrasonic Inspection System

In this system a Q-switched laser operating in the thermoelastic regime, so as to not cause damage, is made incident on the surface of a microelectronic chip package. This nano-second laser pulse flash heats the chip material at the incident point causing rapid expansion. This induces vibrations in the material around the excitation point, which radiate outward through the material as both transverse and longitudinal waves. Any boundary encountered by the waves will augment the wave by either transmitting or reflecting it. When that boundary is air (such as at the edge of the chip) very little of the wave's energy can be transmitted, and therefore it is almost entirely reflected back into the chip, resulting in a mixing of the transverse and longitudinal waves. This mixing is known as mode conversion. All of these reflections and transmissions interact with each other constructively and destructively to transfer energy into the normal vibrational modes of the chip. In this laser ultrasonic inspection (LUI) system, the transient out-of-

plane vibrations resulting from these vibrational modes are measured using a laser Doppler vibrometer. The signal acquired from the DUI is compared to a reference signal from a known good chip. Any defects in the solder joints such as cracks, delamination, missing balls, voids, etc. alter the vibrational response of the chip and therefore can be detected and/or categorized by analysis of the measured response.

One of the important methods of comparing the signal from the DUI to the reference is the modified correlation coefficient (MCC) [27]. Equation 3 shows how the MCC value is calculated

$$MCC = 1 - \left(\frac{\sum_n (R_n - \bar{R})(A_n - \bar{A})}{\sqrt{(\sum_n (R_n - \bar{R})^2)(\sum (A_n - \bar{A})^2)}} \right)^2 \quad (3)$$

where R_n is the reference signal, $\bar{R}$ is the average value of R_n, A_n is the signal of interest, and $\bar{A}$ is the average of A_n. An MCC of 0 means there is complete correlation between the two signals; therefore the DUI is good. An MCC of 1 indicates the signals are complete inverses of each other and therefore indicates dissimilarities between the chips. Due to manufacturing variations and the limitations in the system (i.e. limited accuracy of the positioning stages, etc.) the MCC value will never reach the perfect correlation value of 0 even for two good chips.

Figure 1.19 shows the basic operational principle of the LUI system as well as an example time-domain signal. The research presented in this thesis is based on laser ultrasonic generation and detection techniques.

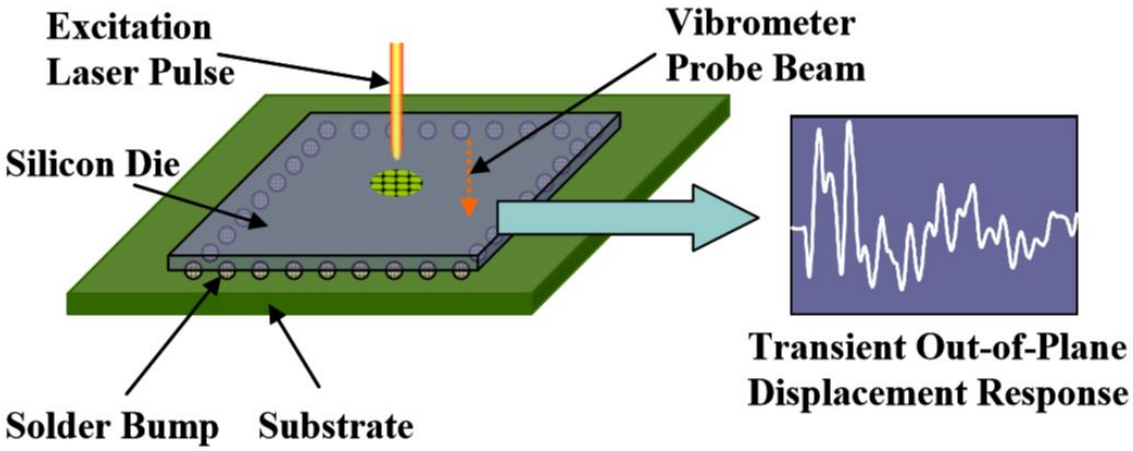

Figure 1.19: Operating principle of laser ultrasonic inspection.

Previous work on this system has shown successful application to the detection of solder joint defects such as misaligned, open, missing, and cracked solder joints in land grid array (LGA) packages [29]. Another study used the system to study the reliability of FC solder balls undergoing accelerated thermal cycling [30], and other work effectively detected the presence of poor wetting and voids [7]. Table 1.2 shows a comparison between different non-destructive solder joint/bump inspection methods. This comparison shows the uniqueness and robustness of the LUI inspection method.

Table 1.2: Comparison of different non-destructive inspection methods.

Features			Laser Ultrasound	Electrical Test	X-Ray		Acoustic Inspection
					2D X-Ray	3D X-Ray	
Contact/Non-contact			Non-contact	Contact via test pads	Non-contact	Non-contact	Contact (immersed in water)
Throughput							
Cost			$200K	Low	$150K - $250K	$350K - $500K	$200K – $250K
Resolution			Has been used to detect presence of micro-cracks	Low	1-2 microns	1-2 microns	Resolution increases with frequency of ultrasonic transducer at expense of penetration depth
Capabilities	Silicon die defects		Yes	Yes	Yes	Yes	Yes
	Interlayer delamination		Yes	No	No	Yes	Yes
	Solder bump defects	Missing	Yes	Yes	Yes	Yes	Yes
		Misaligned	Yes	No	Yes	Yes	No
		Cracks	Yes	No	No	Yes	No
		Open	Yes	Yes	No	Yes	Yes
		Voids	Yes	No	Yes	Yes	No
	Package Types	FCP	Yes	Yes	Can apply to various package types, however, it's difficult to interpret images of multilayered or double-sided samples	Test chamber has a very limited space (typically 2 – 3 in), unsuitable for samples with large dimensions or complicated geometry	Incapable of inspecting packages with large thickness because of lack of penetration
		CSP	Yes	Yes			
		LGA	Yes	Yes			
		BGA	Yes	Yes			
		MLCC	Yes	Yes			

The research objectives for the work contained in this thesis include: 1) Hardware modifications to change the system from a single fiber/excitation point system to a dual fiber array system capable of either single or double excitation point inspection. The increase in available energy with multiple excitation points will allow larger chip packages to be inspected as well as increased sensitivity to small defects. 2) Further expand the research potential of the system by implementing changes for increased control over the excitation point. 3) Develop and incorporate new safety features and programming bug fixes to increase the safety and reliability of the system. 4) Validate the

improved system by using it to inspect a new type of chip package from CISCO and cross-checking these results with destructive evaluation.

1.5 Thesis Outline

This thesis consists of 7 chapters. A brief mention of the content of each of these chapters is given here.

Chapter 1 gave an introduction to microelectronic chip packaging and its development. Different nondestructive methods were presented along with a brief mention of their limitations. Afterwards the laser ultrasonic inspection method was discussed as well as the research objectives for this work.

Chapter 2 examines the makeup of the system as a whole and then describes each of the constituent parts in more detail. It concludes with a discussion of the limitations to be overcome.

Chapter 3 describes the major system improvements made as part of this project and also presents in depth the process of fiber alignment and input coupler focusing. This is of extreme importance as improper alignment and/or focusing can lead to damage of the fiber optic cables.

In Chapter 4 a basic list is provided of additional improvements that were made to the system.

Chapter 5 constitutes the bulk of this work and is where all the experimental results are presented. First the generation of a standard curve of laser power vs. optical attenuator value is chronicled, as this greatly increased the ease of selecting a particular laser power. Next, the inspection pattern for the new CISCO chip package is described and then experiments determining the damage threshold are discussed. Tests showing the repeatability of the new system are presented followed by a set of experiments demonstrating the advantages of having dual excitation points. The remainder of the chapter is mainly spent on the analysis of the results of both LUI and destructive testing of two CISCO chips. These chips are connected to PCB substrates labeled board #3 and board #29.

Chapter 6 offers concluding remarks and a recap of important contributions.

Chapter 7 introduces recommendations for future research work.

CHAPTER 2
EXAMINATION OF ORIGINAL SYSTEM

In this chapter the system that was operational at the beginning of this research project, as well as some of its limitations, will be discussed. First there will be an overview of the system as a whole and then each of the components/subsystems will be discussed in more detail. The chapter will conclude with the discussion of the limitations of the system.

2.1 Hardware

Figure 2.1 shows a diagram of the original laser ultrasonic inspection system. The system consists of (1) a neodymium-doped yttrium aluminum garnet (Nd:YAG) laser for generating the excitation beam, (2) laser interferometer for measuring the out of plane displacement caused by the vibrations, (3) vibrometer controller for decoding the interferometer signal, (4) sample stage for precision positioning of the DUI under the vibrometer probe, (5) vacuum table for easy, secure mounting of the DUI, (6) laser positioning stage atop the sample stage for fast, repeatable positioning of the excitation laser, (7) fiber optic delivery system to transmit the laser beam from the laser itself to the DUI, (8) vision system for detecting device fiducials for package alignment, and (9) a computer for controlling the system and processing the data.

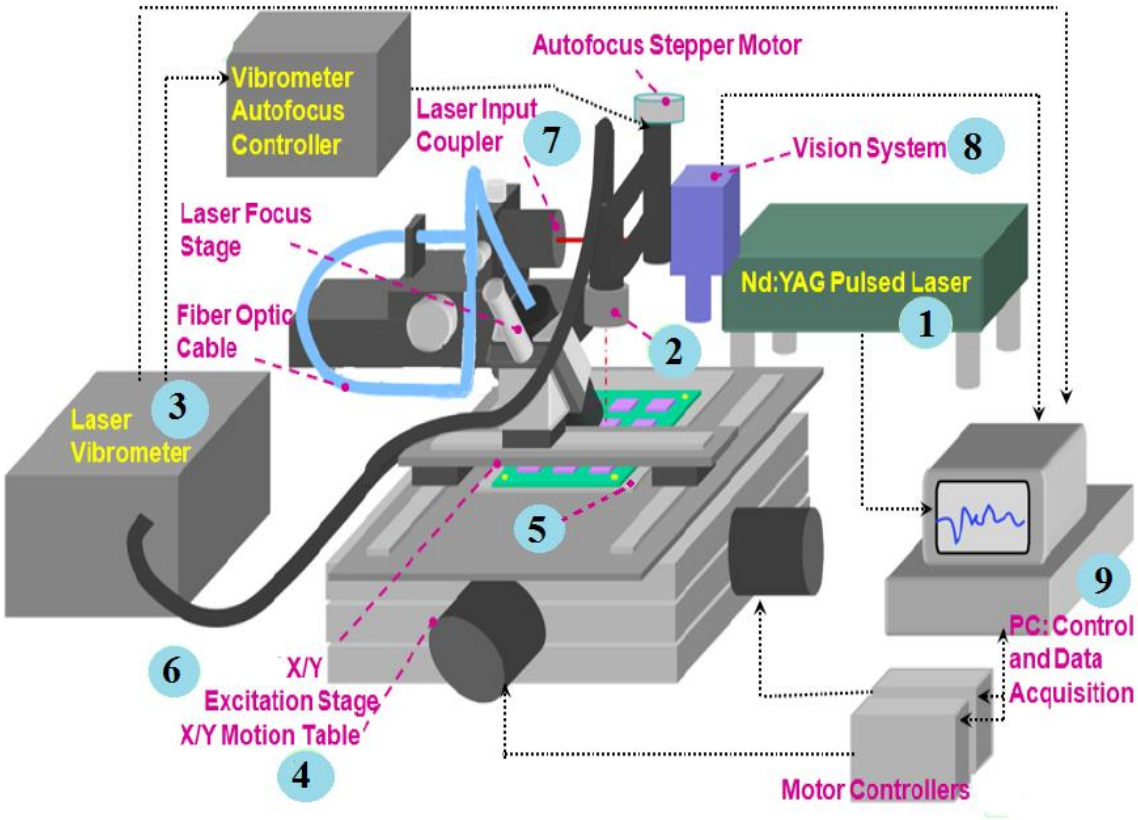

Figure 2.1: Diagram of the exciting LUI system

2.1.1 Excitation Laser

The laser used to generate the ultrasound is a New Wave Research Polaris II as shown in Figure 2.2. The Polaris II is a Q-Switched Nd:YAG laser capable of between 1Hz and 20Hz pulse rate at 1064nm with approximately 4 to 5 nS pulse length. The maximum energy per pulse is 50mJ, though this is well beyond the damage threshold for most chip packages and therefore is carefully controlled by means of an optical attenuator. Figure 2.3 shows the laser power meter system used to calibrate the laser power for the particular chip under inspection. The output beam has a $1/e^2$ diameter of 3mm and 98% pulse to pulse energy stability over 10,000 pulses after a 30 minute warm

up period [31]. The $1/e^2$ diameter of a Gaussian laser beam is defined to be 2 times the radius from the beam axis at which the intensity has dropped to 13.5% of the maximum intensity.

Figure 2.2: New Wave Research Polaris II Nd:YAG Laser System (Source: New Wave Research)

Figure 2.3: Laser power meter

2.1.2 Laser Vibrometer

The system uses a laser Doppler interferometer to measure the out of plane vibrations of the chip package in the ultrasonic region induced by the excitation laser. The Doppler interferometer is made up of a Polytec® OFV-511 fiber optic heterodyne interferometer, shown in Figure 2.4, and a Polytec® OFV-2570 high frequency vibrometer controller, shown in Figure 2.5. As shown in Figure 2.6, the interferometer sensor head is positioned perpendicular to the surface of the DUI, where it delivers the interferometer's laser beam directly to the DUI's surface. The laser spot size can be focused down to 3um so as to achieve a high spatial resolution. The vibrometer controller has an integrated 10MHz bandwidth velocity decoder and 24MHz displacement decoder. As the out of plane vibration of the DUI is the variable of interest, the velocity decoder was not used. The maximum displacement measurable by the system is 75nm with a measurement resolution of 0.3nm. In addition to measuring the displacement, the vibrometer controller also measures the intensity of the reflected laser interferometer measurement. The greater the amount of laser light reflected back to the interferometer,

the greater the signal-to-noise ratio (SNR). In this system, the information concerning the intensity of reflected light is provided as feedback to the autofocus subsystem, which allows the automated adjustment of the DUI to sensor head distance to maximize the collected light.

Figure 2.4: Doppler Interferometer used in the LUI system

Figure 2.5: Vibrometer controller used in the LUI system

Figure 2.6: Interferometer sensor head

2.1.3 Autofocus System and Local Search Pattern

The surface finish of the DUI can greatly affect the amount of laser light from the interferometer that is reflected back into the sensor head. A smooth finish results in a more specular reflected beam and a rough surface results in a more diffuse beam. The amount of light collected by the interferometer greatly affects the SNR, with a decrease in the amount of light corresponding to a low SNR and vice versa. Therefore, it is

important to adjust the standoff distance between the DUI and the sensor head until the captured light is maximized. This is achieved by mounting the sensor head onto a motorized linear stage which can change the standoff distance. Before data is taken at a particular point, the system reads the intensity of the light collected by the sensor head and the result compared to a set threshold value. If the measured intensity is below the threshold the autofocus system will initialize a scan in which the height of the sensor head is adjusted until an intensity value above the threshold is found. In the event that this fails, the system will initialize a "Local Search" in which the inspection point is moved out in a rectangular spiral in increments of 1 micron at a time. An example search pattern is shown in Figure 2.7. At each step in the process an autofocus routine is run to search for an intensity value above the threshold. This continues for a predetermined number of steps or until a suitable intensity value is found. In the event that an intensity value above the threshold is not located, the data will be taken at the point where the highest value was measured.

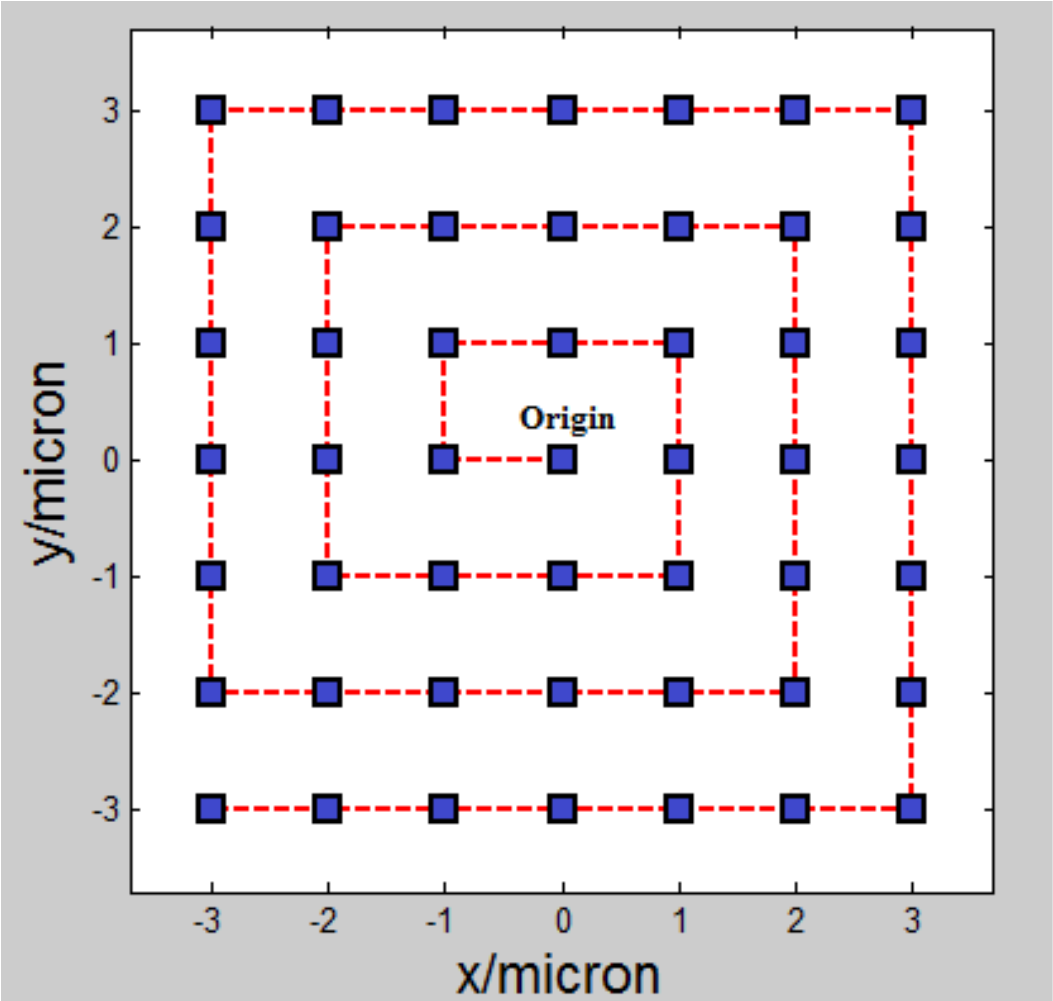

Figure 2.7: Local search pattern for autofocus system

2.1.4 Vision System

The vision system makes use of a camera, shown in Figure 2.8 and software to detect fiducial marks on the PCBs that carry the DUI and is used for calculating the coordinates for the excitation laser and inspection points. Fiducial marks are marks on the PCB, usually a small circle, square, or cross of copper, or gold/silver plated copper, which serve as reference points by which a system can determine the exact location and orientation of the PCB. An example of a round fiducial mark is shown in Figure 2.9.

Fiducials are useful for pick-and-place machines where they allow for precise placement of microelectronic components. In this research the fiducial marks are used by the vision system to detect how the board is placed on the vacuum stage, and this information used to calculate the motor commands used to move the laser and interferometer to the correct locations.

Figure 2.8: Camera used to detect the fiducial marks

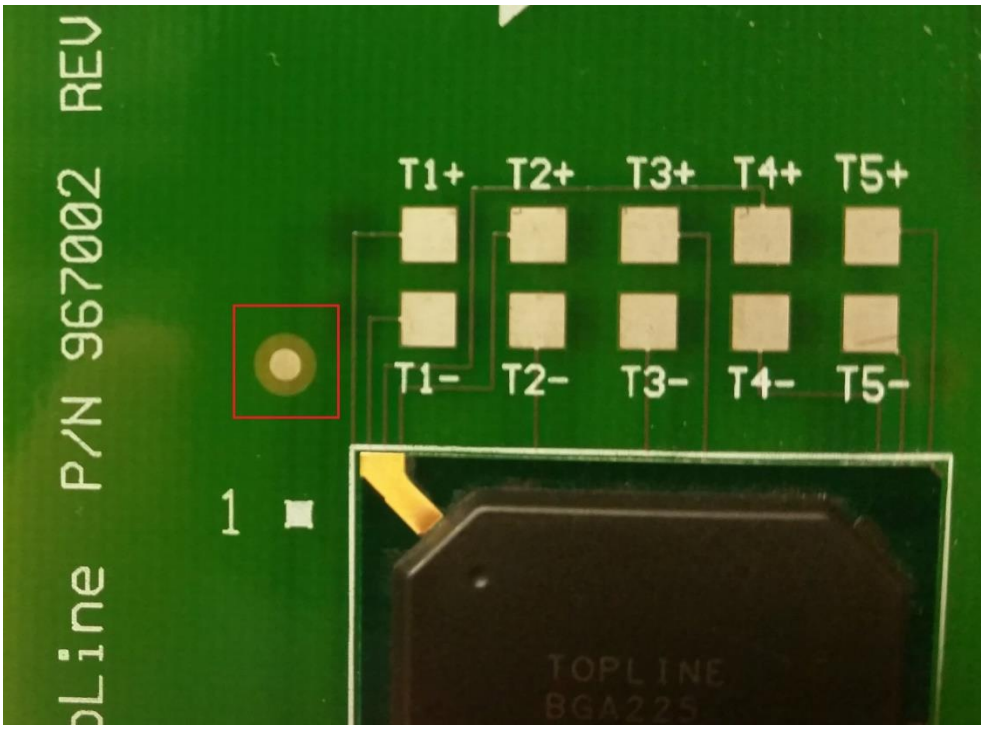

Figure 2.9: Photograph of a PCB with the fiducial mark indicated

2.1.5 Bandpass Filter

A Krohn-Hite Corporation model 3945 high-pass/low-pass Butterworth/Bessel programmable filter, shown in Figure 2.10, was used in low pass and amplifying mode to filter out unwanted high frequency noise as well as to amplify the signal from the vibrometer controller. The programmable filter features 3 independent input channels, a frequency range from 3Hz to 25.6MHz, and noise of <250 uV referred to the input. In this research, only the Butterworth low-pass channel was used with a cutoff frequency of 2MHz and an input gain of 10db and output gain of 6db.

Figure 2.10: Filter and amplifier (Source: Krohn-Hite Corporation)

2.1.6 Fiber delivery System

The original fiber delivery system was composed of an input coupler, 600um core fiber optic cable, and a non-adjustable collimator and a focusing lens, all by U.S. Laser as shown in Figure 2.11. This system allows the excitation laser to remain stationary while allowing the excitation point on the DUI's surface to be positioned as needed. The fiber optic cable features a PVC armored jacket that provides protection against mechanical shock and some resistance to over bending. LD-80 end connectors were used for secure, repeatable fiber attachment. The fused silica core was chosen for its high laser energy damage threshold and low loss characteristics, which allows the nanosecond scale laser pulses to be efficiently transmitted to the DUI.

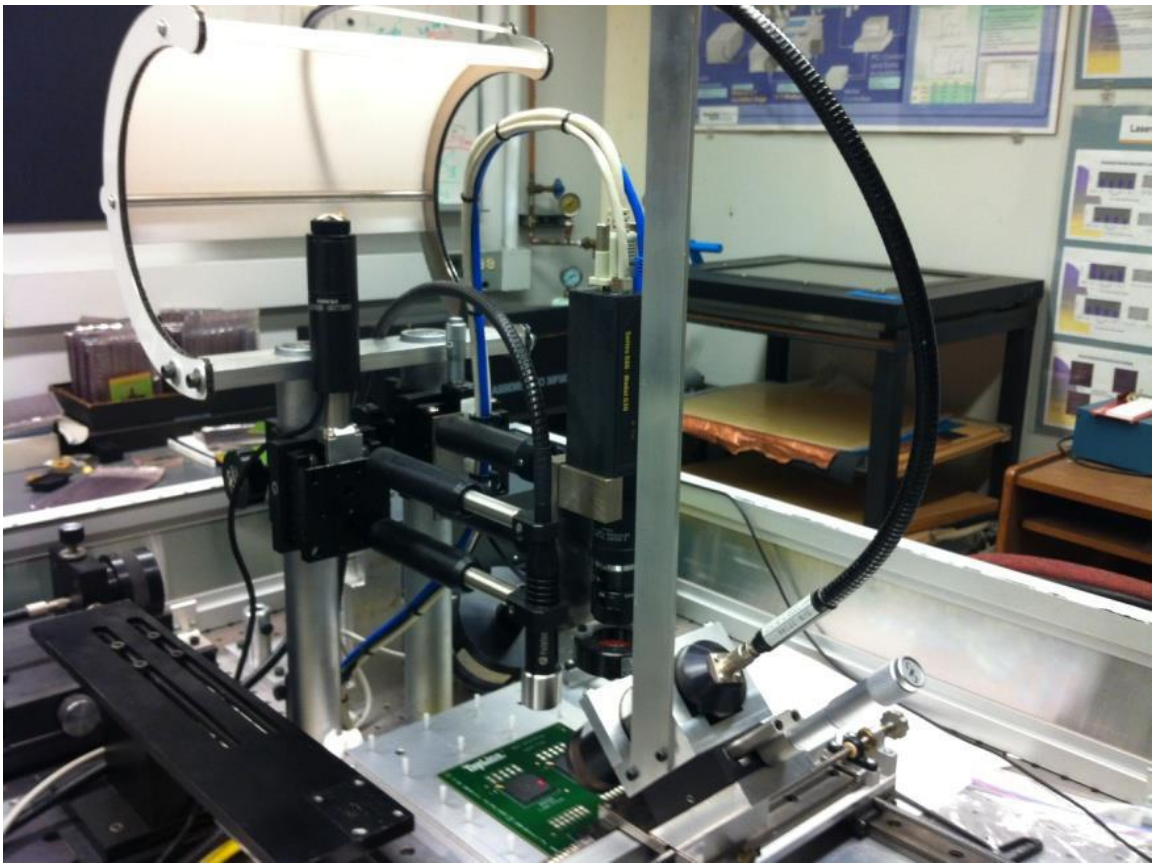
Figure 2.11: Original fiber delivery system

2.1.7 Sample Positioning Stage

The sample positioning stage is a stepper motor controlled X-Y stage made by Nutec Inc. and is used for precise, automated positioning of the DUI. As per the manufacturer's specifications the accuracy is 7.5um per 100mm of travel with bidirectional repeatability of ±1.0 um, and an orthogonality error of less than 7.5 arc-seconds. This is accomplished by the use of preloaded crossed-roller bearings, which eliminate play, and precision-grade lead screws. The stage has a large 200mm x 200mm range of motion atop which is mounted the vacuum table and Arcus laser positioning stage (see below). An image of the stage is shown in Figure 2.12.

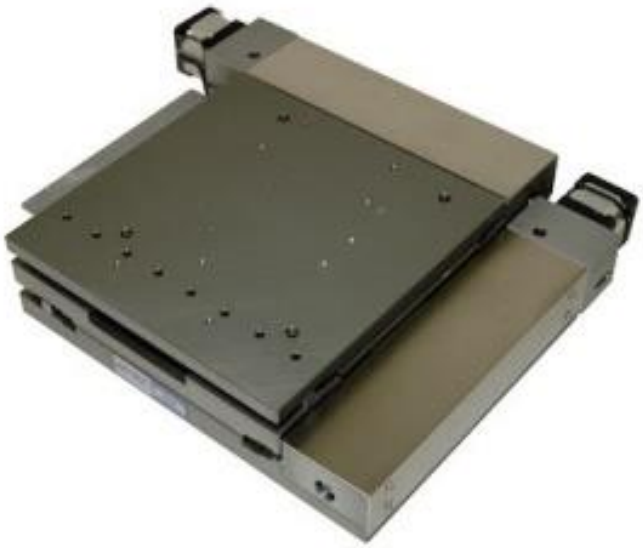

Figure 2.12: X-Y Positioning Table (Source: Motioncontrol.com)

3.1.8 Vacuum Table

The vacuum table, shown in Figure 2.13, is mounted atop the sample positioning stage and is used to securely fix the DUI during the inspection process. The table consists of an anodized aluminum vacuum plate which the sample sits on as well as an alignment fence for the sample to be butted up against for repeatable placement of the sample. The vacuum plate has two independent systems of channels machined into the back of it; these are connected to a total of 48 inlet ports. When a vacuum is drawn from one of the main vacuum ports, air is sucked through the system of channels and ports, which in turn will vacuum down onto the plate the sample positioned on it. As seen in Figure 2.13, one system of channels and ports extends only over a small portion of the plate and is used

for securing small samples while the other system extends over the entire plate and is used to secure larger samples.

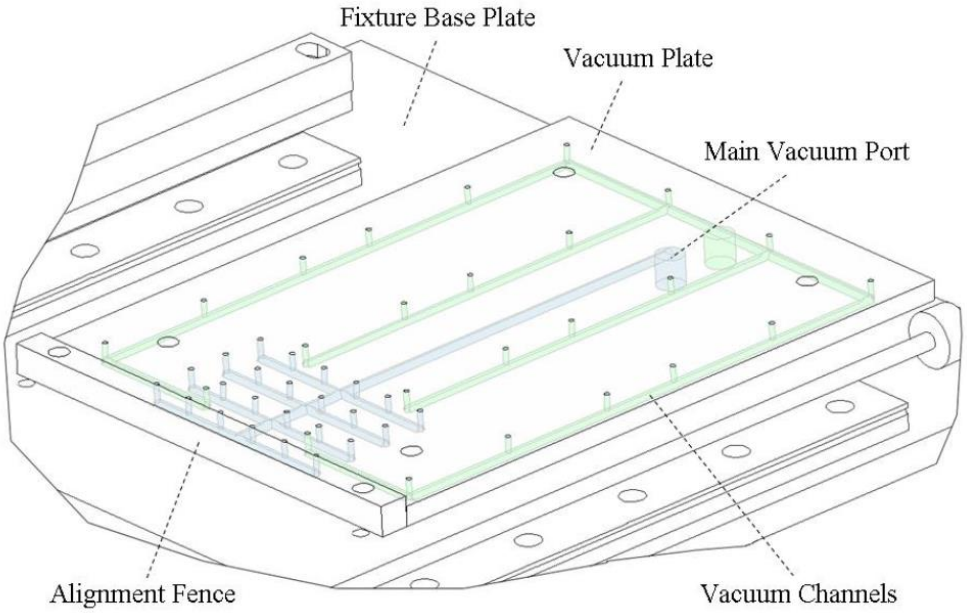

Figure 2.13: Vacuum table for securing the samples during inspections. The channels that connect all the inlet holes for securing large samples is shown in green while the channels that connect the inlets to secure small samples is shown in blue. (Source: [7])

2.1.7 Arcus laser positioning system

The laser positioning XY-stage is a custom built motorized stage for accurate, repeatable automated positioning of the laser excitation spot. The stage incorporates PCB 25thread/in lead screws and 200step/rev stepper motors to drive the movement as well as an Arcus PMX-2ED-SA stepper motor controller capable of micro-stepping and ±5% step accuracy. To increase accuracy and repeatability, feedback is provided by one ACU-RITE MicoScale™ linear encoder per axis. The encoder feedback allows 1um excitation

spot positioning resolution to be achieved with repeatability within one resolution count. Figure 2.14 shows a picture of the Arcus system with the end effectors mount on top.

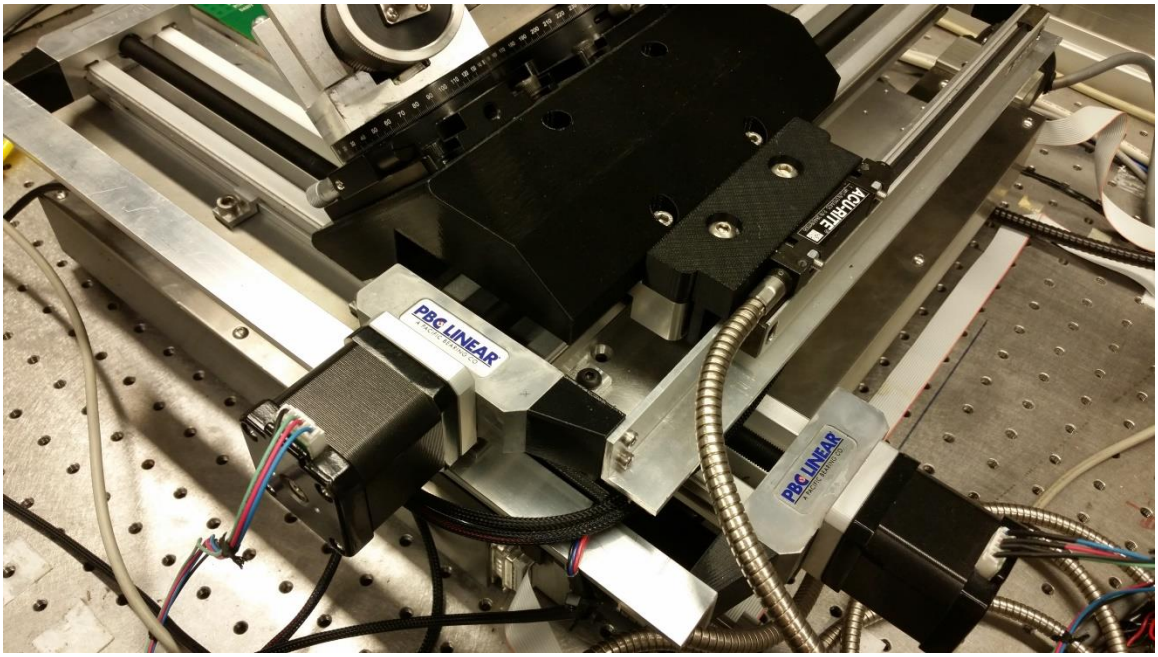

Figure 2.14: Laser excitation point positioning stage

2.2 Limitations of the original system

In this section some of the limitations of the previous system are discussed. Some will be discussed in detail while some will simply be mentioned.

2.2.1 Non-adjustable end effector

The end effector (EE), shown in Figure 2.15, is the unit composed of a collimating lens, to collimate the diverging beam exciting the fiber optic cable, and a focusing lens, for directing the collimated beam down to a small spot on the DUI. The original EE used a non-adjustable collimator, meaning the distance between the end of the fiber and the collimating lens could not be adjusted. This meant that the distance from the EE to the focal plane could not be varied and therefore, for a stationary EE, the size of the incident point was fixed. This meant that the size of the incident spot on a DUI would change depending on how thick DUI was. This could cause issues, such as the incident spot being focused to too small a point and exceeding the damage threshold of the DUI, or the incident spot could be too large, and therefore the energy density too low to effectively generate ultrasounds. In the original system a way to address this impediment was implemented by mounting the end EE on a linear stage which could either move closer or farther away from the DUI. As shown in Figure 2.16, the light leaving the focusing lens forms a conical shape as it converges down to a point located on the focal plane for the lens. Once the light passes through the focal point it starts to diverge in a conical shape opening up in the direction of travel of the light. Therefore, when the EE is moved closer or farther from the DUI the path of the light will be intersected at different points, changing the size of the incident spot. With this set up the area of the incident spot could be varied from $0.6mm^2$ to approximately $8mm^2$ [32]. It was desired to expand the range of possible incident spot sizes so investigations could be conducted on the effect incident spot size has on the inspection results. In addition, this would allow adjustments of the incident energy density so as not to damage the DUI.

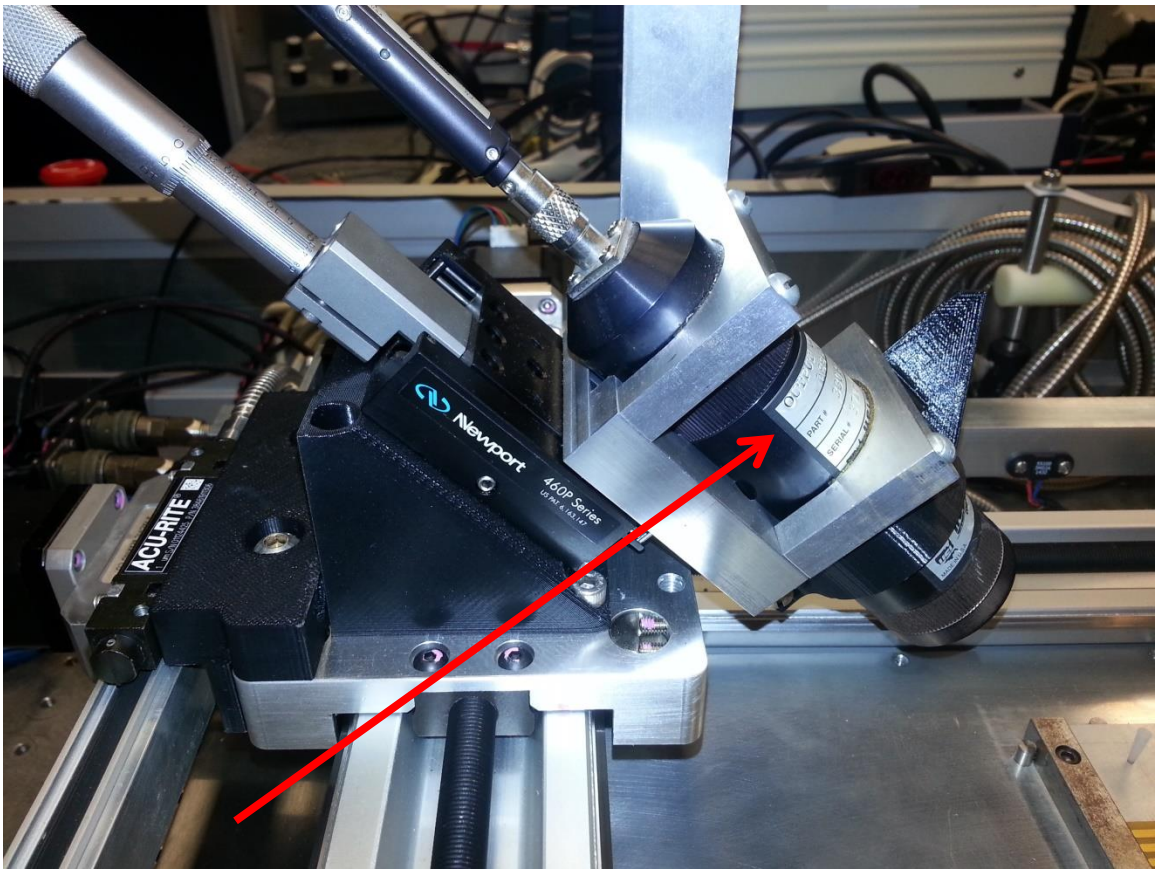

Figure 2.15: Photograph of fixed type end effector (Source: U.S. Laser)

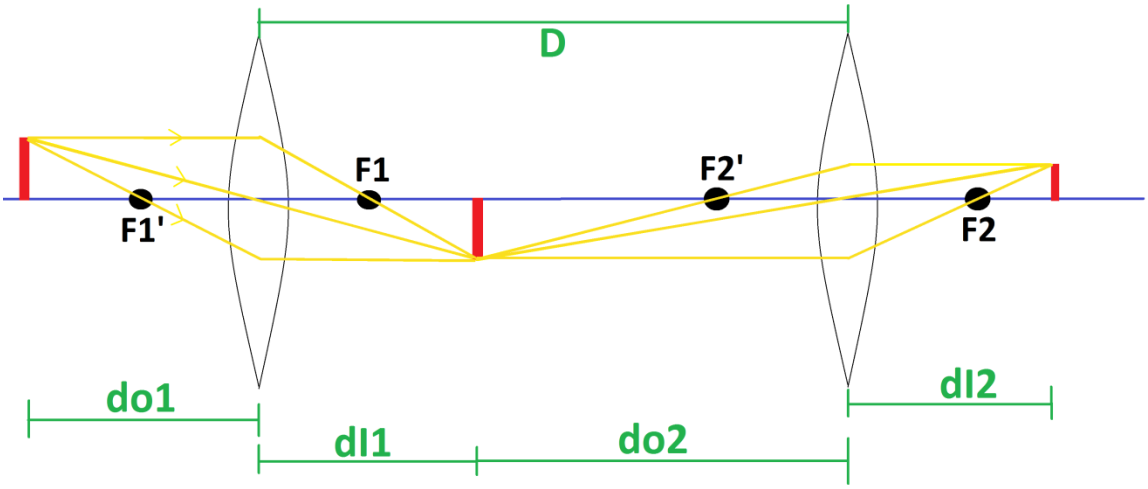

Figure 2.16: Ray diagram showing the bending of light rays as they pass through two lenses

2.2.2 Single Excitation Point

The damage threshold of a particular device is concerned with the maximum laser energy density the surface of the device can withstand before material begins to be ablated. For a particular incident spot size this limits the energy that can be delivered for ultrasonic generation. The strength of ultrasounds that can be produced from the maximum energy for a single incident point might not be strong enough to detect very small defects or inspect large devices. Therefore, a means to deliver multiple incident spots was desired so that the total energy delivered to the device could be increased. In addition, multiple incident points open up more studies that can be done to investigate the possible benefits of using different incident spot configurations.

2.2.3 Single Fiber Optic Cable

The use of a single fiber optic cable has additional considerations beyond allowing only one incident spot to be used. While using just one incident spot limits the energy that can be used for inspecting the chip without damaging it, using just one fiber optic cable limits the amount of energy at the experimenter's disposal due to the intrinsic damage threshold of the fiber. Ignoring factors such as self-focusing, Smith *et al* reports finding the intrinsic damage threshold of a fused silicon fiber to be 4.75 kW/um2 (or 47.5 GW/cm^2) this number though can be much lower depending on many factors, such as the

polishing method used for the ends of the fibers [33]. Because the minimum fiber bend radius depends on the diameter of the fiber core, the energy needed to inspect a large chip package could force the use of a fiber with an impractically large minimum bend radius.

2.2.4 Limited Safety Features

The original system had a limited number of safety features that inadequately protected against collisions between the end effector and the interferometer probe. Precise calibration of the locations of the laser excitation point and the interferometer probe is required for successful comparisons of inspections across multiple different devices. Therefore, it is paramount that the interferometer probe not collide with the end effectors. A laser tripwire safety system was in place in the original system, but only would cut power to the Arcus stage to keep it from driving the end effectors into the interferometer probe. Normal operation of the system during the homing routine did not allow for the tripwire safety feature to be applied to the sample positioning stage. Additionally, the in place E-stop circuit did not cut power to the sample stage either, so that even if an impending collision was observed it was difficult for the operator to stop the system in time. Multiple instances of collisions/near collisions had occurred, leading to damaged components and many wasted hours of system downtime.

CHAPTER 3
SYSTEM IMPROVEMENTS

This chapter will deal with the major improvements made to the system. Much of the hardware used in the original system stayed the same so when something is not specifically mentioned it may be assumed that it was unchanged. Any of the minor changes or those that do not require much description will be listed in the next chapter.

3.1 Laser multiplexer system

The heart of the upgrade to the optical fiber array system is the U.S. Laser multiplexer. As shown in Figure 3.1, this device takes in a single laser beam and by means of a partial mirror splits the beam and directs each of the split beams into a separate input coupler to be launched into one of two fiber optic cables. The multiplexer also incorporates a half-wave plate which is used to adjust the balance between the two beams.

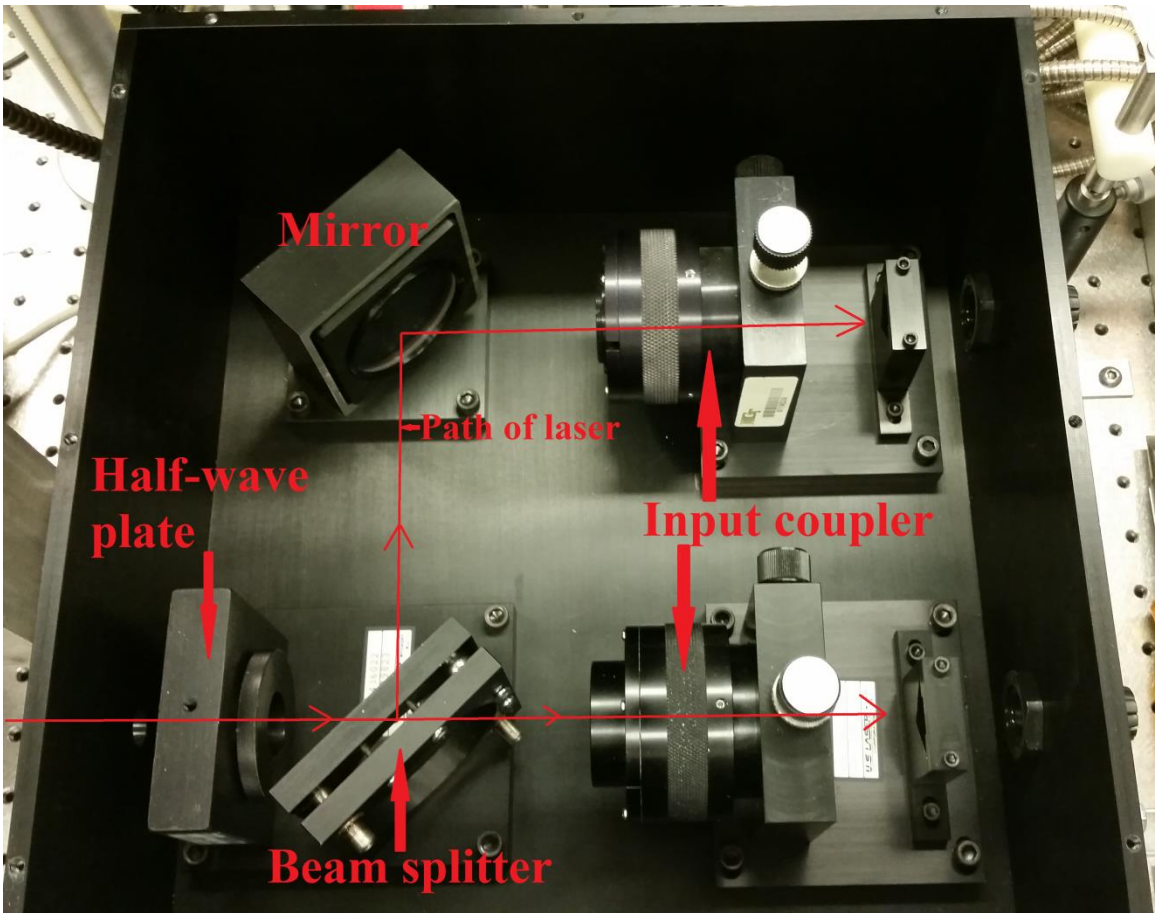

Figure 3.1: Workings of the laser multiplexer with laser path shown

3.1.1 Mounting

For ease of mounting, and so proper alignment of the laser to multiplexer input could be obtained, a set of brackets and adjustment screws was devised. To set the height of the multiplexer, four adjustment screws were threaded into the mounting table, and the height was adjusted by changing how deeply the screws were turned in. Centering the laser through the input aperture to the multiplexer is important to proper coupling into the fibers. To determine correct screw adjustment, calipers were used to find the difference

between the distance measured from the table to the laser aperture and the distance measured from the bottom of the multiplexer to the input aperture. The calipers were then used to set the adjustment screws to this height.

XY translation was prevented by the system of L-brackets, nuts, and bolts as seen in Figure 3.2. These were implemented on all four sides of the multiplexer, and once it had been aligned using the edge of the table as a reference, the nuts and bolts were tightened.

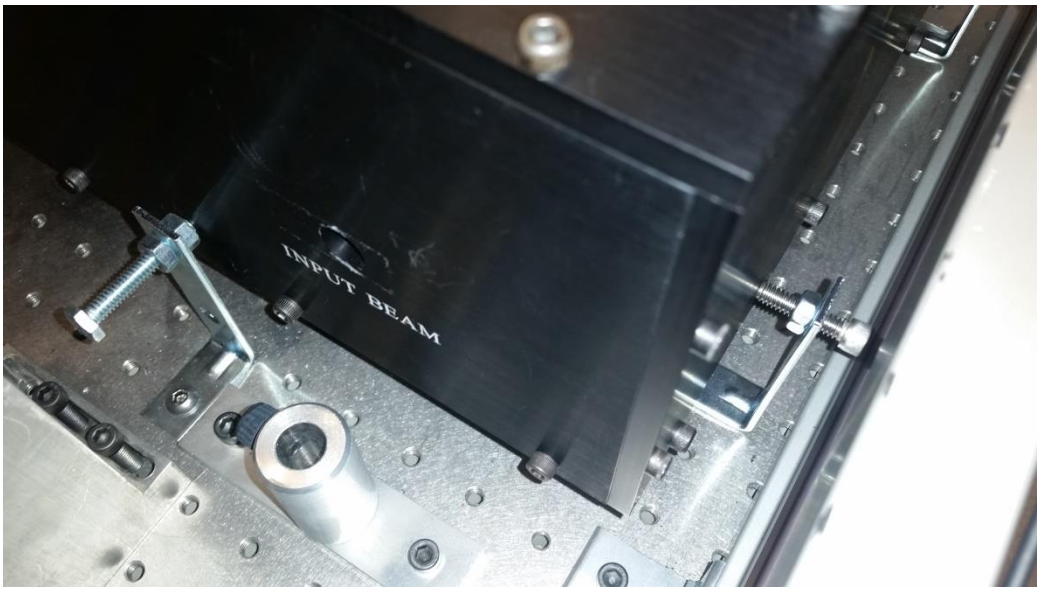

Figure 3.2: Brackets and bolts securing multiplexer

3.2 Rotational end effector stages

To accomplish the goal of allowing for a range of laser incident point spacings, two ThorLabs PR01 rotational stages were installed on which the end effectors would be

mounted. As seen in Figure 3.3, the stage has a micrometer and Vernier scale for precise adjustment. The 5 arcmin gradations allow for adjustments of ±1 arcmin to be made. This correlates to repeatability in the spacing of about 0.5mm.

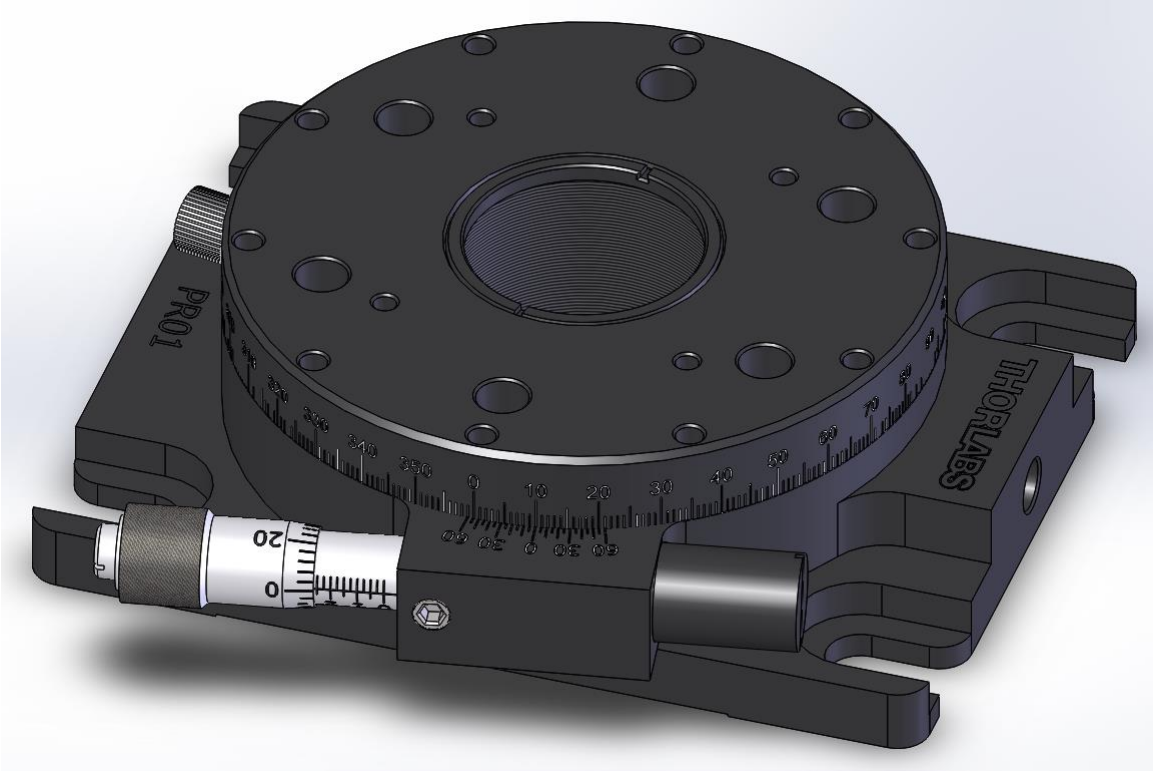

Figure 3.3: Rotational stage for adjusting the laser incident spot spacing

To set the spacing between the incident laser spots a MATLAB program was written. This program allows the user to input the desired spot spacing, along with the height of the package to be inspected, as measured from the vacuum table, and outputs the angle setting for each rotational stage in degree, minute format.

3.3 Adjustable end effectors for focusing

The original end effectors used did not allow for the focal length to be changed and therefore new adjustable end effectors from U.S. Laser were installed. The adjustment is achieved by rotating the threaded tube the fiber optic cable attaches to while the fiber is removed. In doing this the distance between the end of the fiber and the collimating lens is changed. As seen in Figure 3.4, the result is that the beam leaving the collimating lens is converging, collimated, or diverging. Whichever of these behaviors occurs, determines the focal distance of the beam. As a result, the incident spot size will change. The adjustable end effectors were attached atop the rotational stages via two machined aluminum clamps, and this assembly was affixed to a custom designed and 3D printed mount that rides on the Arcus positioning XY stage. This entire assembly can be seen in Figure 3.5.

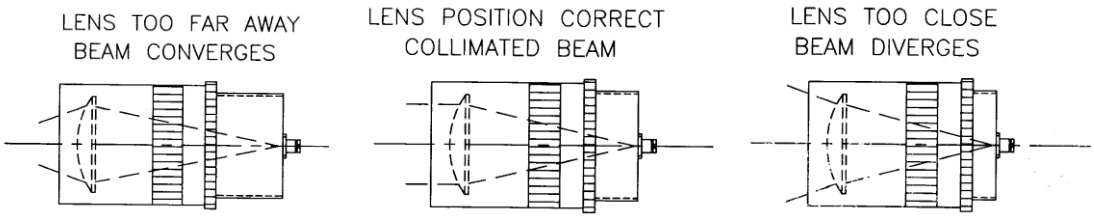

Figure 3.4:Diagram showing laser beam behavior vs. position of focusing screw

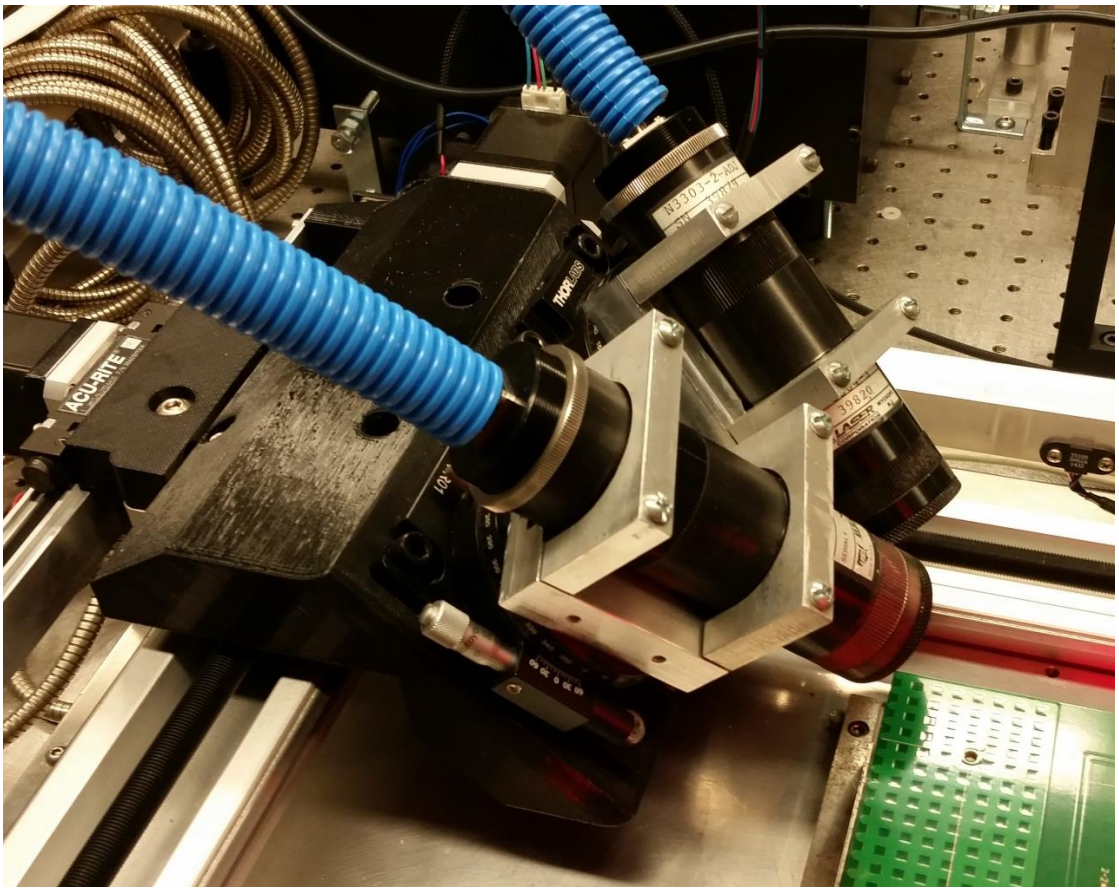

Figure 3.5: Rotational stage and adjustable end effector assembly.

The minimum size the beam can be focused to is given by equation 4

$$S_{min} = \frac{f_2}{f_1} d_{core} \quad (4)$$

where f_2 is the focal length of the objective lens, f_1 is the focal length of the collimating lens, and d_{core} the fiber optic cable core diameter.

Taking the values for the system of f_2 = 75mm, f_1 = 60mm, and d_{core} = 1mm gives a minimum focused spot diameter of 1.25mm. Knowing the laser is incident at a 45degree angle allows the minimum incident spot size to be calculated at ~1.73mm^2 using the equation for the area for an ellipse.

In order to focus the laser onto any height package it was necessary to undertake some optical calculations. Using the thin lens equation 5 for both the collimating and focusing lenses, the relationship between the distance from the collimating lens to the focal distance of the objective lens was derived and is shown in equation 6.

$$\frac{1}{d_o} + \frac{1}{d_i} = \frac{1}{f} \tag{5}$$

where d_o is the distance to the object being imaged, d_i is the distance to the image produced, and f is the focal length of the lens.

$$d_{o1} = \frac{f_1\left(\frac{f_2 d_{i2}}{d_{i2}-f_2} - D\right)}{f_1 - D + \left(\frac{f_2 d_{i2}}{d_{i2}-f_2}\right)} \tag{6}$$

where d_{o1} is the distance from the end of the fiber optic cable to the collimating lens, f_1 and f_2 are the focal lengths of the collimating lens and objective lens respectively, d_{i2} is

the distance from the objective lens to the focal plane, and D is the distance between the collimating and objective lenses. Therefore, using the known constants for the lenses, all one must do is to substitute the distance to the desired focal plane and the output will be the needed distance between the fiber end and the collimating lens. Using a CAD model of the system along with basic trigonometry, the mathematical relationship between the desired focal plane and the height of the DUI was found. Using this and the number of threads per inch on the focus adjustment, a program was written in MATLAB that allows the user to input the height of the package from the vacuum table, and the program will output the number of turns to move the focus adjustment to focus the laser spot on the surface of the package. To make the process as efficient as possible this code and the code for setting the incident spot spacing were integrated into a single program.

3.4 Hall Effect collision prevention

Due to the need for precise calibration to allow for successful comparisons of inspections across multiple different devices, it is paramount that the interferometer probe not collide with the end effectors. This would disrupt the alignment of the probe and possibly damage the internal lens or other components of the system. A laser tripwire safety system was in place in the original system, but that one protected against the Arcus stage causing the collision. At the start of this project there was no safety system to protect against the sample positioning stage moving the end effectors into contact with the interferometer probe. To prevent this from occurring, a proximity sensor setup was devised using Hall Effect sensors and neodymium magnets. As seen in Figure 3.6, the

Hall Effect sensors are attached in a ring on the interferometer probe while the magnets are mounted over the end effectors. The Hall Effect sensors output an analog signal to a custom designed microcontroller circuit. The closer the magnets are to the sensors the greater their output voltage. If that voltage surpasses a predetermined threshold the microcontroller will shut off a relay controlling power to the system. This will stop the system in a fraction of a second preventing the collision.

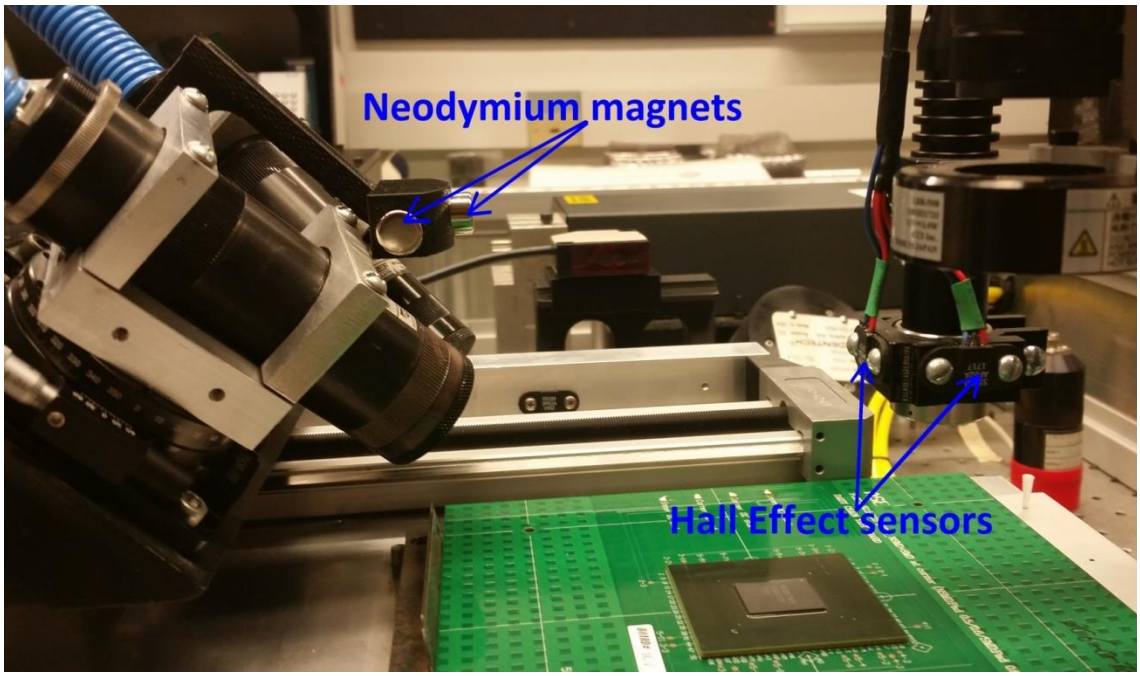

Figure 3.6: Hall Effect safety system

Figure 3.7 shows the circuit layout of the microcontroller PCB and Figure 3.8 shows the assembled board and relay. The ATMEGA328P microcontroller was chosen for its low cost, availability, and excellent documentation.

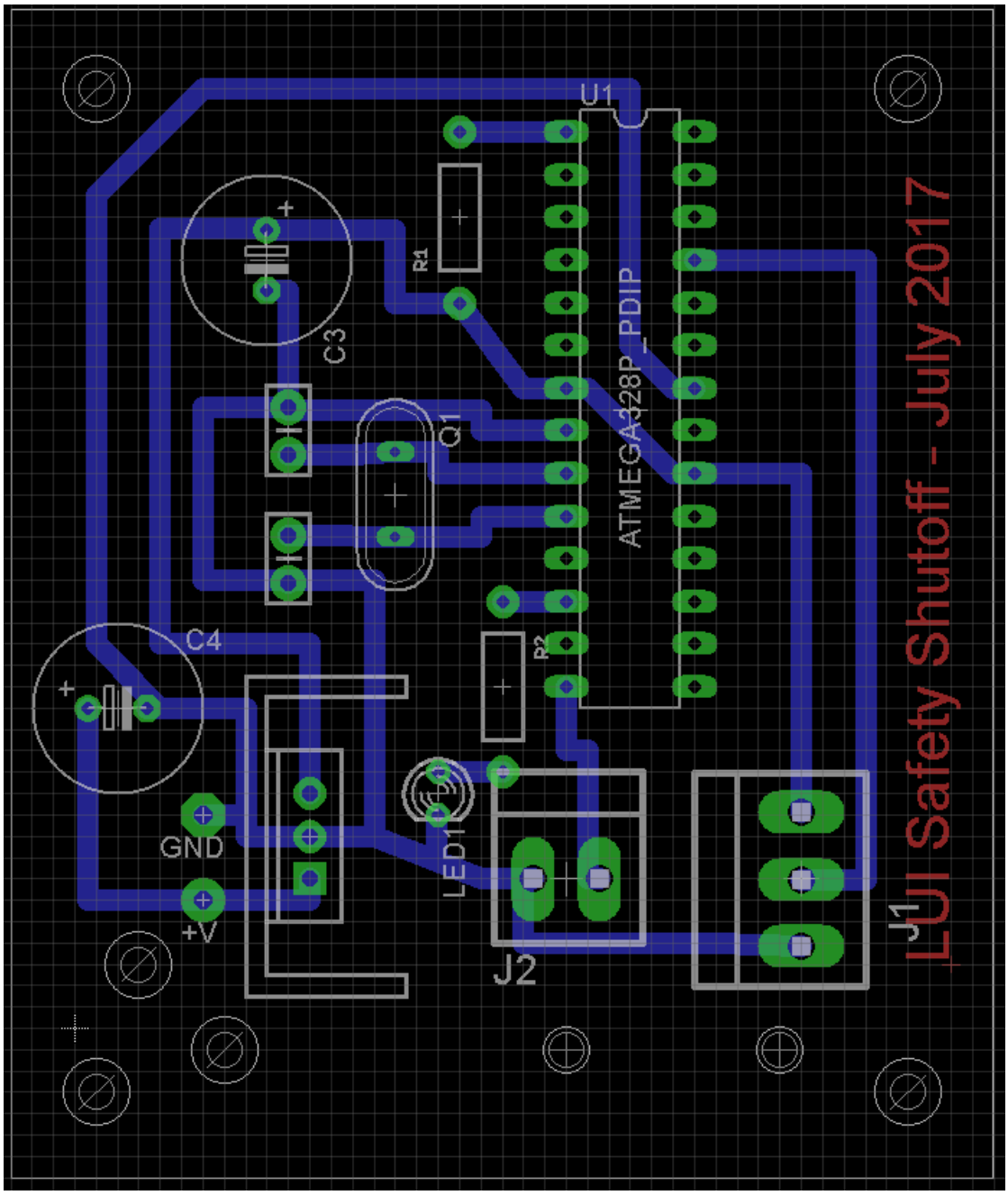

Figure 3.7: Eagle CAD layout of Hall Effect safety system circuit

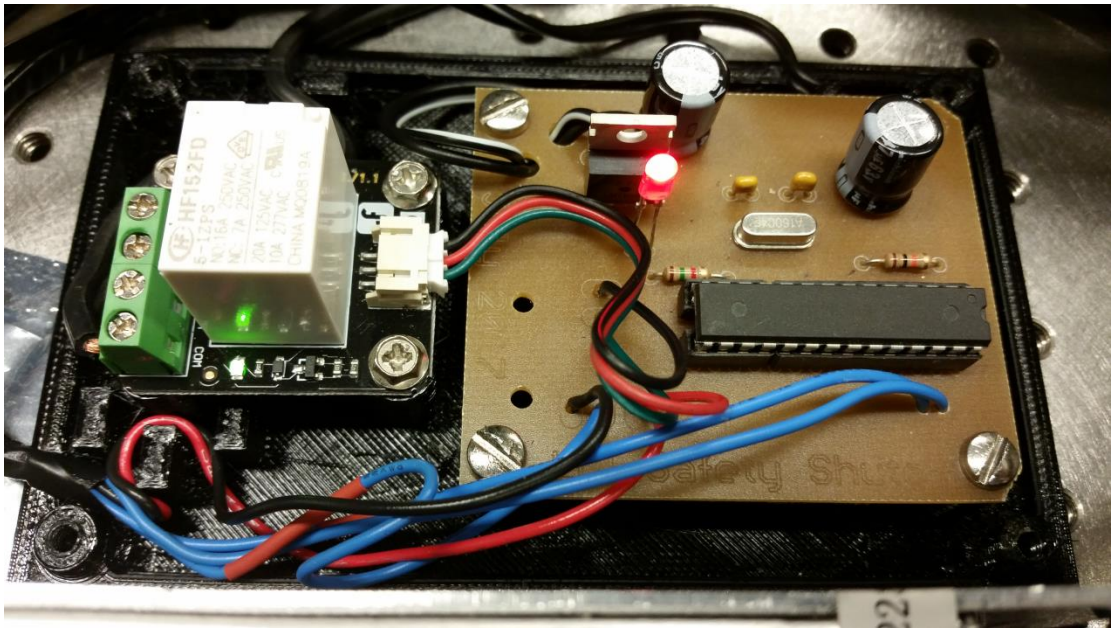

Figure 3.8: Completed Hall Effect PCB

3.5 Alignment and Beam Power Balancing

To avoid damaging the fiber optic cable and/or wasting power, the laser beam must be properly coupled into the fiber. The fiber input coupler, seen in Fiber 3.8, is the device that is made to accomplish this. This is done by means of a focusing lens mounted in a movable housing that allows the lens to translate along the fiber's axis thereby focusing the beam onto the fiber's surface. Additionally, two screws can adjust the XY alignment between the incoming beam and the end of the fiber. In order to prevent damage to the fiber and/or power loss, the beam must not only be centered on the fiber's face but also focused correctly. Fiber 3.9 shows different possibilities for the fiber alignment/focus.

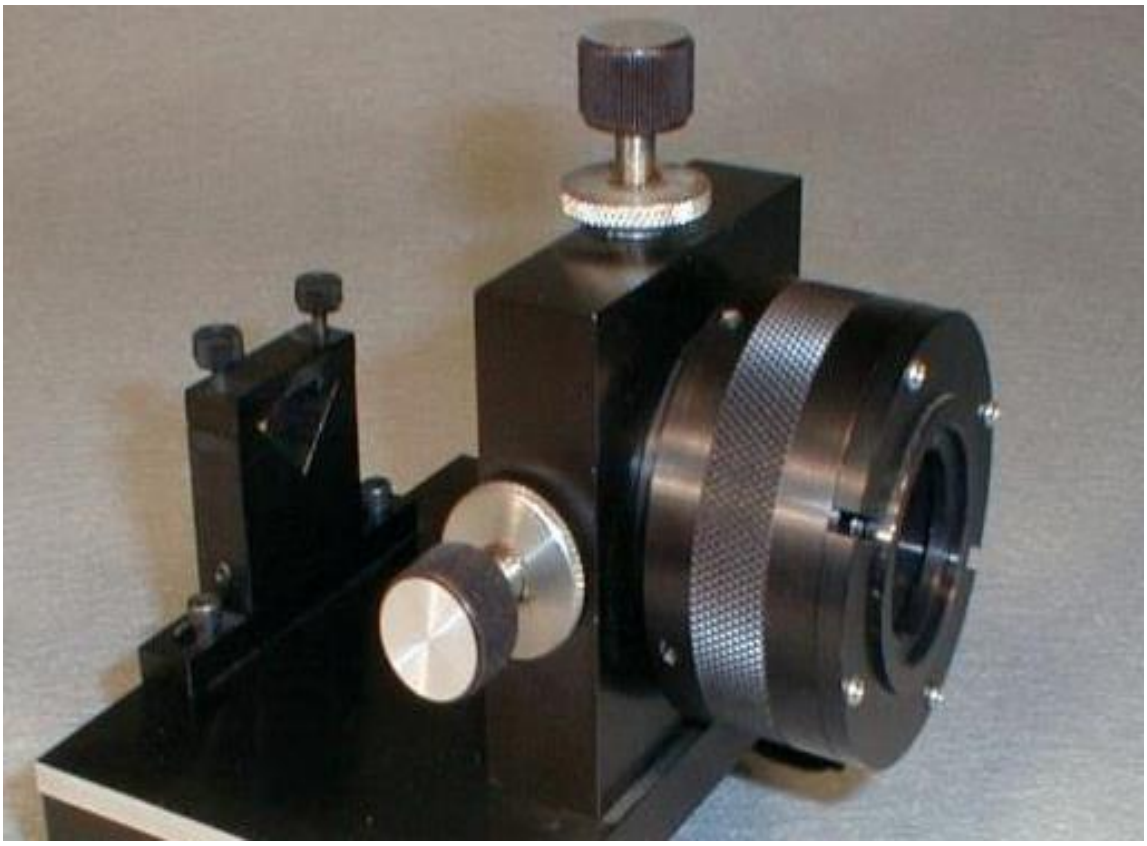

Figure 3.9: Fiber input coupler mounted with fiber holder shown on left (Source U.S. Laser)

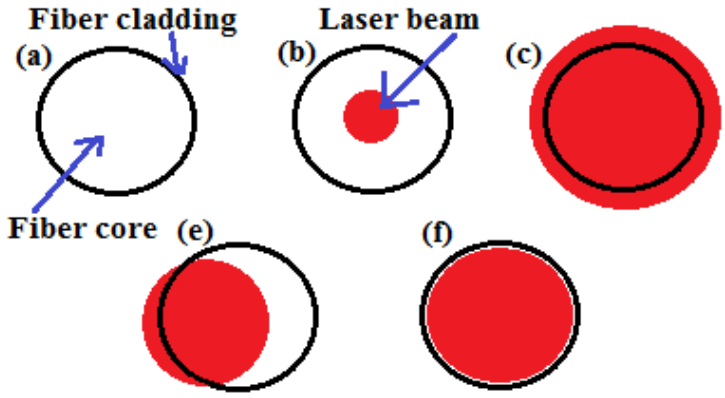

Figure 3.10: Different ways to couple the laser into the fiber. (a) Representation of end of fiber. (b) Beam is aligned but focused too small. (c) Beam is aligned but focused too large. (e) Beam is misaligned. (f) Proper alignment and focus.

To align the laser exiting the input coupler to the fiber optic cables' face the input coupler's focusing adjustment was set at the mid position, and the laser turned on to a low power (<25mW). A rough alignment is achieved by placing a piece of lens cleaning paper coated in pencil graphite over the output aperture of the input coupler. This makeshift viewing paper flashes green when irradiated, and these flashes can be seen through the paper. The XY adjust knobs were adjusted to center the green spot as close as possible to the center of the output aperture. A copper alignment aperture, seen in Figure 3.10, was screwed onto the input coupler's output, and the power meter used to measure the laser power escaping through the hole. One axis at a time, the adjustment knobs were varied until the measured laser power was maximized. This assures that once the fiber was installed the laser would be centered on the fiber's face.

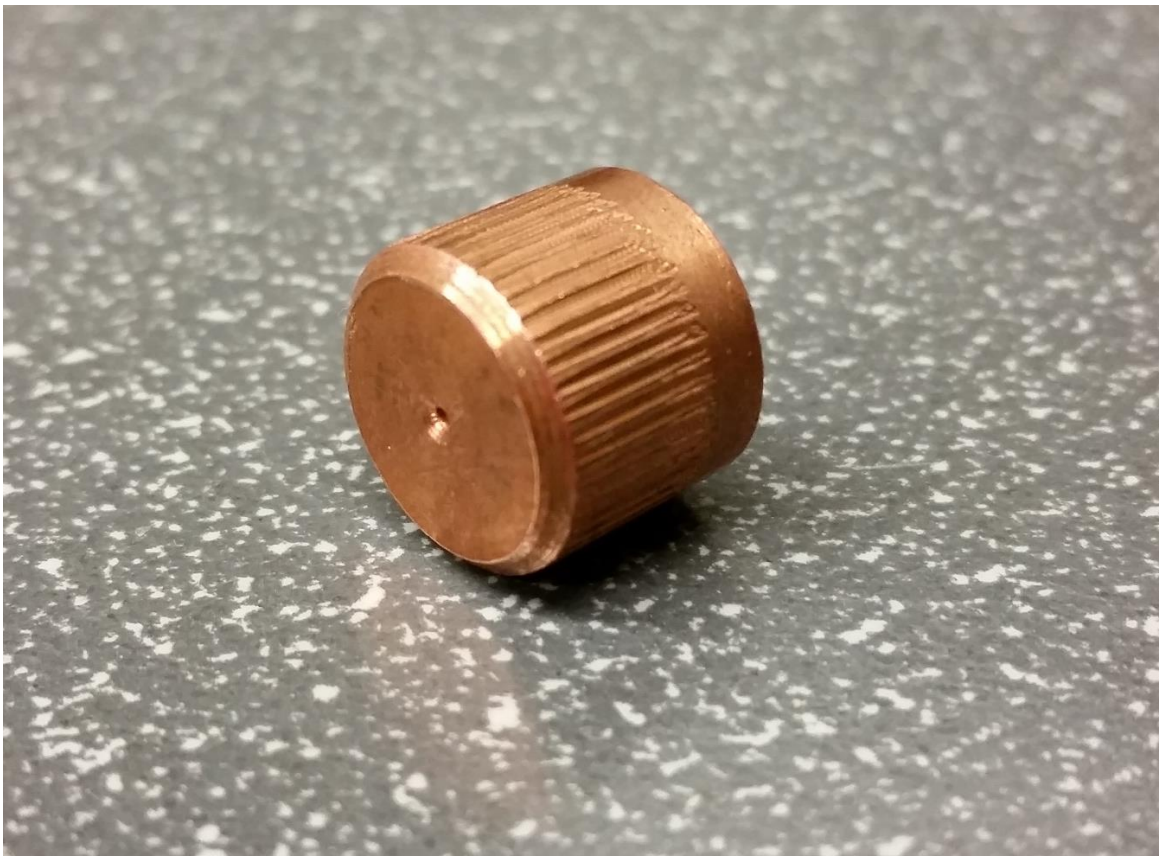

Figure 3.11: Copper alignment aperture

To set the focus, the laser was powered off, the copper aperture removed, the input coupler's focusing adjustment set all the way clockwise, and the fiber optic cable attached. The laser was set to a low power, and the output of the fiber directed into the power meter. The focusing adjustment was then slowly turned counter-clockwise until the measured power began to decrease. The focusing adjustment was then reversed for ¼ turn. At this point the power transmission was ~91% of the input power.

Confirming proper alignment and focusing was accomplished by directing the output of the fiber onto a laser viewing card. A well-defined spot on the card means alignment and focusing was successful. Figure 3.11 shows the possible images seen on the viewing card.

Figure 3.12: Possible outputs of the fiber (Source: U.S. Laser)

Figure 3.12 shows a photograph of the completed system.

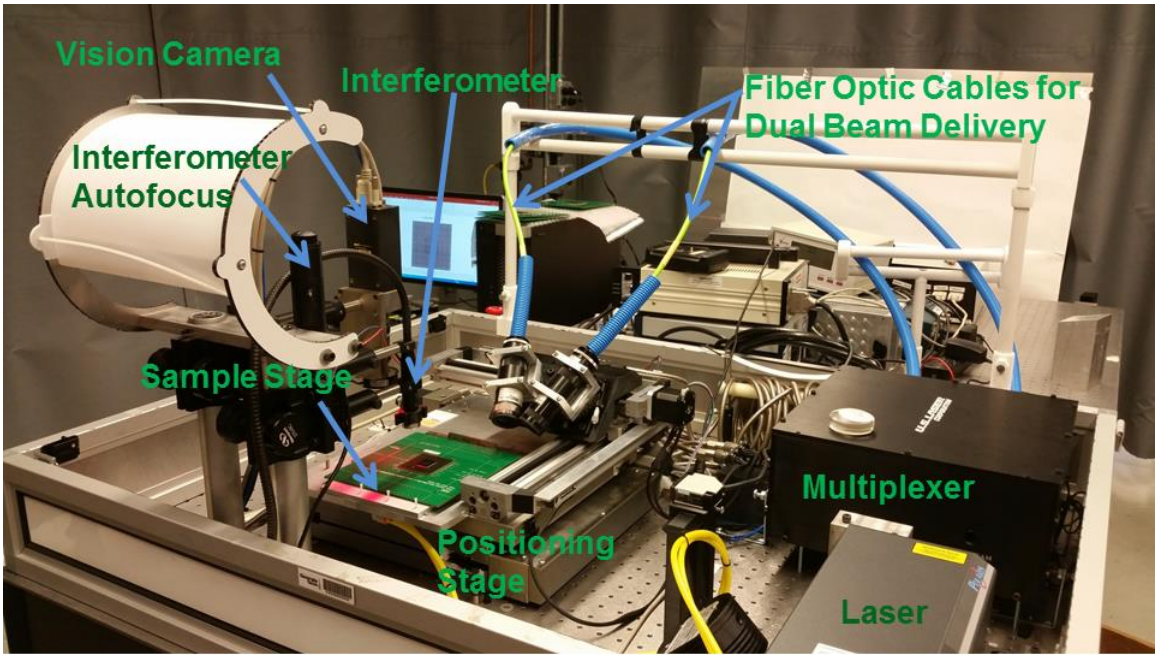

Figure 3.13: Photograph of the upgraded LUI system

CHAPTER 4
SUMMARY OF ADDITIONAL IMPROVEMENTS AND CONTRIBUTIONS

In this chapter many of the minor improvements which benefited the system but in themselves do not merit much discussion will be chronicled with either a brief description or a simple listing.

4.1 Hardware

4.1.1 Arcus clamps

As seen in Figure 4.1, a set of aluminum clamps is used to secure the rails that the laser positioning system uses. The original system used a single clamp on each side of the rail even though there is space for two clamps on each side. In addition, the channel machined in the clamp was too deep and as a result even when the clamps are securely tightened the rails could be knocked out of alignment with minimal effort. To correct this issue four new clamps were machined that had a more shallow channel as well as a higher pivot point, to allow for a greater degree of force to be applied to the rail. A CAD rendering of the clamp can be seen in Figure 4.2.

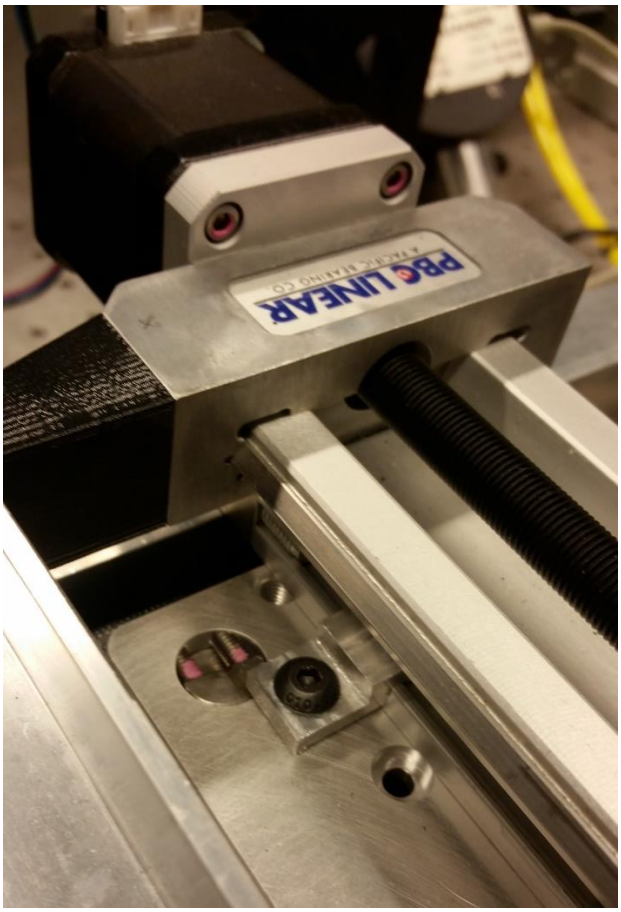

Figure 4.1: Clamp used to secure the laser positioning stage

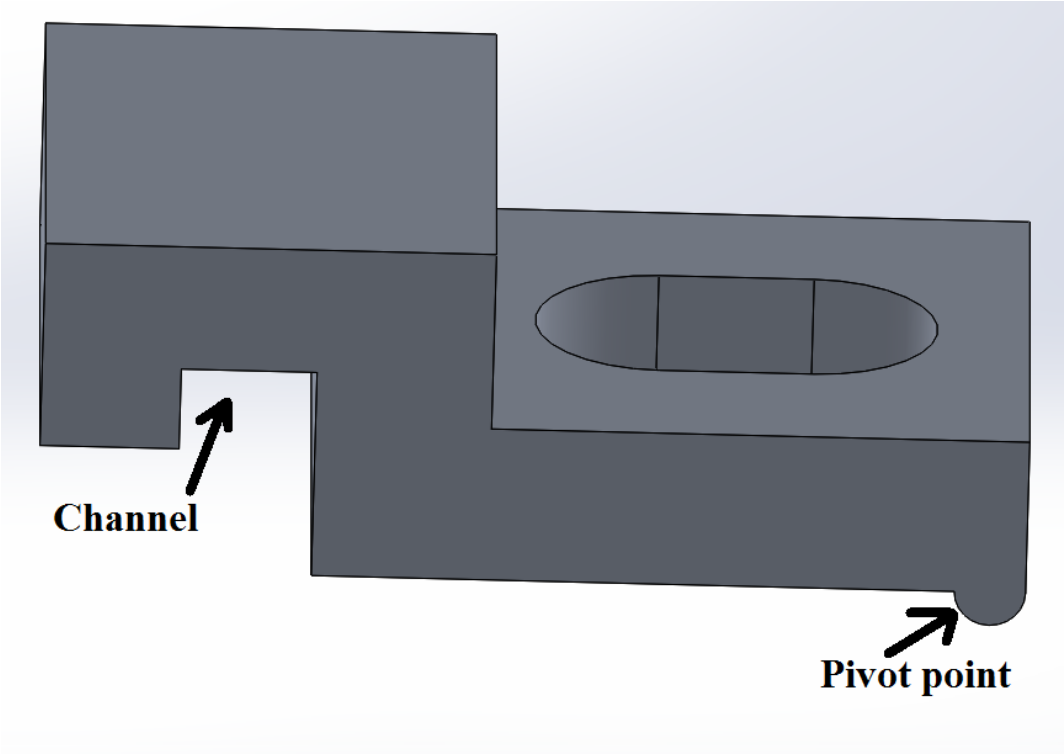

Figure 4.2: New clamp for Arcus laser positioning system

4.1.2 Repaired Autofocus stage

The autofocus linear stage was behaving erratically and repairs were needed. When performing autofocus routines, the stage would sporadically try to move past the maximum downward position. It was found that the end stop was failing. This was repaired and the stage then functioned as normal.

4.1.3 System reconfiguration

The original configuration of the system required the new fiber optic cables to extend past the edge of the system's table. This was deemed inadequate as the cables could easily be knocked into and damaged. Therefore, the entire system was disassembled and then reassembled in a new orientation that routed the cables over the table itself.

4.2 Software

4.2.1 LUI code

Many small modifications were made to the LUI code to improve the performance and reliability of the system. Some of the modifications include: (1) Modified the MATLAB directories to stop MATLAB from sporadically crashing on running the code. (2) Added a fix to the autofocus routine to correct an error where the data was not being read properly at times due to an input buffer issue. (3) Implemented code to fix a problem where the laser would not fire when using the single capture feature. (4) Improved the laser positioning stage's homing routine for better collision avoidance between the fiber optic cable end effectors and the interferometer.

4.2.2 Arcus code

At the beginning of this research it was noted that reasonably often the Arcus laser positioning stage would stall when attempting a move. This was investigated and it was found that the movement accelerations were set too high for the system impedance. This was rectified in the code by proper adjustment of the movement parameters.

4.2.3 Autofocus code

While investigating the previously mentioned issue with MATLAB not reading the data from the autofocus system it was found that under certain circumstances the autofocus microcontroller would send the wrong position data to MATLAB. This was corrected by changing the code and reprogramming the autofocus controller.

CHAPTER 5
SYSTEM VERIFICATION AND EXPERIMENTS

5.1 Creating Standard Curve of Laser Output Power vs Attenuator Value

In this section a standard of laser output power vs attenuator value was constructed. This needed to be done as the system operator would previously change the laser power by directly entering an attenuator value instead of the desired laser power. If the operator wanted to know the laser energy at a particular attenuator value, they would have to guess at the attenuator value needed, fire the laser and let it warm up for 30 minutes and then use the power meter to measure the laser power. This could be a time intensive process, especially if a particular laser power is needed and/or many different laser powers needed to be used. In order to quickly and more accurately set the laser output power during the inspection process a set of tests were conducted to measure the output power of the laser at discrete attenuator values, and the data was recorded. The laser was allowed to warm up before data collection began. Data were taken with the attenuator starting at 10 and incrementing in steps of 10 up to a max of 150. At each value the laser was allowed to fire for 20 seconds before the reading on the power meter was recoded. Once an attenuator value of 150 was reached, the test was begun again. This was repeated a total of three times. From this, the averages of the data sets were calculated and a best fit line found. The results are shown in Figure 5.1. The equation of the best fit line is $y = 0.0124x^2 + 0.6759$ with an R^2 value of better than 0.99. Knowing

this equation, one can substitute in their desired laser power and then use an equation solver to find what attenuator value they need for that laser power.

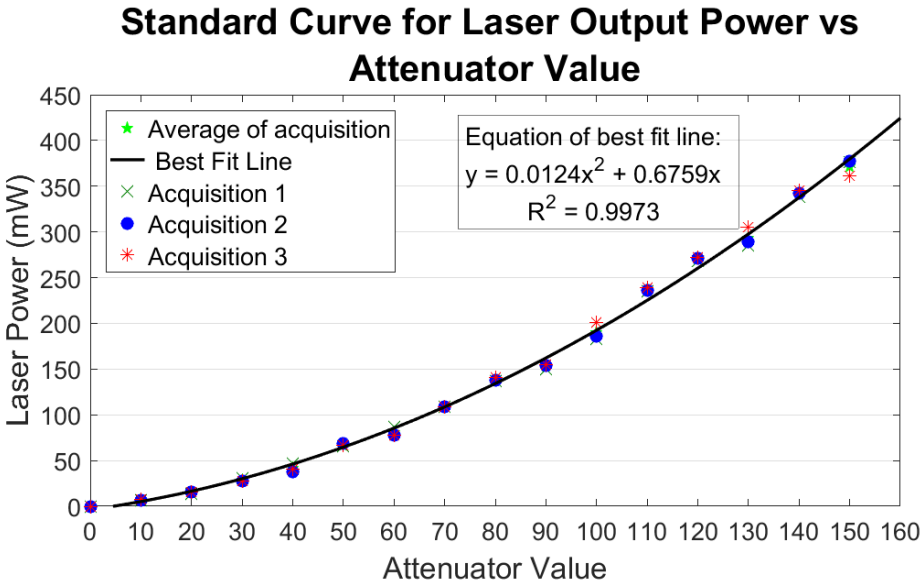

Figure 5.1: Graph showing the data collected for the laser power vs attenuator value tests. The best fit line is also plotted and the equation of the line shown.

5.2 Inspection Pattern for CISCO Chip

All the tests that make up this work were conducted on a flip chip ball grid array (FCBGA) package supplied by CISCO. The chip measures 52.5mm x 52.5mm square with a 20mm x 18.5mm FC at its center. The top of the FC is approximately 5mm from the board. An example of the chip is shown in Figure 5.2. This chip is similar in construction to the one shown in Figure 5.3, in that the FC is joined to a BGA substrate layer, which allows the connections to the board to be made with larger, more robust

solder balls with a greater pitch. The space in between the FC and the top of substrate is underfilled for added strength.

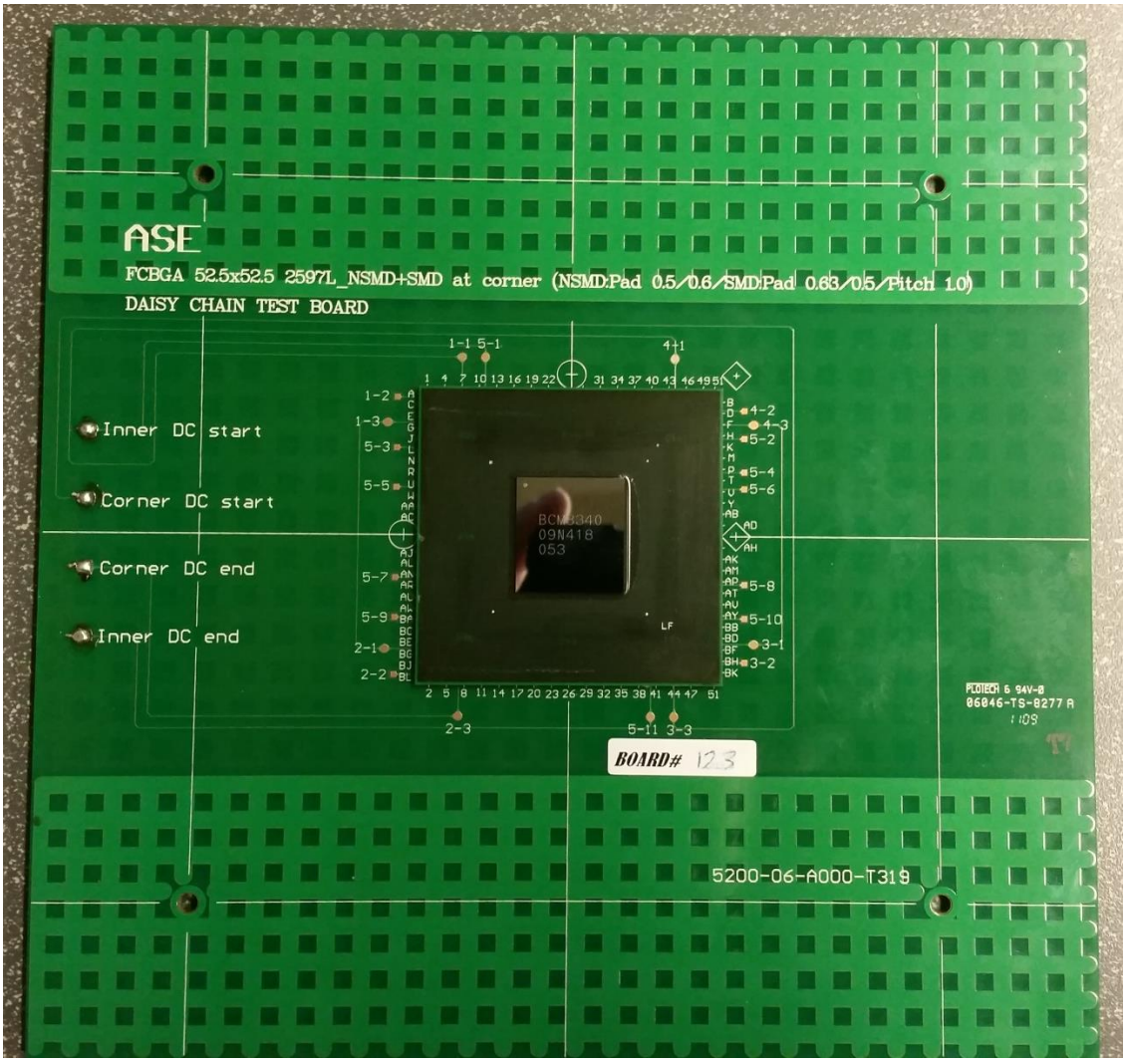

Figure 5.2: Photograph of the CISCO board with the FCBGA at the center.

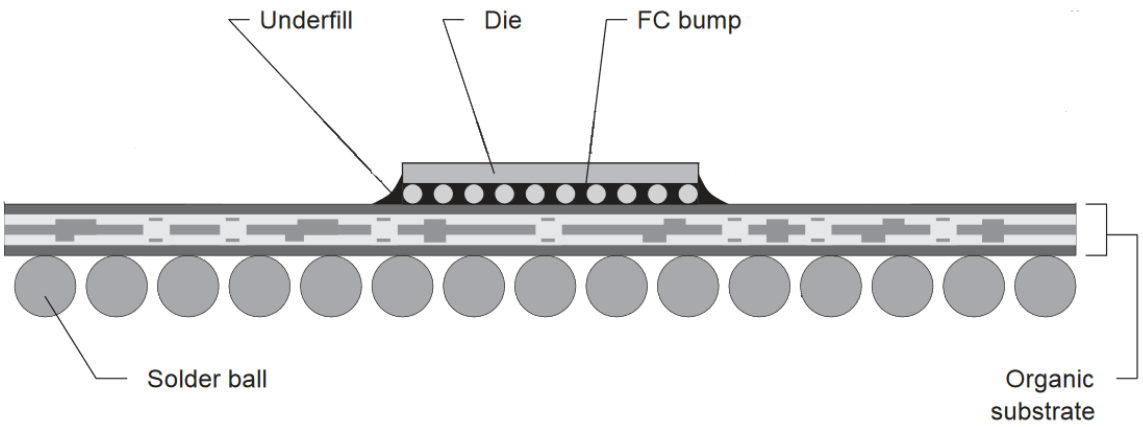

Figure 5.3: A cutaway showing the FC inside a BGA package. Note the bumps used on the underside of the die. Source: Texas Instruments.

Two different inspection patterns were chosen to be tested. One involved dividing the area of the chip into 9 subsections, as shown in Figure 5.4, and treating each subsection as its own chip, and the other using a single excitation point and taking data over the entire surface of the BGA. For the subsection inspection pattern, the laser excitation point was positioned over the section's center while the interferometer laser was moved to the inspection locations. The need to subdivide the chip was twofold; because of the large nature of the chip, and the underfill beneath the FC, it was not known if a signal of sufficient strength and quality would be able to be generated to conduct a reliable inspection on the solder balls underneath the exposed portion of the BGA. Therefore, by taking data from the subsections individually, a way of crosschecking the results from the whole board test was created. Also, subdividing the chip allowed tests to be run on a smaller portion of the FCBGA, which allowed for greater speed and efficiency when tests did not require data from the entire chip. As hinted at above, the other inspection patterns involved centering the laser excitation point/points in the middle of the FC and then taking data from all of the substrate.

Because the substrate was the main area of interest, the FC was kept as its own section. How the chip was divided is shown in Figure 5.5.

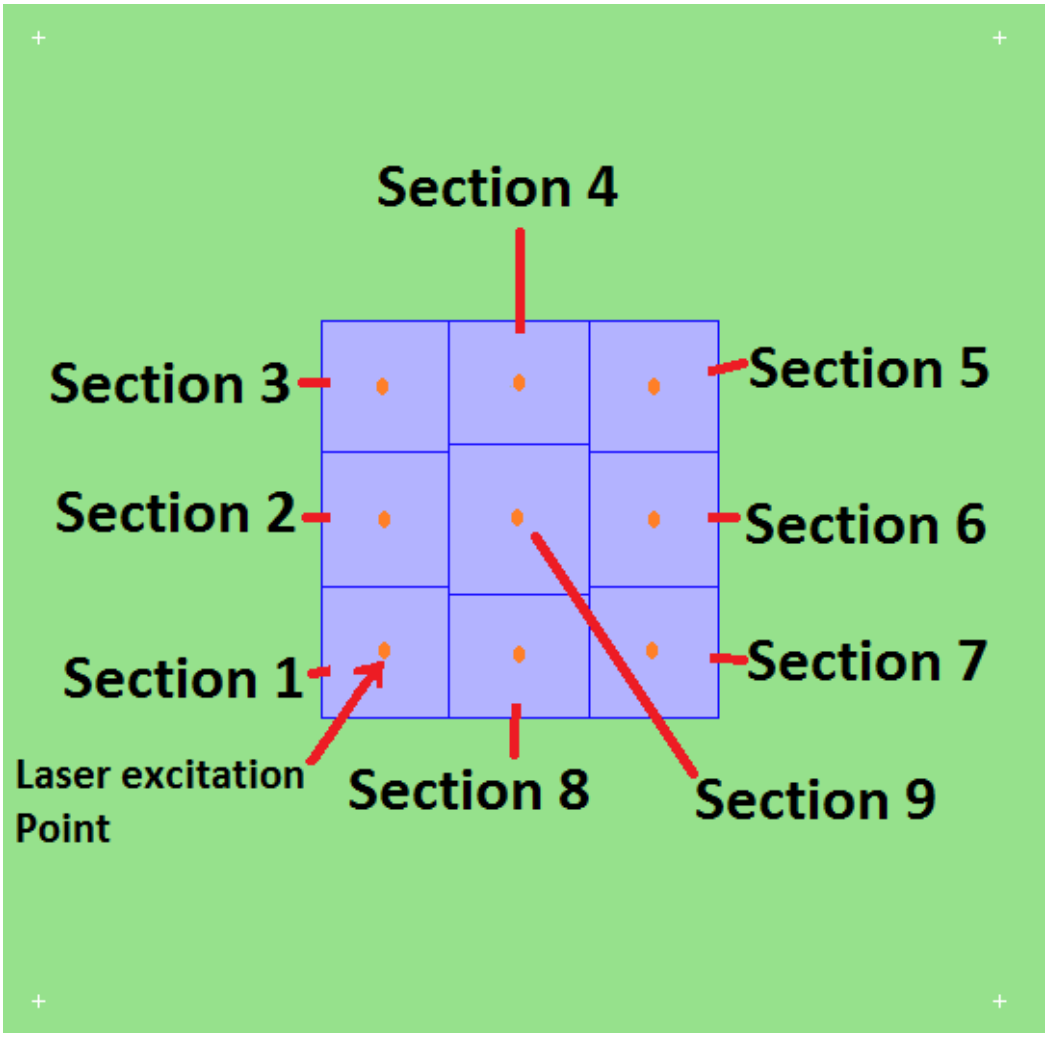

Figure 5.4: Diagram showing how the CISCO chip was subdivided. Note that each subsection has its own excitation point

Figure 5.5: Diagram showing how the CISCO chip was divided into only two inspection areas – FC and substrate. The excitation remains constant at the center for all of the inspection

The inspection locations were determined based on the layout of the solder balls. Figure 5.6 shows a sitched together x-ray of the CISCO chip with solder balls clearly shown as an array of dark circles. As shown, there are no solder balls in any of the corners. If one looks closely the slightly darker gray area in the center shows the location of the FC. The board itself was too large to be x-rayed adequately all at once because when done there was a large degree of pincusion distortion due to the curvature of field

of the x-ray machine that the software could not correct. To solve this the board was x-rayed in quadrants, and the images were imported into a photo editing software and manually stiched together.

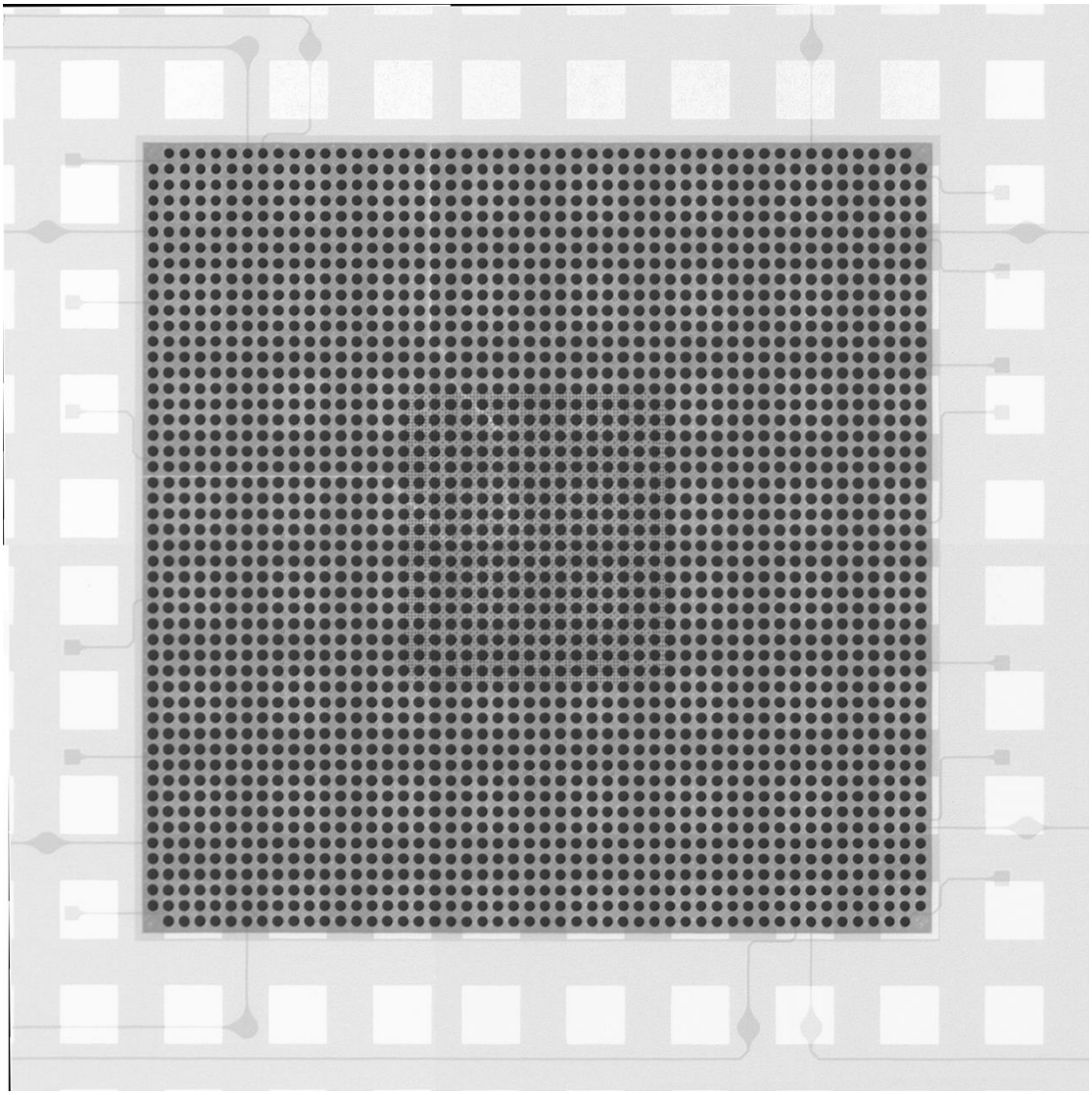

Figure 5.6: A 2D X-ray image of the CISCO chip. The array of solder balls shows up clearly as the black circles (no solder balls in the corners)

Normally, the inspection locations are generated from the board's gerber files (files that contain all the dimentional data for the board that manufacturers use when making the boards). However, the gerber files were not available, so therefore in order to obtain the exact dimentions necessary, the x-ray was imported into a CAD software and scaled to the known dimensions of the chip of 52.5mm x 52.5mm. A circle was drawn around one of the corner solder balls and then a linear pattern created along one of the rows of balls. As shown in Figure 5.7, the spacing was adjusted until a circle was centered over each of the balls. In this way the spacing was determined to be 1.044mm.

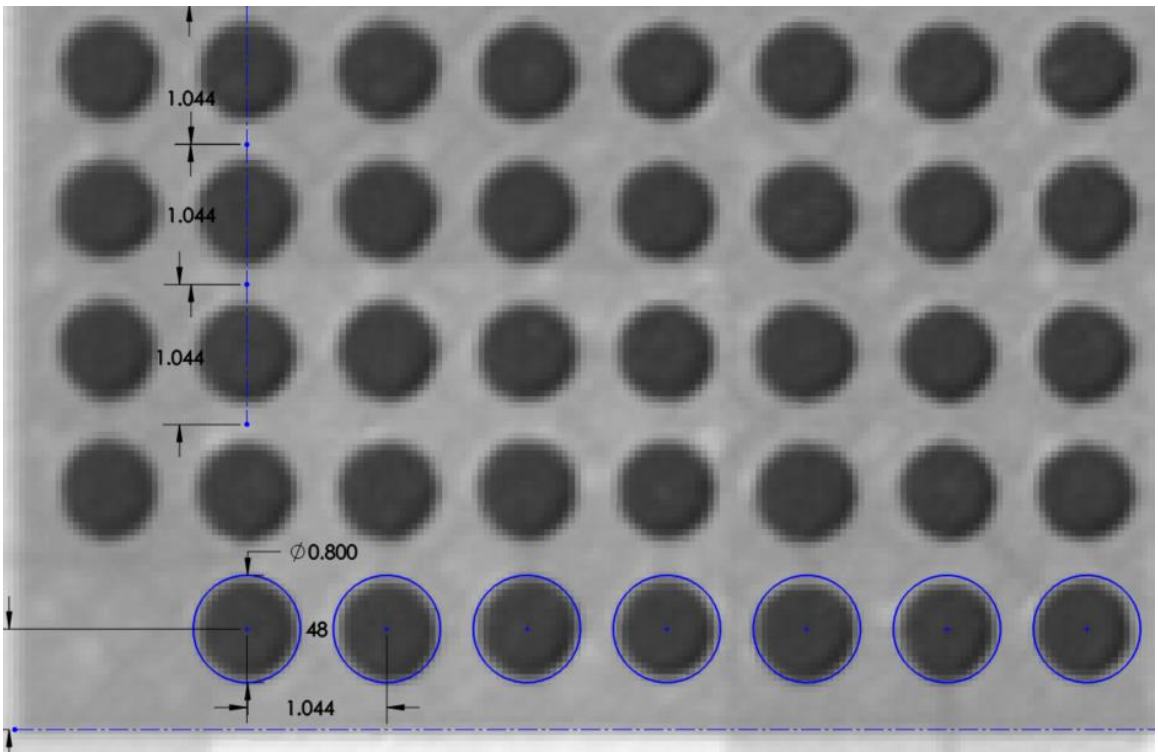

Figure 5.7: CAD showing the spacing between the solder balls.

Once the spacing was determined, a program was written in MatLab to calculate the location of each of the inspection points. Figures 5.8 and 5.9 show how the inspection

points were chosen in relation to the solder balls. To increase throughput, the solder balls were grouped in 3x3 grids, and data was taken at the center of each grid. Along each edge there is a single row of solder balls not covered by the grids, so they were divided into strings of three and data taken over the middle ball. In this way, every solder ball is either directly under or adjacent to an inspection location and therefore any defect within the ball able to strongly affect the acquired signal. The location of each inspection point stays the same whether the chip is inspected section by section or the entire chip at once, the only difference is the location of the excitation point and how much area of the chip is inspected per experiment.

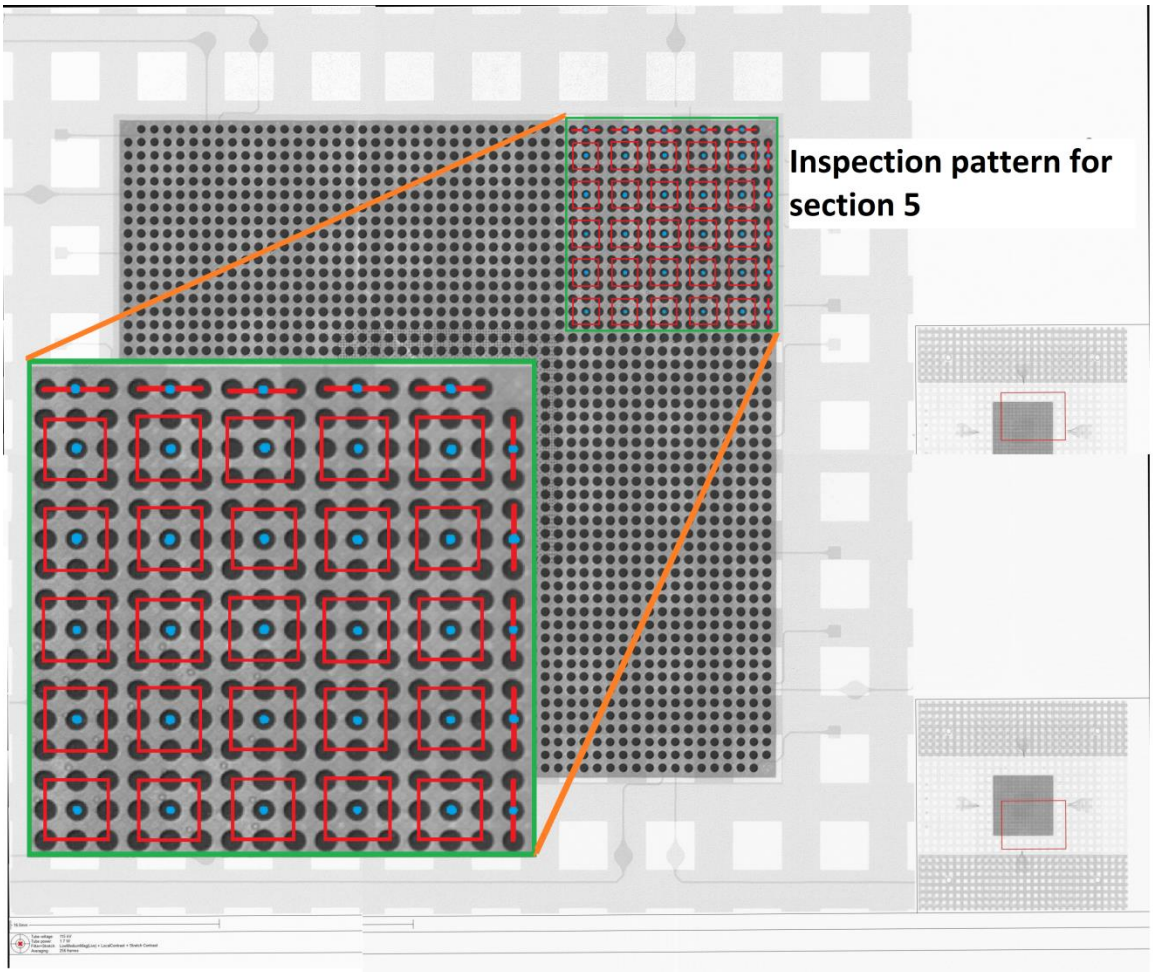

Figure 5.8: Inspection pattern for section 5 overlaid on the chip x-ray. Pattern is similar for all other sections.

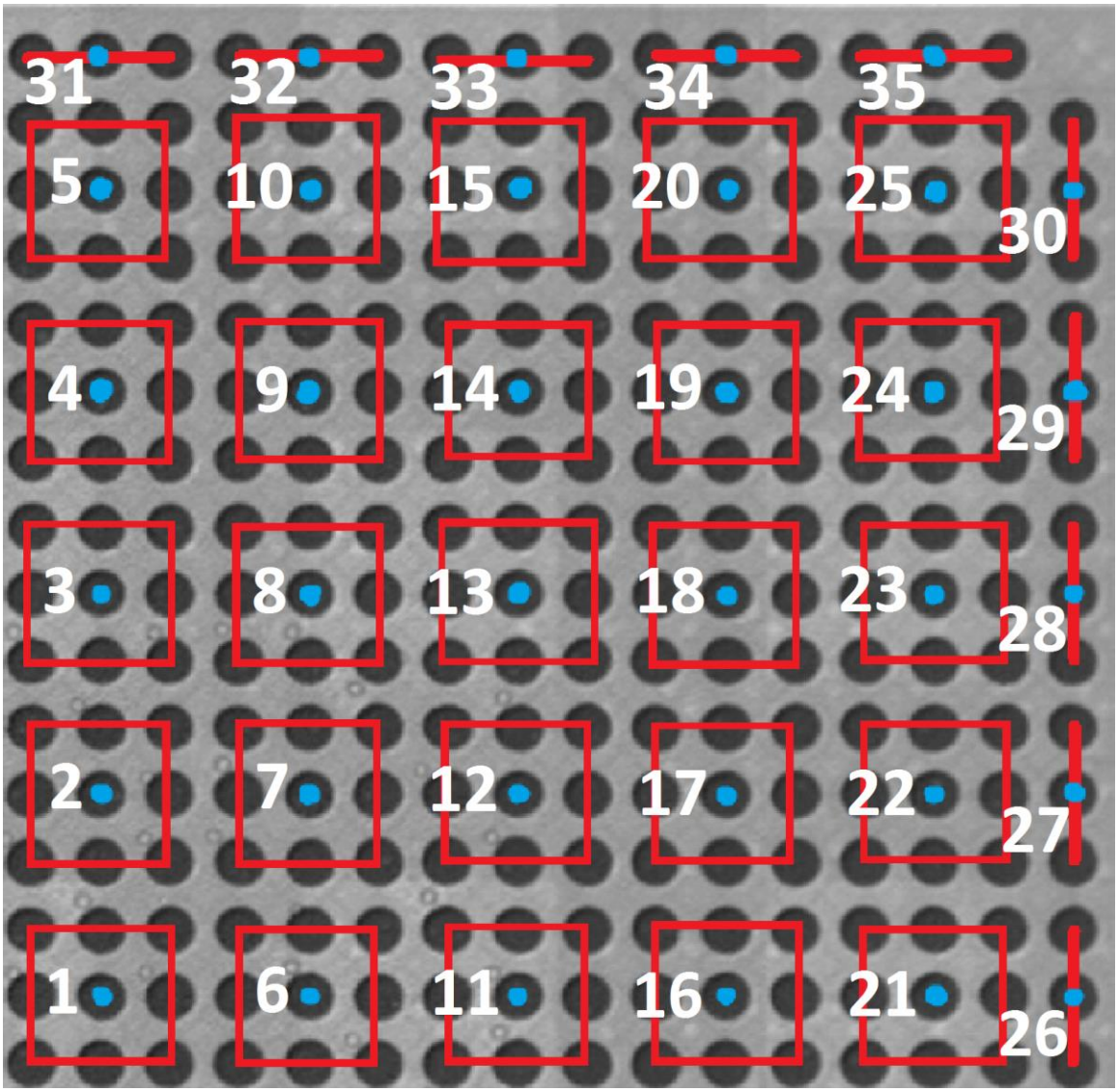

Figure 5.9: Close-up of the inspection patterned for section 5 overlaid on the chip x-ray along with the inspection point numbering.

5.3 Damage Threshold Limit for CISCO Chips

The laser ultrasonic inspection operates in the thermoelastic regime. Therefore, before data could be taken on the CISCO chips the damage threshold needed to be determined. As no previous data was readily available for the substrate, this was done experimentally. Using a beam area of ~3.6mm^2 for the substrate, a single beam of varying powers was made incident on the surface for ten minutes and then the surface inspected for signs of damage. Signs of damage included flashes of light emitted from the incident point during inspection, pitting, burnt marks, large degree of color change, and the like. Examples of damage to the substrate surface can be seen in Figure 5.10. Once the sample had been confirmed damage free, the laser was incremented by 10mW and the test repeated. Once damage was detected the max allowable power level was set at 20mW below it to have a margin of safety. It was found that the substrate started to be noticeably damaged at 70mW and the FC at around 220mW. Dixon *et al.* reported that for single-crystal silicon the thermoablation regime begins around $0.24J/cm^2$ [34]. 220mW average laser power with an incident area of $3.6mm^2$ translates to $\sim 0.3J/cm^2$. Due to the uncertainty in the incident spot size and the difficulty determining the exact at which power the damage starts, the threshold found here seems reasonable. Therefore, for a single incident point the maximum power was set to 50mW and 200mW for the substrate and FC respectively.

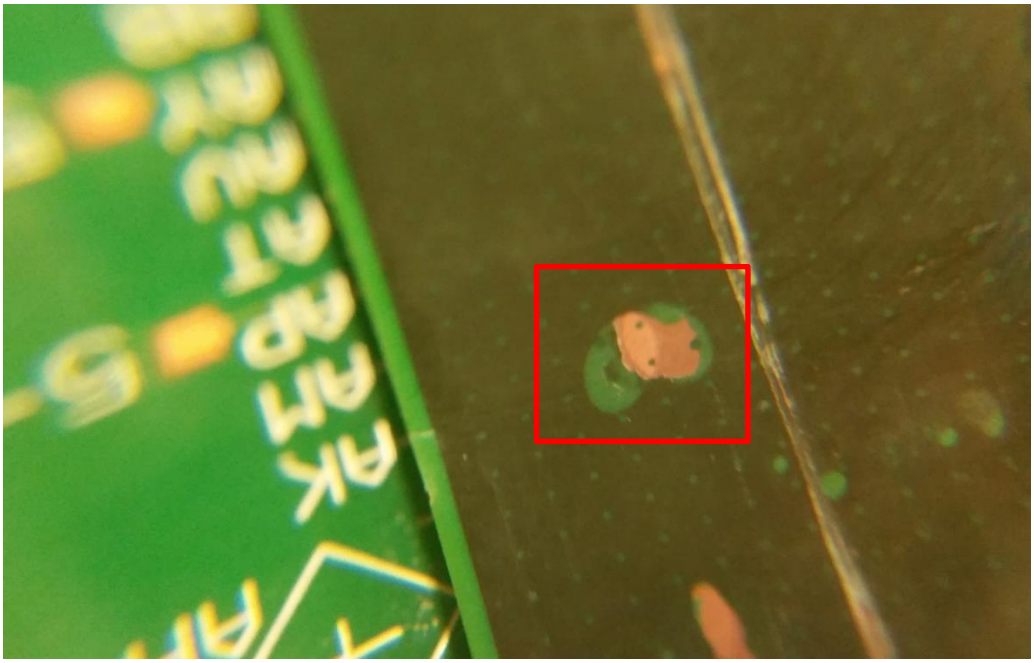

Figure 5.10: Surface of substrate after damage threshold test. Ablation marks clearly seen.

5.4 Repeatability test

During the evaluation period of this research, a set of tests were performed to assess the repeatability of the results obtained from the new system. Board #123 from CISCO was marked as defect free, so inspections were conducted on it to generate the reference signals to which the data from other boards would be compared. To evaluate the repeatability of the system 4 inspections were conducted on board #123 back-to-back using identical inspection parameters and then the result were compared using the MCC method. For the sake of time only data on section 1 of board #123 was taken instead of all eight sections. Table 5.1 lists the parameters used for the experiments. Theoretically, because all the inspections within any one test were conducted on the same board with the exact same parameters, all the MCC values should be zero. However, because of the

random error present in any experiments it is expected that instead of the MCCs being zero, all MCC values for the comparisons should be very low and close together. For the first test, shown in Figure 5.11, the MCC values were higher and not as consistent as expected. Preliminary comparisons between different boards suggested that a threshold value of ~0.025 should be used to determine whether an inspection point is good or bad. If the MCC is below 0.025 the point is good, if it is above 0.025 the point is bad. Having MCC values, from repeated tests on the same board, of almost 1/3 of the suggested threshold was considered not sufficient. To further confirm the existence of the problem another set of inspections was conducted on board 41. As can be seen in Figure 5.12 the results show similar inconsistencies in the MCC values as compared to the test on board 123. To isolate the problem, a series of tests were run while holding all parameters but one constant.

Table 5.1: Experimental parameters for repeatability test

Parameter / **Experiment**	**Total Laser Power (mW)**	**Sampling rate (MS/s)**	**# of samples**	**Signals average per inspection point**
Repeatability test	50	50	3000	128

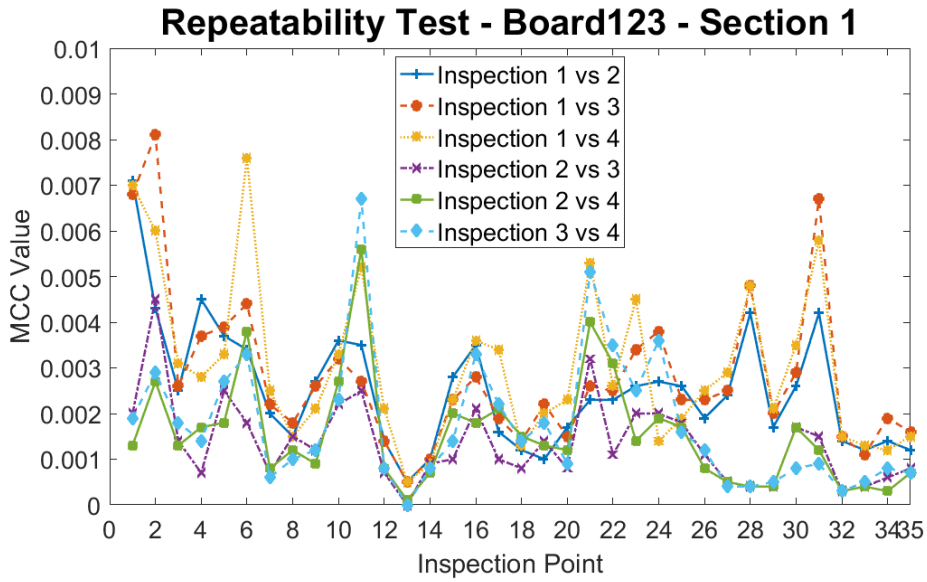

Figure 5.11: Results of the repeatability test for section 1 of board 123. The MCC values are not consistent which suggests that there is some factor causing variations in the inspections. Sampling rate: 50MS/s, # of signals averaged: 128.

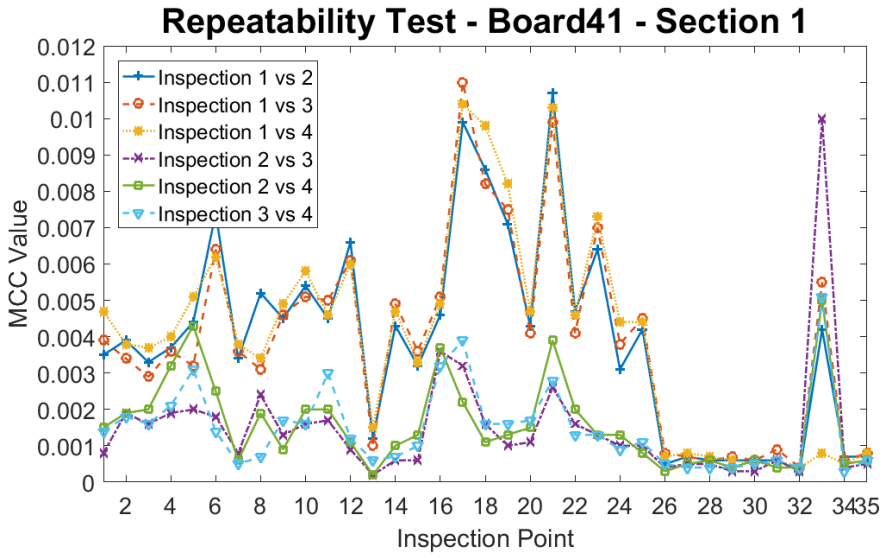

Figure 5.12: Results of the repeatability test for section 1 of board 41. As for Figure (refer to previous Figure), the MCC values are not consistent which again suggests that there is some factor causing variations in the inspections. Sampling rate: 50MS/s, # of s

First a test was run to examine if the laser stage positioning was repeatable. Using the Arcus manual control window the laser incident point was moved under the camera and the vision software was used to measure the incident point offset. The laser was then moved in varying directions before being reset back to the original coordinates and the offset noted again. The offsets were all the same, so it was concluded that the issue was not in the laser stage.

To check if wobble in the autofocus system was the culprit a set of tests was run with the autofocus system disabled. This did not produce any useful results, as many of the inspection points had very high MCC values as a result of insufficient light being collected to produce a clean signal. To eliminate this problem a set of 5 manual inspections was performed on 3 inspection points. The laser was moved into position and the interferometer set to take data at the inspection point. The autofocus program was run and then 5 sets of data were taken at that point. The interferometer was moved to the next point, the autofocus program run, and 5 sets of data collected. This was repeated for one more point. The signals for the 5 inspections at each point were visually compared to each other and found to be a good match. This suggested the issue was in either the autofocus system or the sample stage.

Next, a repeat of this last experiment was run but this time with the autofocus system fully operational. The results of this experiment were visually inspected as before and also found to have very similar signals. Therefore, the problem with repeatability was determined to most likely lie with the sample stage. The sample stage was closely examined, and it was found that if a sufficient force was applied, a small amount of play in the yaw was detected. See Figure 5.13 for a visual. The manufacturer of the stage was

contacted and they indicated that the issue was that the bearings had lost their preloading. The stage was partially taken apart and preloading applied to one of the bearings; the stage was then reassembled.

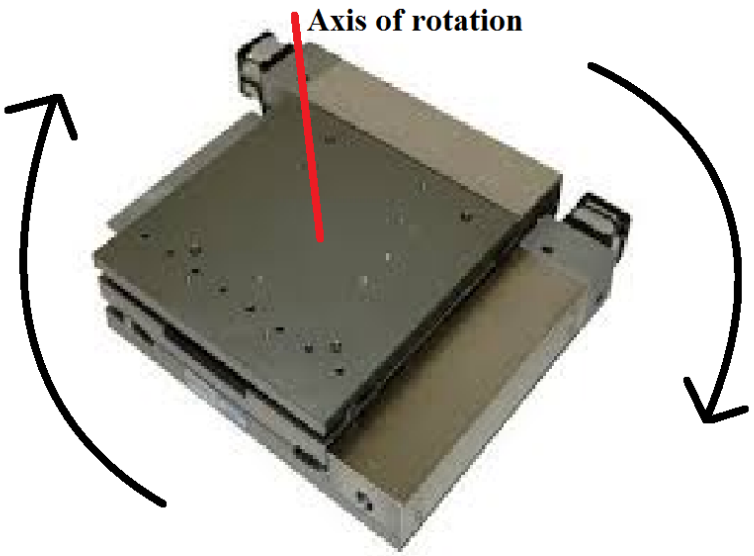

Figure 5.13: The sample stage was found to be able to rotate slightly around the axis shown.

Table 5.2: Updated experimental parameters for repeatability test

Parameter / **Experiment**	**Total Laser Power (mW)**	**Sampling rate (MS/s)**	**# of samples**	**Signals average per inspection point**
Repeatability test	50	100	6000	256

For the next test, an increased sampling rate and signal averages were chosen so as to further reduce any signal noise. The new parameters are shown in table 5.2. The results from the new test are shown in Figure 5.14. The results show much more

consistent MCC values for the comparisons then before the preloading of the stage bearing which indicates that this was the problem. Therefore, preloading for the other bearing was done and 3 more repeatability tests were run and the results shown in Figures 5.15, 5.16, and 5.17 respectively. Except for a spike at inspection point 23 in the first test, all inspection points show greater consistency and lower MCC values than for the previous tests. This spike is thought to be caused by some random variation as tests 2 and 3 do not exhibit any similar spikes in the MCC values. From this study the repeatability of the new system has been shown.

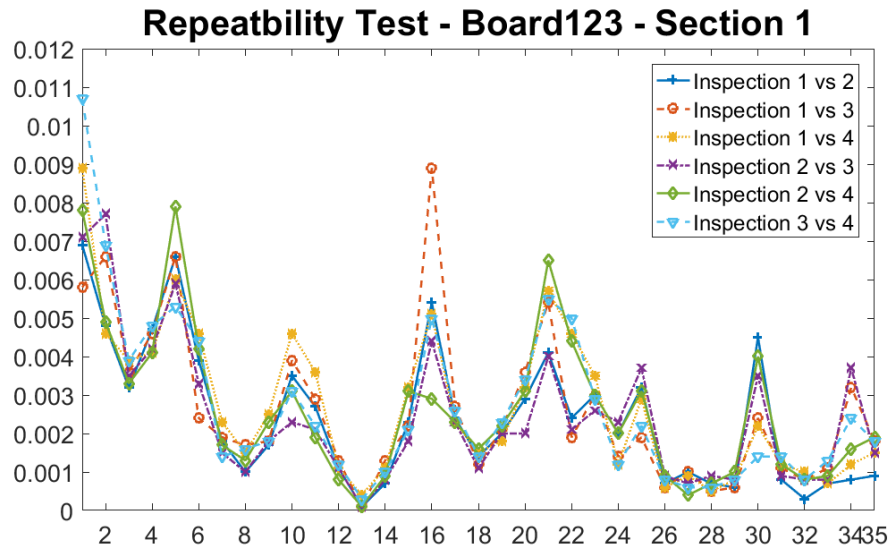

Figure 5.14: Results of the repeatability test for sec. 1 of board 123 after the preloading in one of the rails had been reset. It is obvious that the MCC values are much more consistent which suggests that the play in the sample positioning stage was indeed the issue

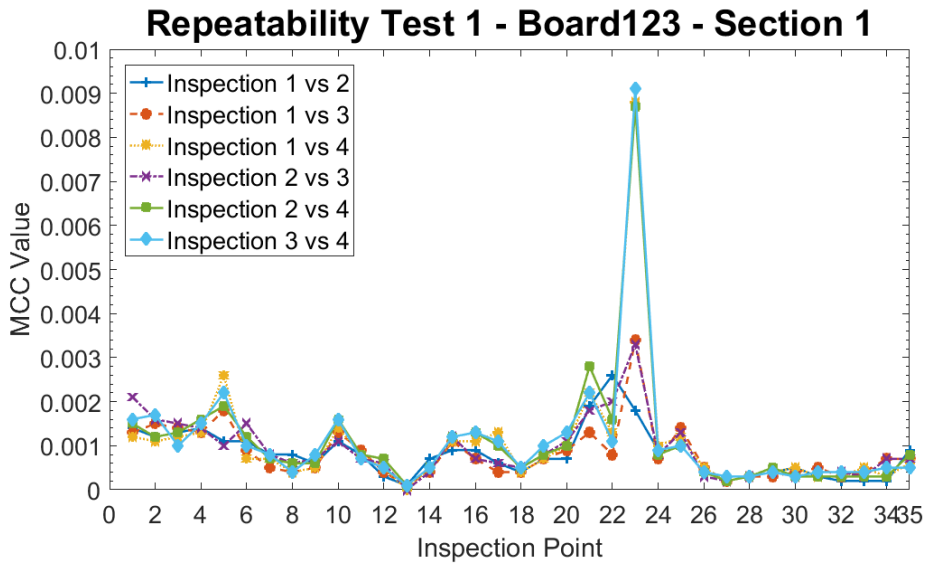

Figure 5.15: Results of the 1st repeatability test for sec. 1 of board 123 after the sample positioning stage had been completely repaired and with the higher sampling frequency and increased number of averages. Spike expected to be an outlier.

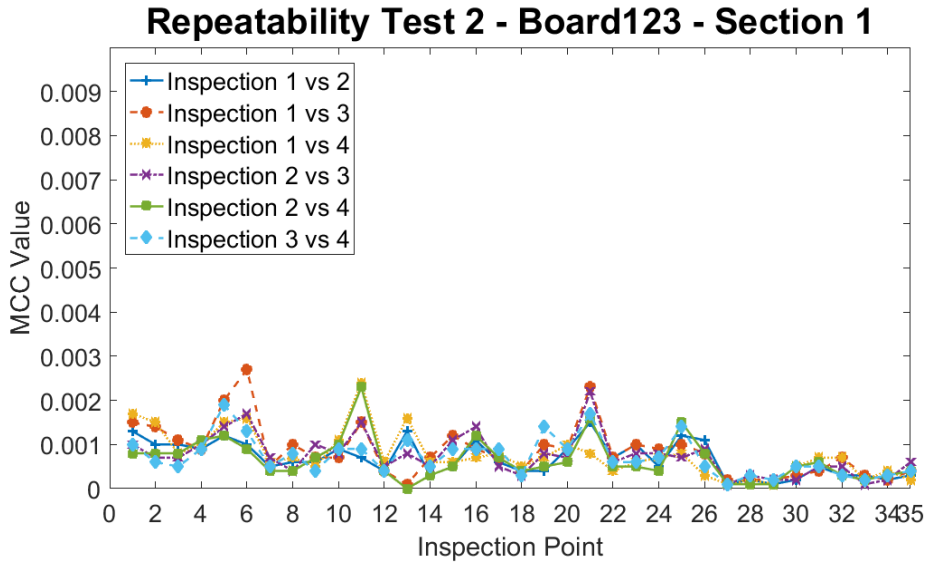

Figure 5.16: Results of the 2nd repeatability test for sec. 1 of board 123 after the sample positioning stage had been completely repaired and with the higher sampling frequency and increased number of averages. There is no large spike at inspection point 23.

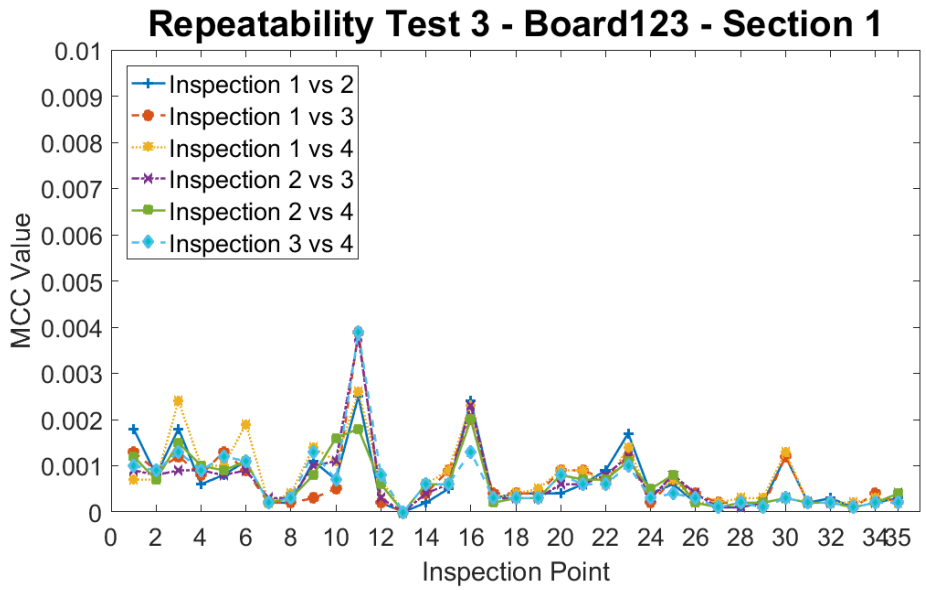

Figure 5.17: Results of the 3rd repeatability test for sec. 1 of board 123 after the sample positioning stage had been completely repaired and with the higher sampling frequency and increased number of averages. Once again there are no large spikes.

5.5 Power advantage for double beam system

One of the major incentives to develop this new system was the desire to deliver power levels to the device under inspection (DUI) not possible for a single excitation point. This is possible with the two beam system because the angle of the rotational stages can be set so that the excitation points have some gap between them rather than them overlapping. The power delivered over each fiber can thus be set to the maximum value for the DUI, and in this way twice as much energy can used in the inspection than is possible with the single beam system. This in turn will greatly increase the strength of the generated ultrasounds. To investigate the benefits of the double excitation points, a series of tests was run using either one or two excitation points with different laser power levels. For the single beam tests one of the fibers was removed from its end effector and

the laser from that fiber directed into a light absorbent container. Since the multiplexer splits the power coming from the laser, the output was doubled to compensate for this. For the double excitation point tests the excitation point spacing was set to 1.85mm. Table 5.3 shows the parameters for each test.

Table 5.3: Main Experimental Parameters for Single Beam and Double Beam Experiments

Parameter / Experiment	**Total Average Laser Power (mW)**	**Sampling rate (MS/s)**	**# of samples**	**Signals average per inspection point**
Single Excitation point	30	50	3000	128
Single Excitation point	40	50	3000	128
Single Excitation point	50	50	3000	128
Double Excitation point	40	50	3000	128
Double Excitation point	50	50	3000	128
Double Excitation point	70	50	3000	128
Double Excitation point	90	50	3000	128
Double Excitation point	100	50	3000	128

Once the data was taken MATLAB was used to perform a periodogram power spectral density (PSD) estimate for several of the inspection points. The PSD describes the power present in a signal as a function of frequency, and therefore in using this one

can see how the increase in power from multiple excitation points affects the strength of the frequencies generated. The results for each of the laser powers at each point were graphed together. The result from one of the inspection points, which is representative of the whole, is shown in Figure 5.18. The units of strength are arbitrary, as only the relative strengths are of interest. From the graph, one can clearly see that an increase in the laser power results in an increase in the ultrasonic signal strength. It is important to note that the strength of the signal for 40mW single beam and 40mW double beams are almost identical. This is to be expected if the strength of the signal is mainly dependent on the total energy used. There is a slight discrepancy in the strengths for the single and double beams at 50mW, though this is thought to be caused by slight variations in the laser power during the test. As shown in Figure 5.19, the raw signal was also plotted and the same trend in signal strengths vs total laser power is seen. Figure 5.20 shows a close up of a portion of the signal for clarity. The signal strength for the 100mW test is approximately 2x the strength of the 50mW test. Once again, the single beam and double beam test at 40mW laser power produced similar amplitude signals with the same tests using 50mW producing slightly different amplitude signals as noted before.

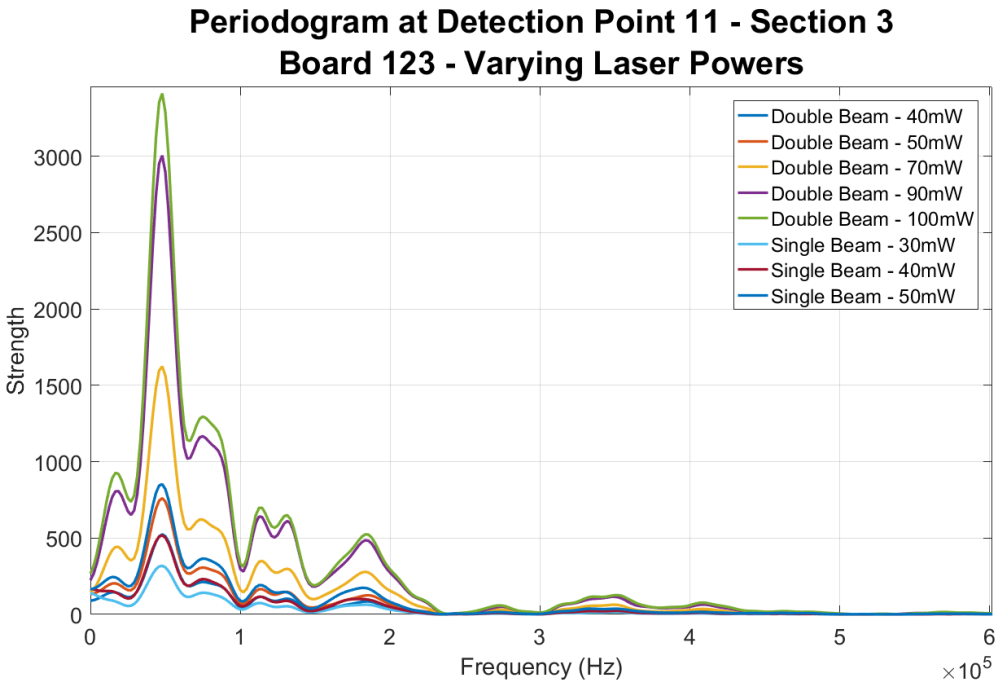

Figure 5.18: Power Spectrum Density for inspection point 11 on section 3 of the CISCO chip.

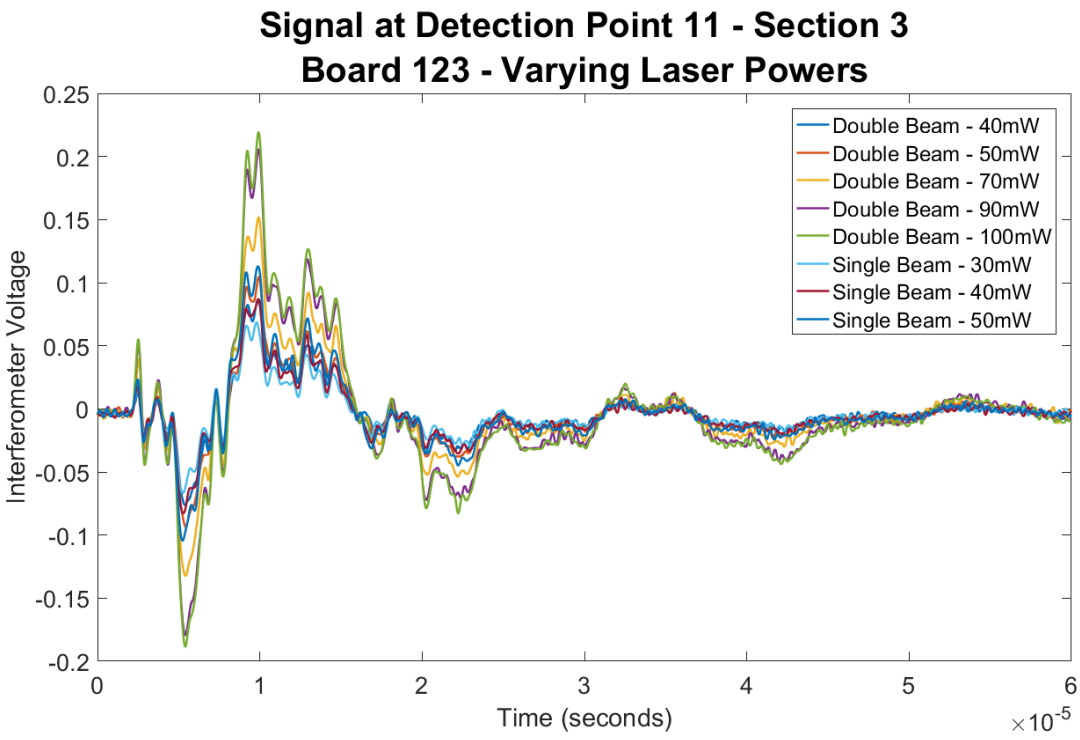

Figure 5.19: Measured signals at inspection point 11, section 3, for varying laser powers.

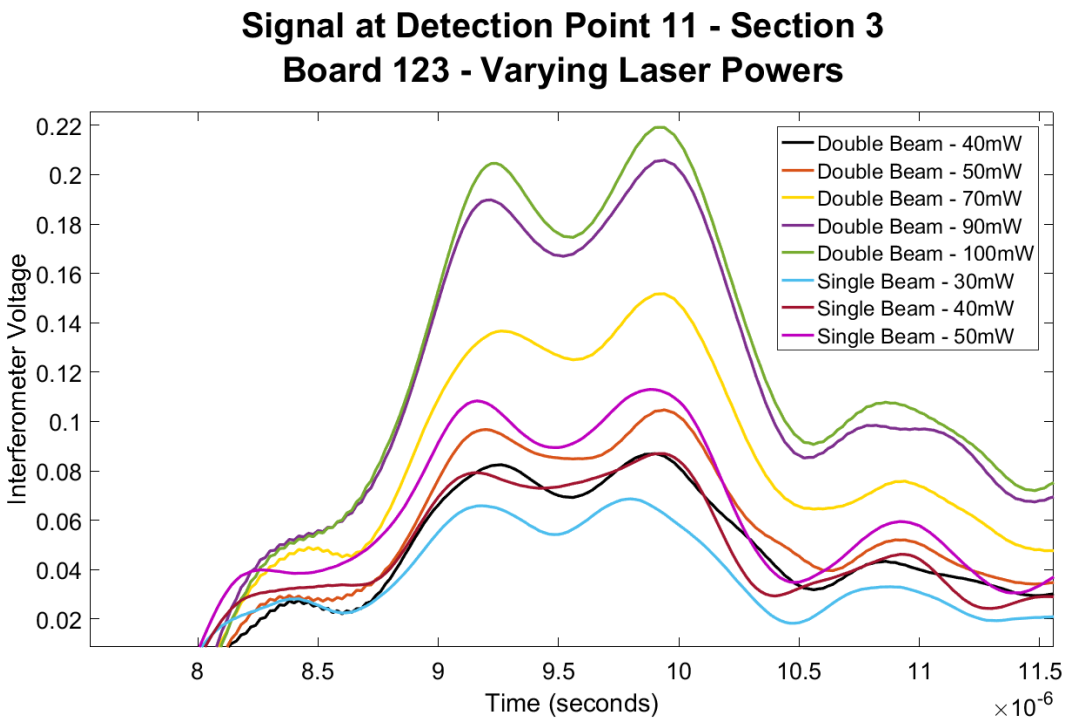

Figure 5.20: Zoomed in view of a portion of Figure 5.19 clearly showing the benefits in using a double beam system

To test the usefulness of having more laser power than a single beam can supply, a set of experiments was run attempting to inspect the entire BGA using either one or two excitation points on the FC. Using a single excitation point at the damage threshold of 200mW, data was taken on boards 123 and 107 and the results compared. As shown in the representative signal at inspection point 17 in Figure 5.21 the signal strength was not strong enough to obtain a clear signal. Because of the low signal to noise ratio, the data from this test is considered meaningless. This shows that the large chip could not be inspected with a system with only a single excitation point.

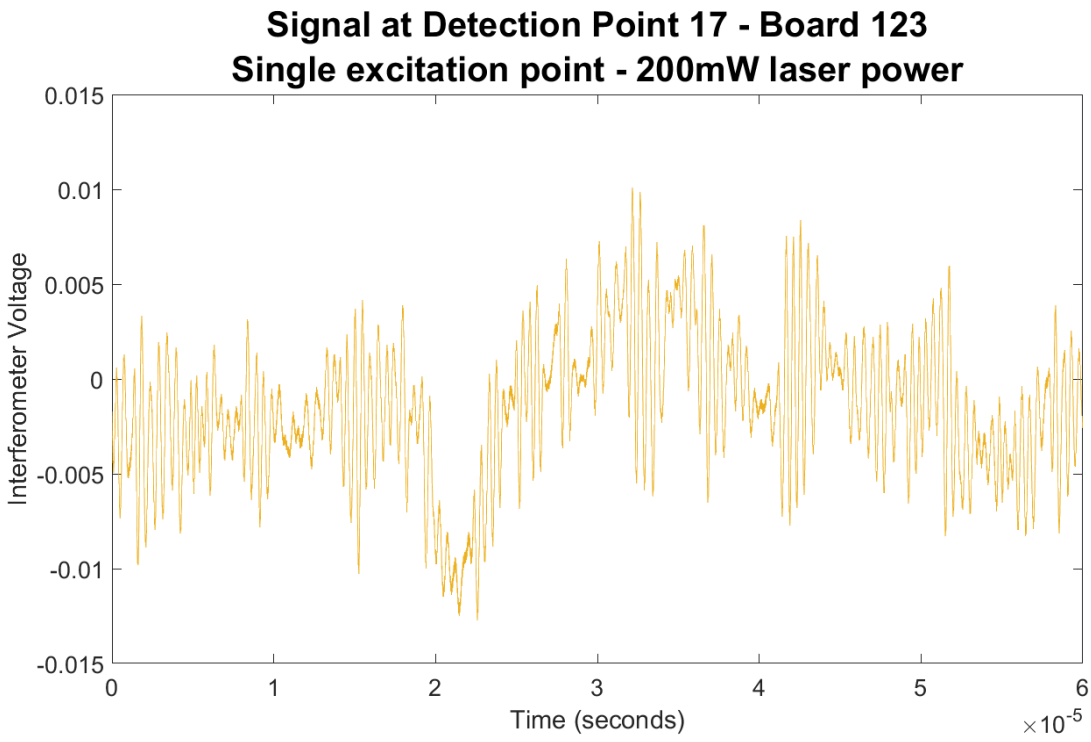

Figure 5.21: Acquired signal at inspection point 17 for the single excitation point experiment

Another experiment was run but this time using two excitation points with a 1.85 center-to-center spacing and 350mW of total laser power. The signal at inspection point 17 of section 3 was again examined, and this time a much clearer signal was obtained as seen in Figure 5.22. With the better quality data obtainable with the double excitation points, the MCC between reference board 123 and board 107 was calculated and the results shown Figure 5.23. Note, at the time the data was taken the configuration of the system did not allow the interferometer to move so as to acquire data on sections 1, 7, or 8.

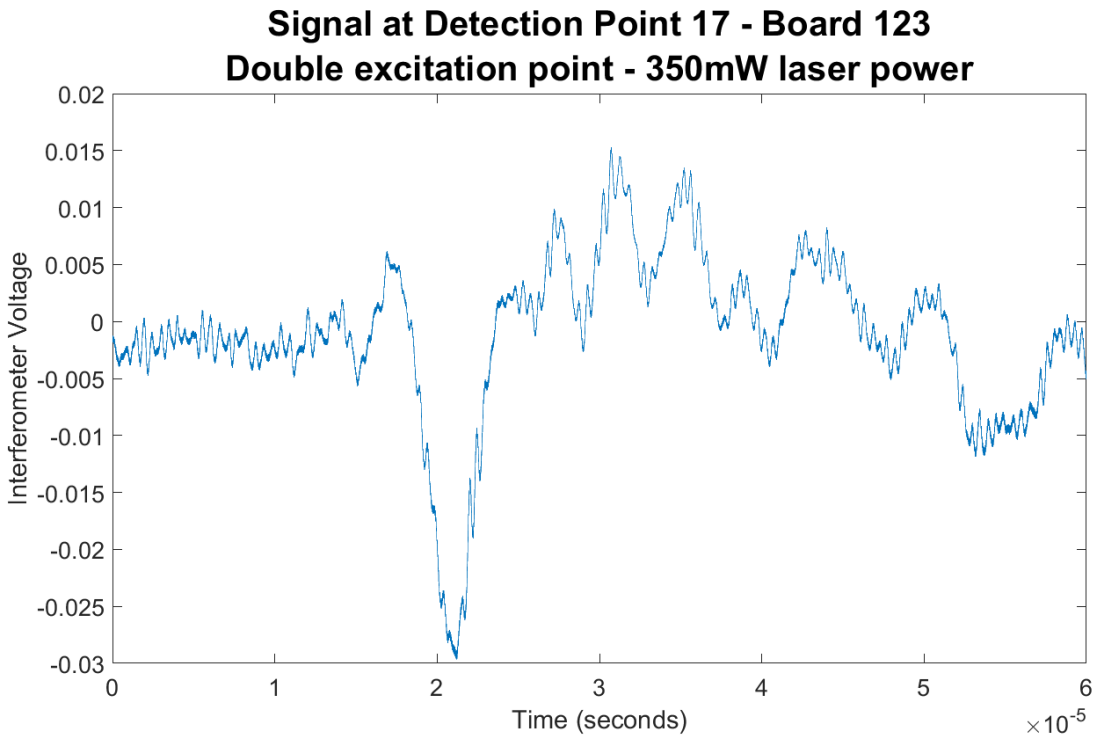

Figure 5.22: Acquired signal at inspection point 17 for the double excitation point experiment

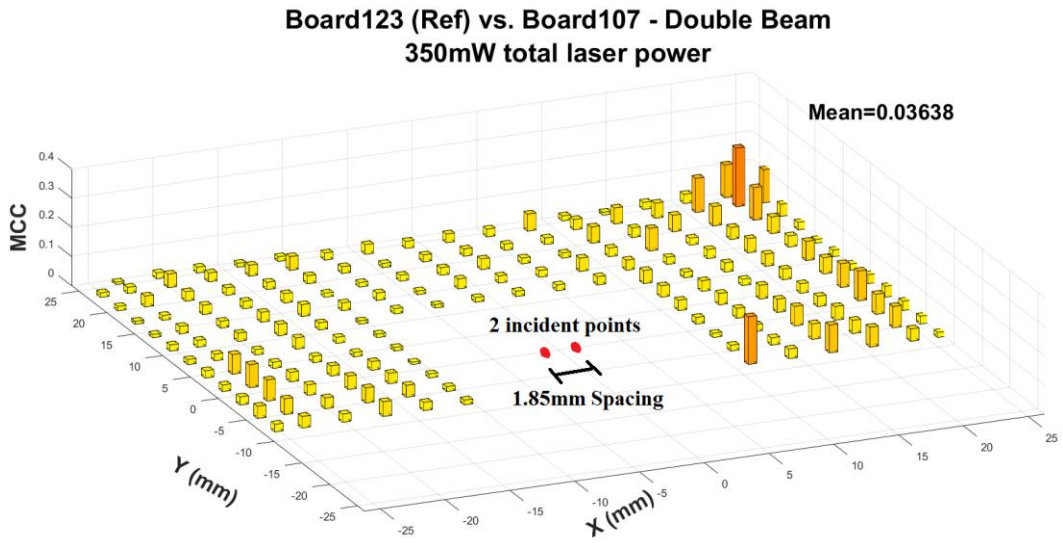

Figure 5.23: MCC plot for double excitation point experiment. The data shown corresponds to sections 2, 3, 4, 5, and 6 of the inspections taken with the sub-sectioning method.

The results from this test were cross-compared to the MCC graphs generated from data taken using the subsection method, and a good match was found. The results from the subsection tests for the same area of the BGA are shown in Figures 5.24 – 5.28. The main features, such as the higher MCC values along the left side of section 2, the slight rise in MCC values in the top left corner of section 3, and the large MCC values in the top left of section 4, are clearly visible for both experiments. From this it is concluded that the use of two excitation points allows enough energy to be delivered to the chip to inspect the entire BGA without the need to subdivide it. The advantage of using two excitation points is thus: simplified code for creating the inspection pattern, increased throughput because the system does not have to take time moving to the different subsections, and increased range of devices the system can inspect.

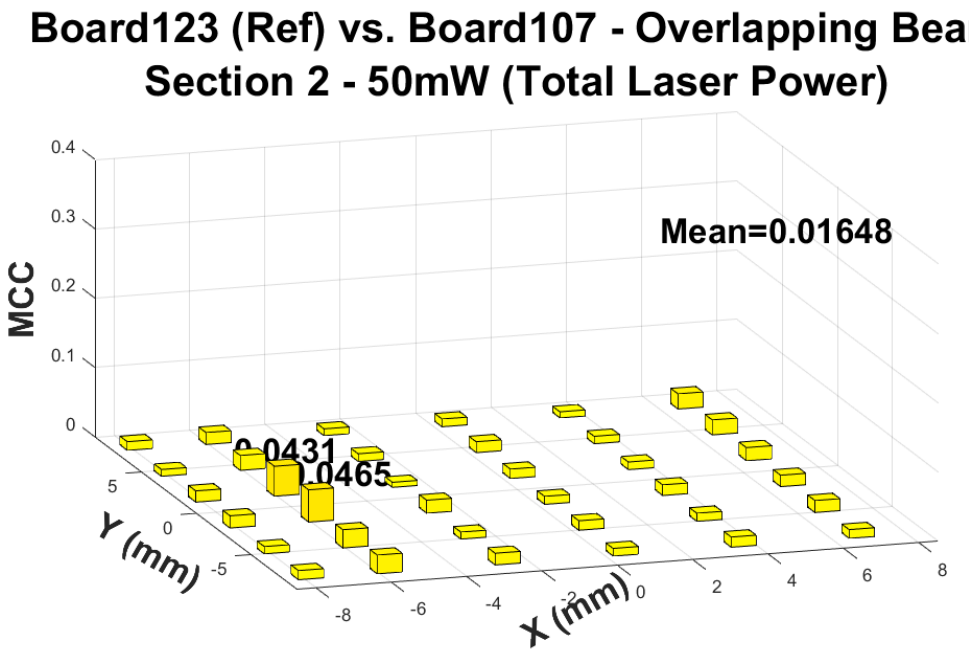

Figure 5.24: MCC plot for section 2 of board 107.

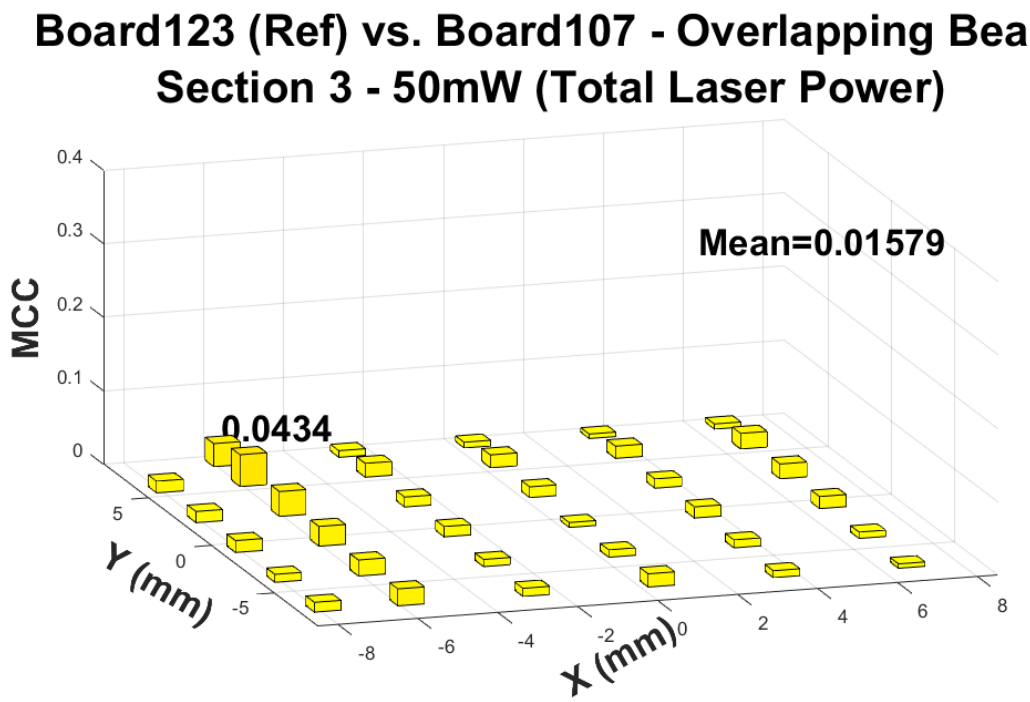

Figure 5.25: MCC plot for section 3 of board 107.

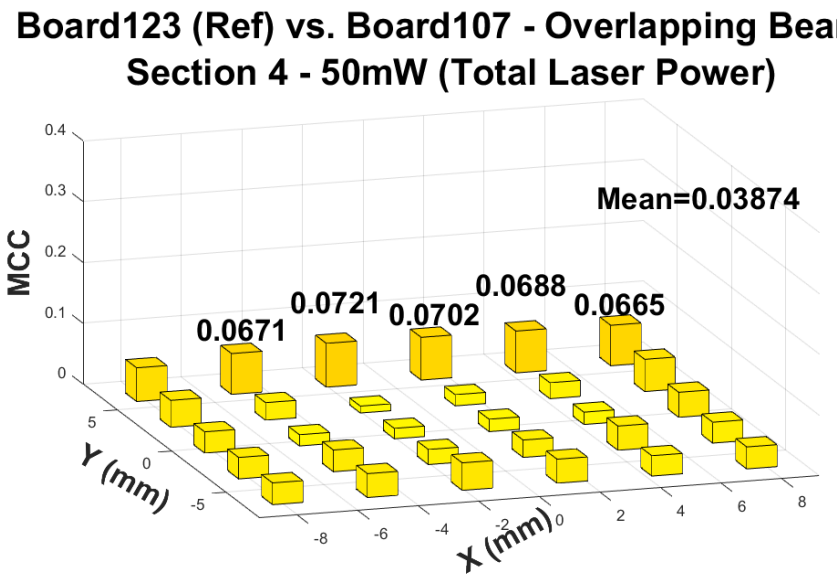

Figure 5.26: MCC plot for section 4 of board 107

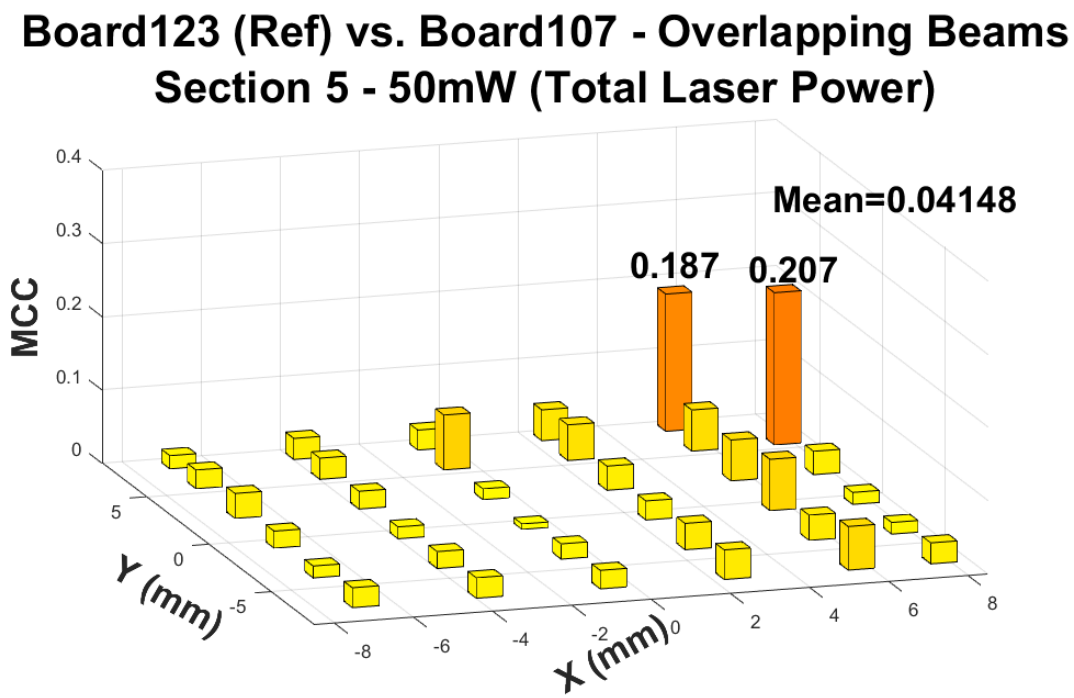

Figure 5.27: MCC plot for section 5 of board 107.

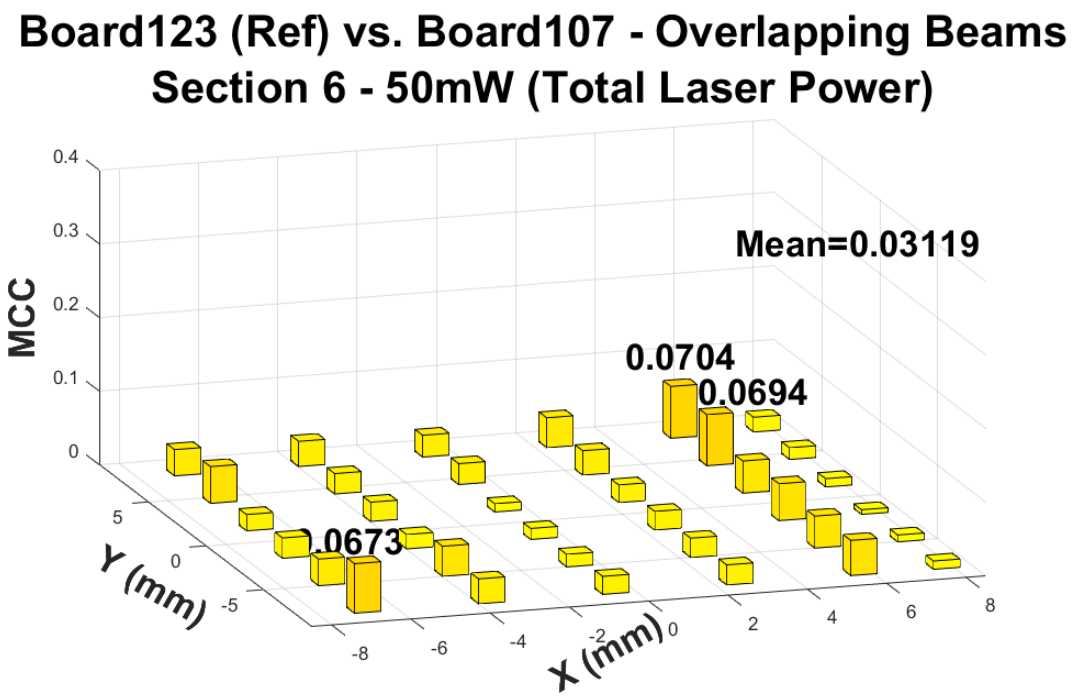

Figure 5.28: MCC plot for section 6 of board 107.

5.6 Equivalency of single beam and overlapping beams

When inspecting significantly small chips the power levels needed might not require the increased power available with two excitation points. In addition, having multiple excitation points might be detrimental, as experience has shown that sometimes data points laying within the excitation region are unusable. So in this situation it is more beneficial to use a single excitation point. Rather than reconfiguring the system to use a single beam, which is a hassle as well as an opportunity to damage the fiber, it is thought that it would be safer and more convenient to simply adjust the angle of the end effectors so the excitation points overlap. While it seems obvious that at the same power level it should not matter whether it is a single excitation point produced with one beam or with

two, it is something that should be verified. To do this a set of tests were run on boards 107, 117, and the reference 123 using both a single beam and a double beam overlapping at the same power level and the results compared. The results of these experiments are shown in Figures 5.29 – 5.31.

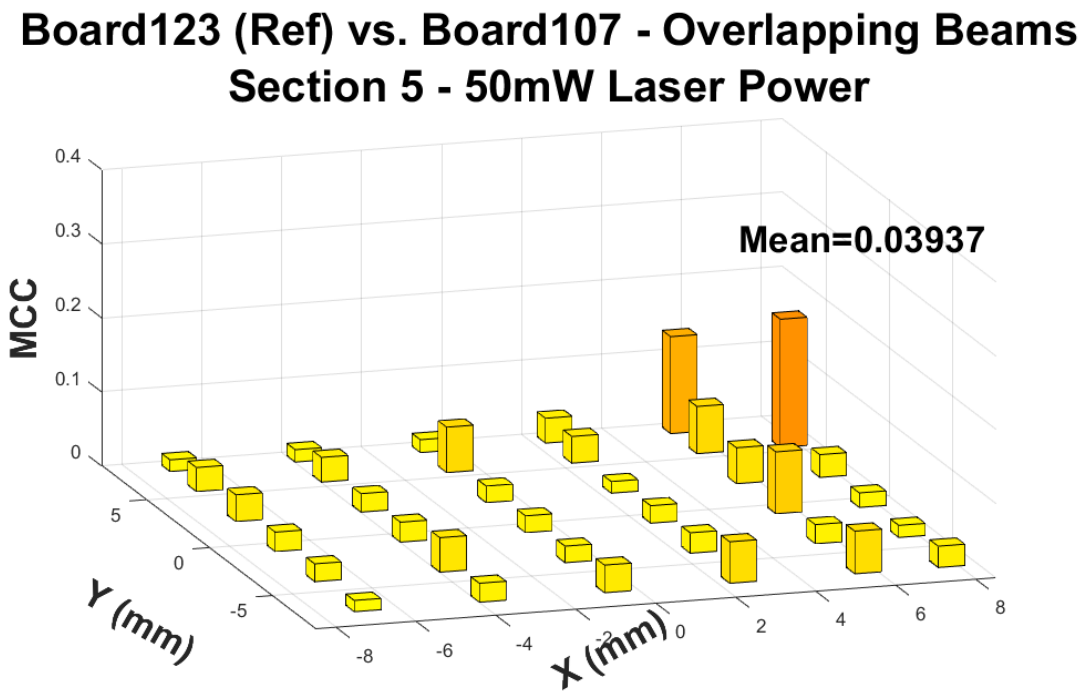

Figure 5.29: MCC plot for section 5 of board 107 vs reference board 123 using overlapping beams.

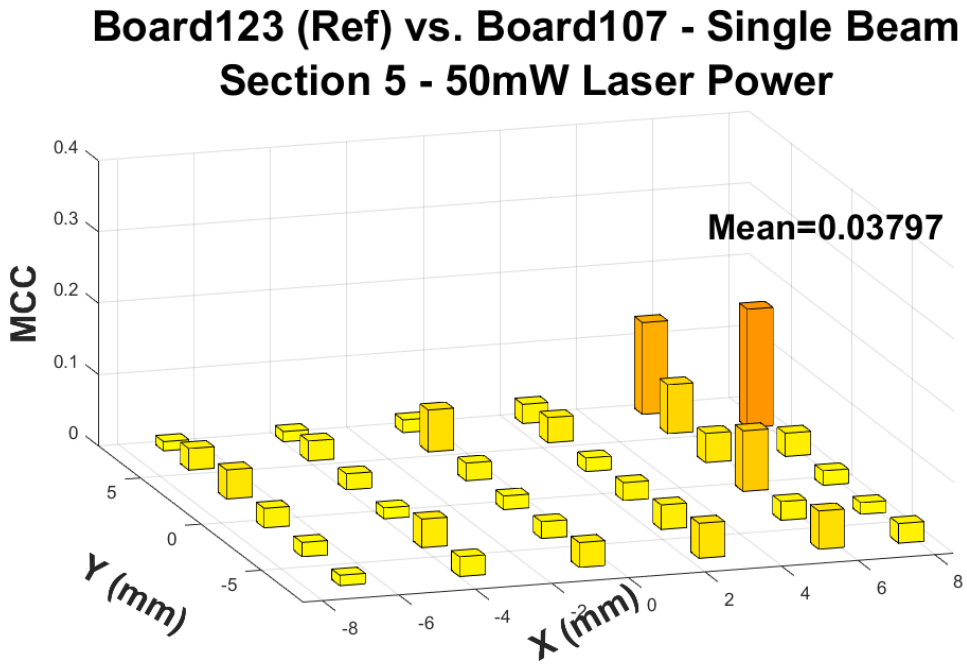

Figure 5.30: MCC plot for section 5 of board 107 vs reference board 123 using a single beam

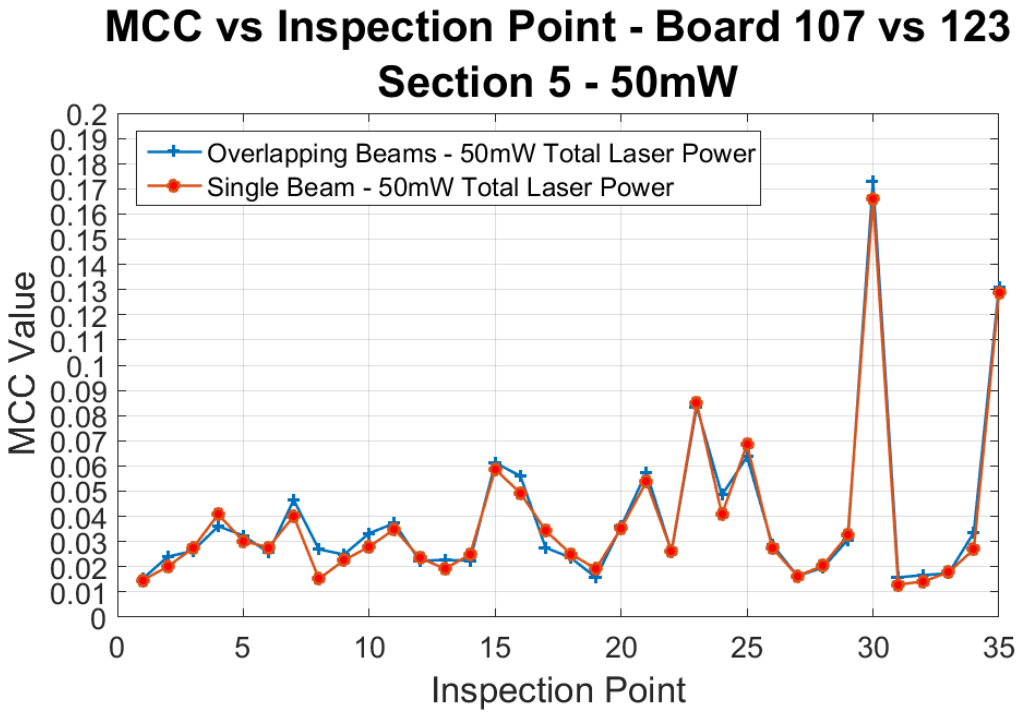

Figure 5.31: Inspection Point vs MCC plot for section 5 of board 107 vs reference board 123 comparing the results from the single beam experiment to the overlapping beam experiment. Any discrepancies are insignificant.

A visual examination shows a great similarity between the two inspection results with all of the features from one inspection showing up in the other. The difference in MCC value inspection point by inspection point was calculated. The minimum value was found to be 0, the max 0.0117, the average 0.00329, and the median 0.0023. The fact that all the features appeared in both inspections and that the MCC values between the two are so close is crucial, as it confirms that the use of overlapping beams is a viable alternative to the single beam system.

Another benefit that comes with using two fiber optic cables instead of one is the smaller fiber core diameter, and therefore smaller bend radius that is possible. In discussion on the topic of bend radius with people in industry, it was noted that typically the short term minimum bend radius is 100x the core jacket diameter, while the long term minimum bend radius is 600x the core jacket diameter. Here minimum bend radius is defined as the smallest radius the fiber can be bent into without the fiber breaking, short term is defined as on the order of seconds, and long term is defined as >20 years. Table 5.4 shows the jacket diameter and minimum long term bend radii for a variety of common fiber core diameters, and Figure 5.32 shows the minimum bend radii verses core diameter in pictorial form. This will become important after a discussion of fiber damage thresholds.

Table 5.4: Common fiber core and jacket diameters vs the minimum long term bend radii.

Core Diameter (um)	Jacket Diameter (um)	Minimum Long Term Bend Radius (mm)
1000	1100	330
800	880	264
600	660	198
500	550	165
400	480	144
200	280	84
50	125	37.5

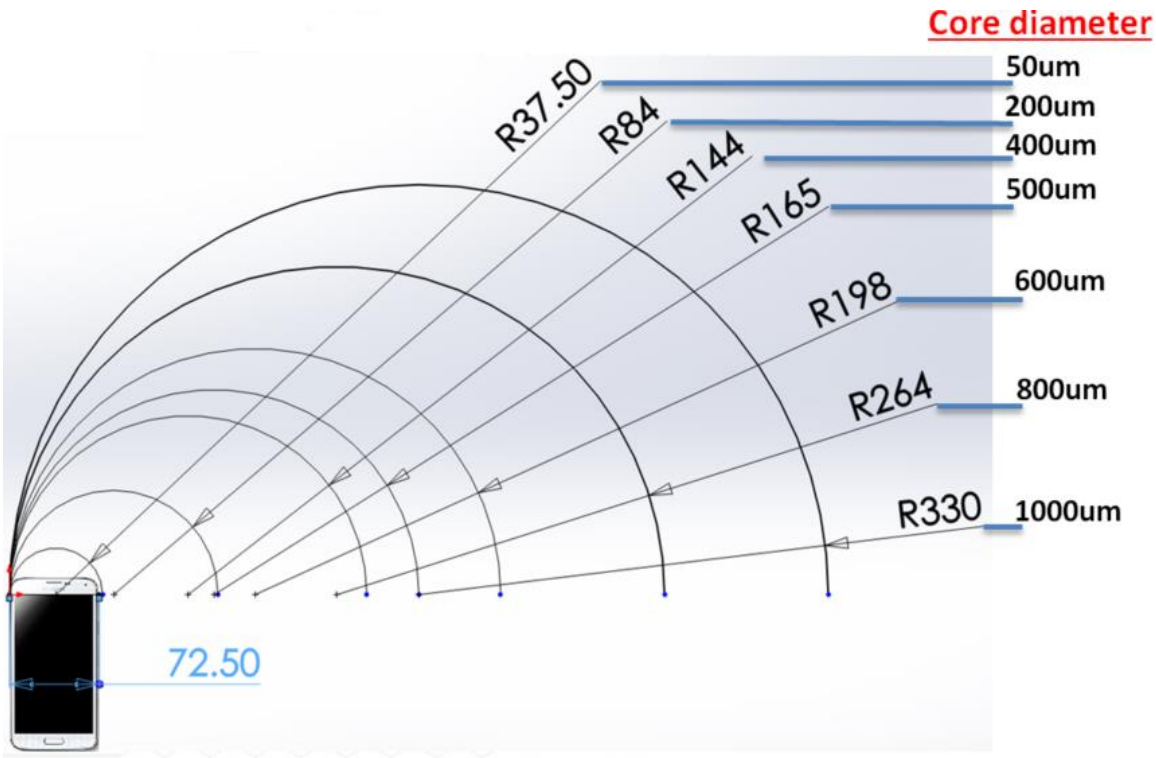

Figure 5.32: Pictorial showing the various minimum long term bend radii for the various fiber core diameters. A scaled picture of a Samsung Galaxy S5 smart phone is shown for reference

When conducting LUI experiments, one must not only consider the damage threshold of the DUI but also the damage threshold of the fiber. The beam profile of the laser used in this system is Gaussian, which is the beam profile for most lasers [35]. The radial intensity of the beam is given by equation 7

$$I(r) = I_o \left[\exp\left(-\frac{2r^2}{w_o^2}\right)\right] \quad (7)$$

where I_o is the intensity at the center of the beam, r is the radius of interest and goes from zero to the beam radius, and w_o is the 1/e^2 radius of the beam. I_o is calculated using equation 8

$$I_o = \mathrm{P}(\infty)\left[\frac{2}{\pi w_o^2}\right] \quad (8)$$

where $\mathrm{P}(\infty)$ is the total instantaneous laser power which can be calculated from the average laser power using equation 9

$$P(\infty) = \frac{\frac{average\ laser\ power\ (in\ Watts)}{laser\ repetition\ rate\ (in\ Hz)}}{pulse\ length\ (in\ seconds)} \quad (9)$$

Using the above equations, the parameters of the laser used in this system, and the laser power set at the damage threshold for the FC of 200mW, the peak power densities for the common fiber core sizes was calculated and the values shown in table 5.5.

Table 5.5: Peak power densities at 200mW total laser power for different fiber core diameter

Fiber Core Diameter (um)	**Peak Power Density Experienced (GW/cm^2)**
1000	1.25
800	1.95
600	3.46
500	4.98
400	7.78
200	31.1
100	125
50	498

Smith *et al.* have reported the intrinsic damage threshold of silica fibers to be 4.75kW/um^2 (47.5 GW/cm^2 or upwards of 3800J/cm^2 for an 8nS pulse) for the bulk material with a surface damage threshold to be much lower. This lower threshold, due to imperfections in the surface polish creating in effect micro lenses which focus the light [33]. Campbell *et al.* reported a surface damage threshold fluence of a 7nS pulse to be 50J/cm^2 [36]. Fiber optic engineers in industry, reported that 50J/cm^2 is the common maximum damage threshold used for short pulses in a fiber. With a 4nS pulse this converts to a maximum power density threshold of 12.5GW/cm^2. The engineers also said that because of variance in the surface finish of the fibers it is general practice to use

a safety factor of 50% when designing any fiber optic system. Therefore, when choosing a fiber for a laser delivery system the maximum peak power density should never exceed 6.25GW/cm^2. Comparing this value to those in table 5.4 it is concluded that in order to carry 200mW average laser power delivered in a 4nS pulse, one would need either a single fiber with a core diameter of 500um or above, or multiple smaller diameter fibers. If the desired average power increased to 400mW, which is the power needed to properly excite the FC of the CISCO board in order to inspect the entire chip at once, one would need a single fiber with a core diameter of approximately 800um. Referencing Figure 5.32, the minimum long term bend radius for this diameter fiber is 264mm. Therefore, in order to bend in a semicircle, a minimum of over half a meter of space is required. This is not practical if a compact system is desired. However, a system with two fibers of just 450um core diameter could be used to safely carry the same total power. This would allow the fibers to make a semicircular bend in only 0.297 meters of space – a reduction of over 43%. This is one of the major benefits of the multi-beam system; for the same power levels a fiber optic array system can be made much more compact than a single fiber system.

5.6 Evaluation of CISCO FCBGA

The new optical fiber array LUI system was used to inspect two of the CISCO FCBGA packages and the results cross-correlated with destructive cross-section testing to evaluate the performance of the new system. Cross-section testing consists of immersing the board in an epoxy resin and then leaving it in a vacuum chamber overnight to remove

trapped air bubbles and cure. The epoxy serves to prevent defects forming from the mechanical stresses experienced during the cutting/grinding stage. Beginning at one edge of the cured block, the material is ground away to reveal the cross-section of interest (for examining solder joints this point is usually located midway through a row of solder balls). As the target location is approached, a series of successively finer grit abrasive materials are used. This leaves a finely polished face on the cross-section, shown in Figure 5.33, which is useful for the next step of the testing: analysis.

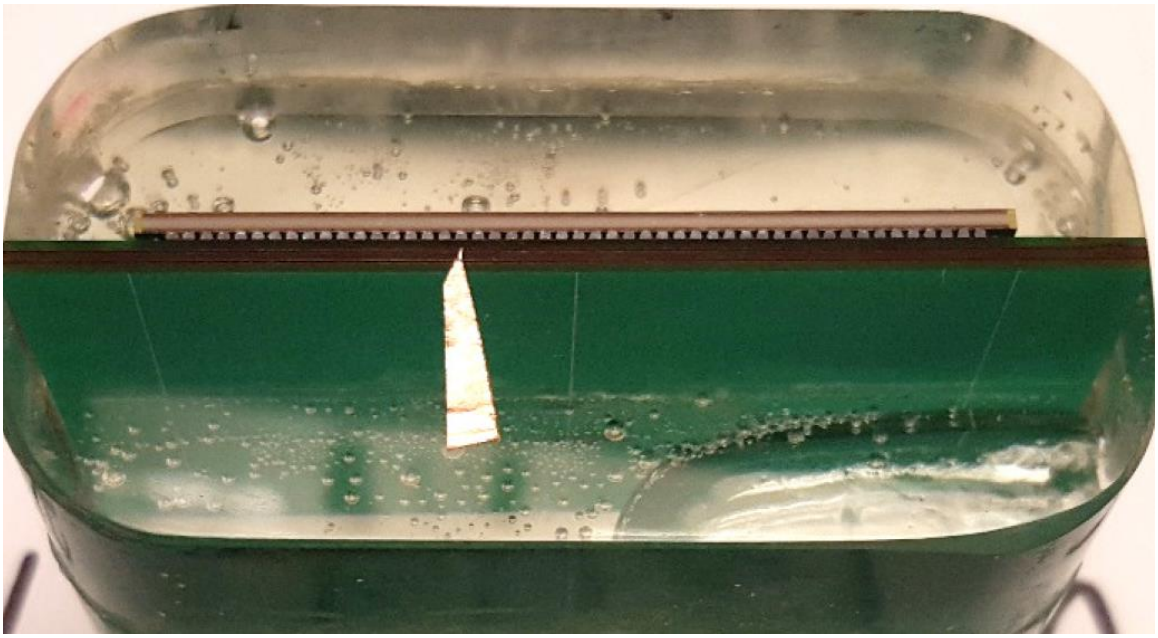

Figure 5.33: CISCO FCBGA embedded in epoxy with cross-sectioned face showing

Scanning Electron Microscopy (SEM) was used to detect the presence of cracks and delamination of the solder balls. Due to the labor intensive nature of cross-sectioning, a single row of solder balls was analyzed for each of the boards. This row of solder balls

runs along the top edge of the board and is shown in Figure 5.34. In this section, the LUI and destructive testing results for one board will be presented followed by the results for the other board. Any inspection performed on the board of interest was also performed on board #123 to generate the reference signal. Additionally, two different excitation spot patterns were used: overlapping excitation spots (OES) and double excitation spots (DES). All the cross-section testing presented in this work was conducted by CISCO.

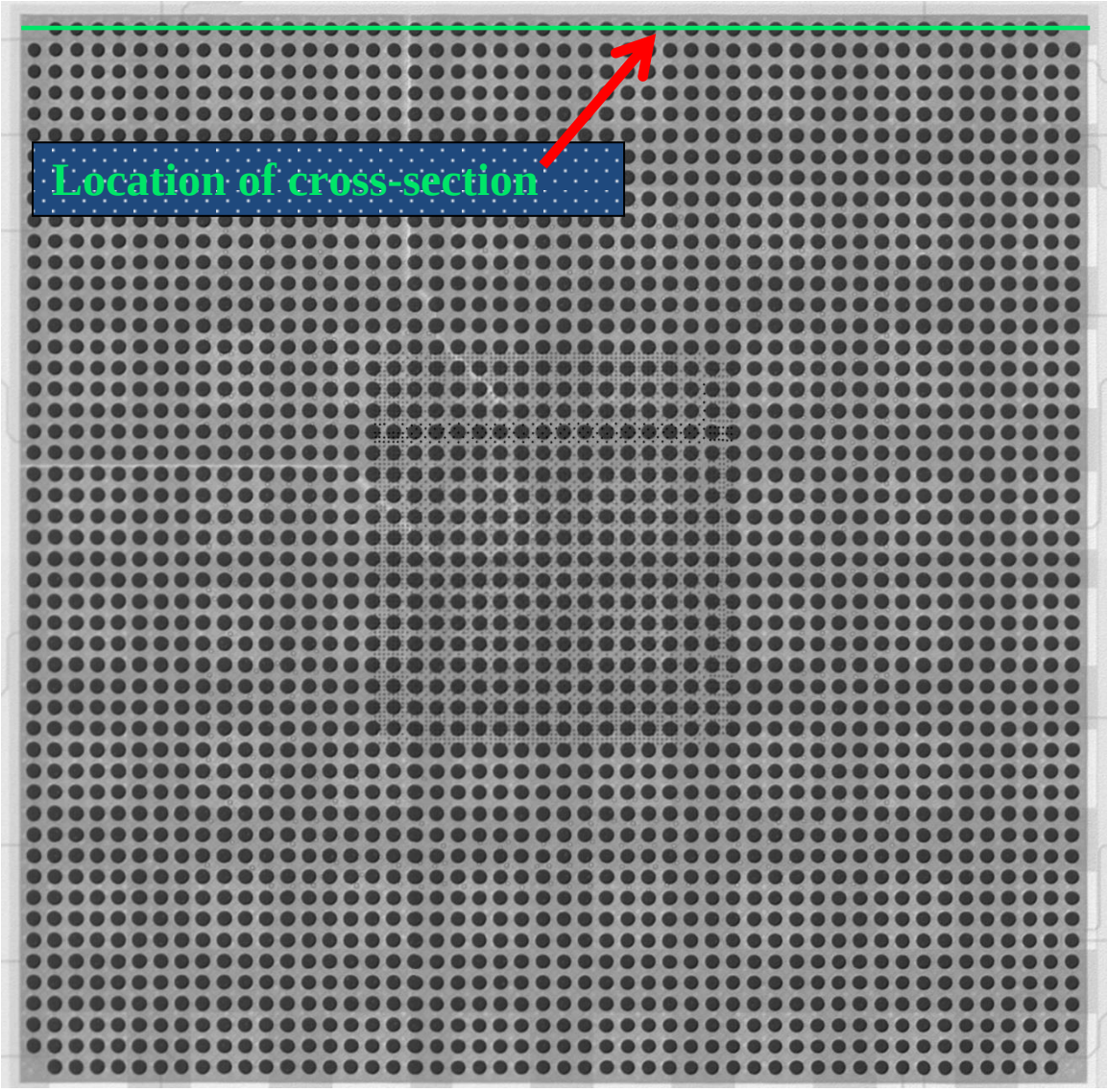

Figure 5.34: X-Ray of CISCO FCBGA showing the location of the cross-section cut

5.6.1 LUI and cross-section results for board #29

Both LUI and cross-sectional analysis were performed on CISCO's FCBGA board #29. The results are presented below. No information concerning the type/s of stress testing applied to the board was provided. Table 5.6 shows the experimental parameter for the LUI test on board #29. The LUI results are shown in Figures 5.34, 5.39, and 5.40 while the SEM results are shown in Figures 5.36-5.38, and 5.41-5.43. Because the cross-section was across only the top row of solder balls, only the results from sections 3, 4, and 5 are presented here. In those sections it is the inspection points at the top edge that are of interest.

Table 5.6: Experimental parameter for LUI of board #29

Parameter / Experiment	**Total Laser Power (mW)**	**Sampling rate (MS/s)**	**# of samples**	**Signals average per inspection point**
Board #29	50	50	3000	128

Figure 5.34 shows the results from section 3. It can be seen that along the top row there are high MCC values for the two inspection points on the left and low MCC values for the other three points. Comparing this to the SEM image in Figure 5.35, it is possible to see cracks and delamination of the solder balls at these same locations. The middle inspection point in the row corresponds to solder balls A8 and A9. Here, a low MCC value was calculated and therefore thought to be defect free. However, some very minor

cracking was observed by the SEM. This juxtaposition of results is suspected to be a result of insufficient excitation energy not inducing strong enough ultrasounds to detect the miniscule crack forming. The low MCC values of the other two inspection points indicate no defects at these points. No cracking or laminate separation at these points was confirmed by SEM.

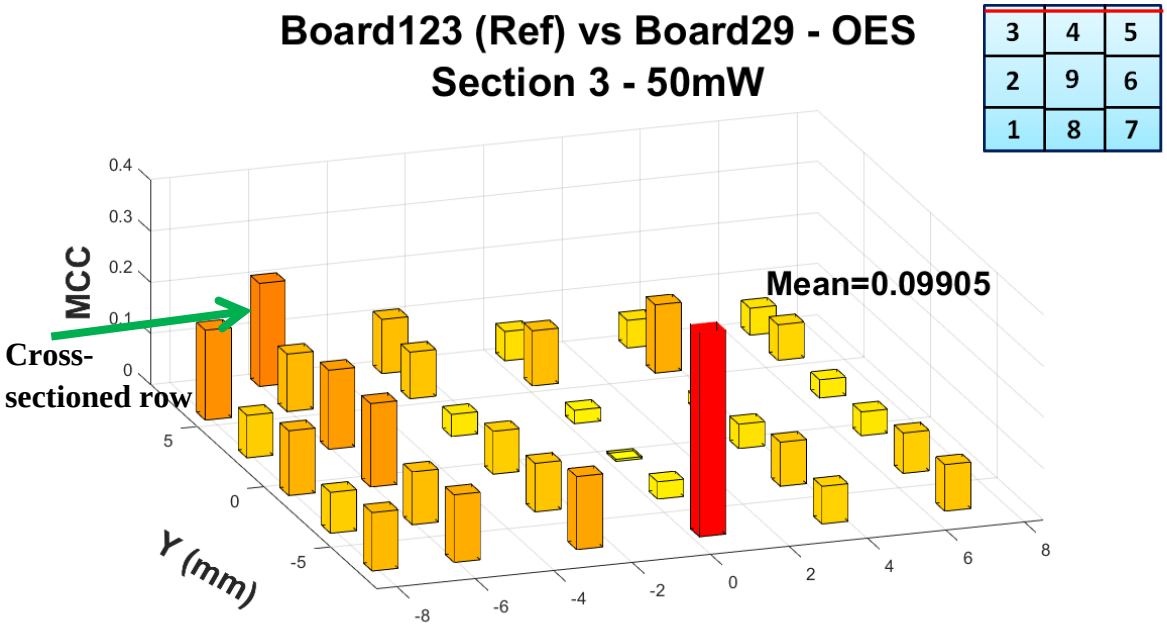

Figure 5.35: MCC graph from board #29, section 3. The line across the diagram in the top right corner shows location of cross-section cut

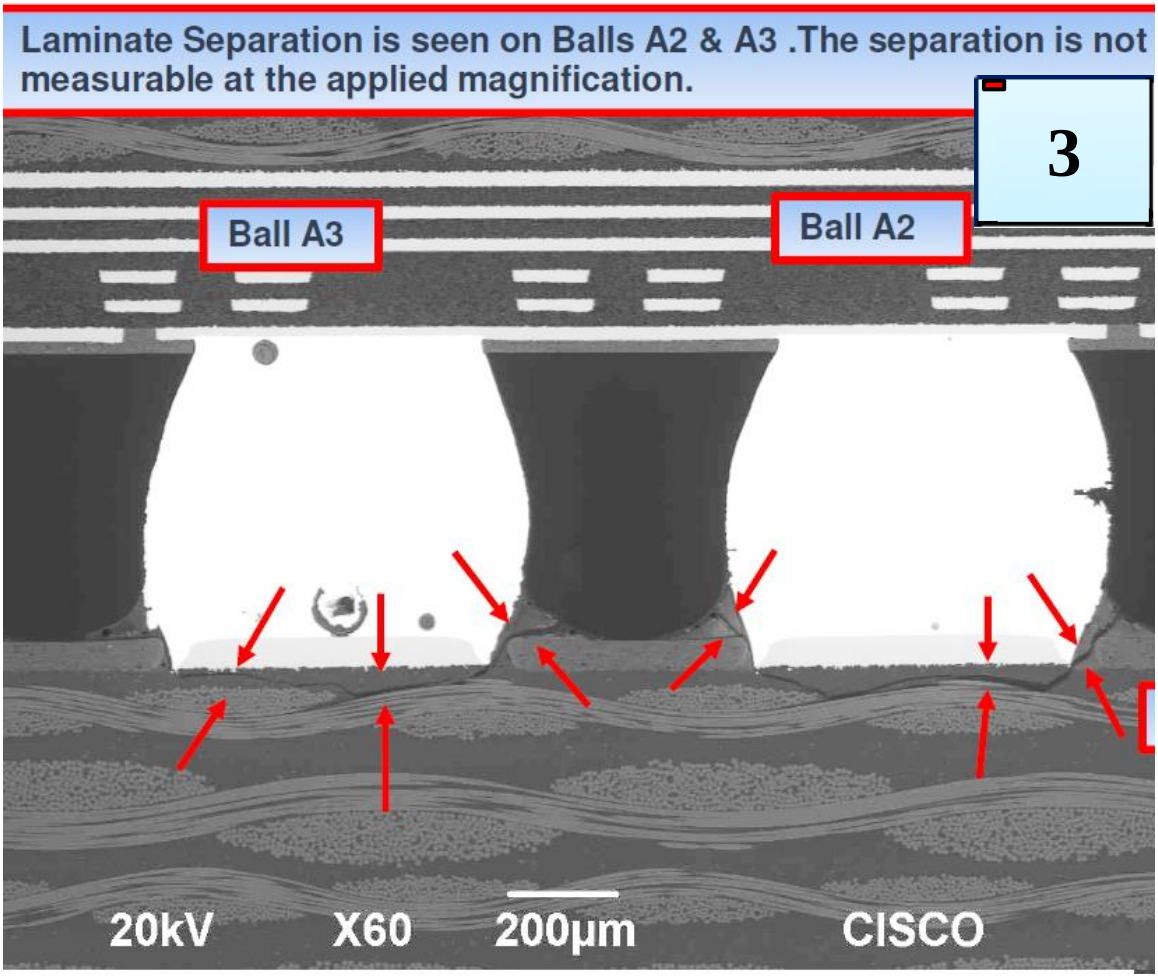

Figure 5.36: SEM of two solder balls in section 3 of board #29. Location of solder balls indicated by marker in the diagram at top right. The laminate separation correlates well to LUI results

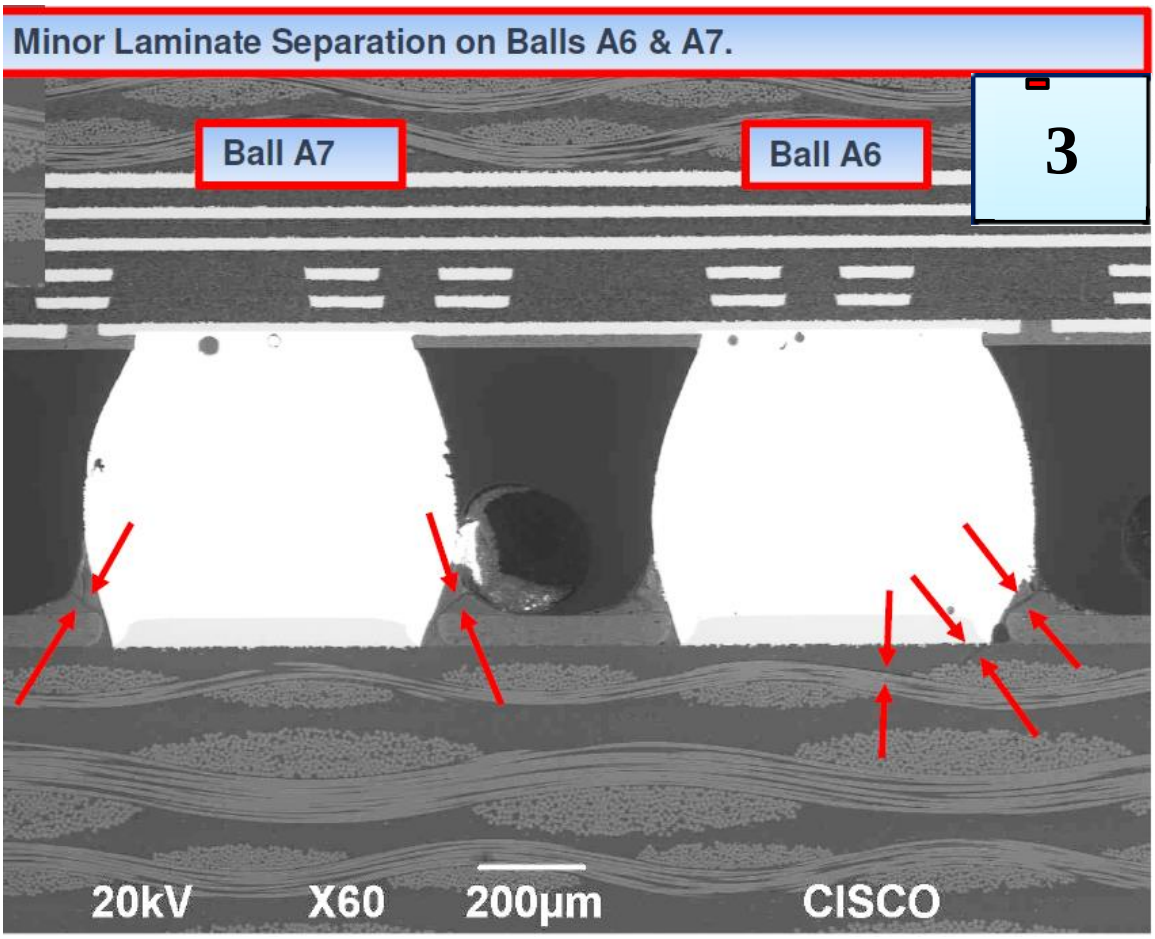

Figure 5.37: SEM of two solder balls in section 3 of board #29. Location of solder balls indicated by marker in the diagram at top right. Minor laminate separation correlates well to the decreased MCC values as compared to LUI results for balls A2 and A3

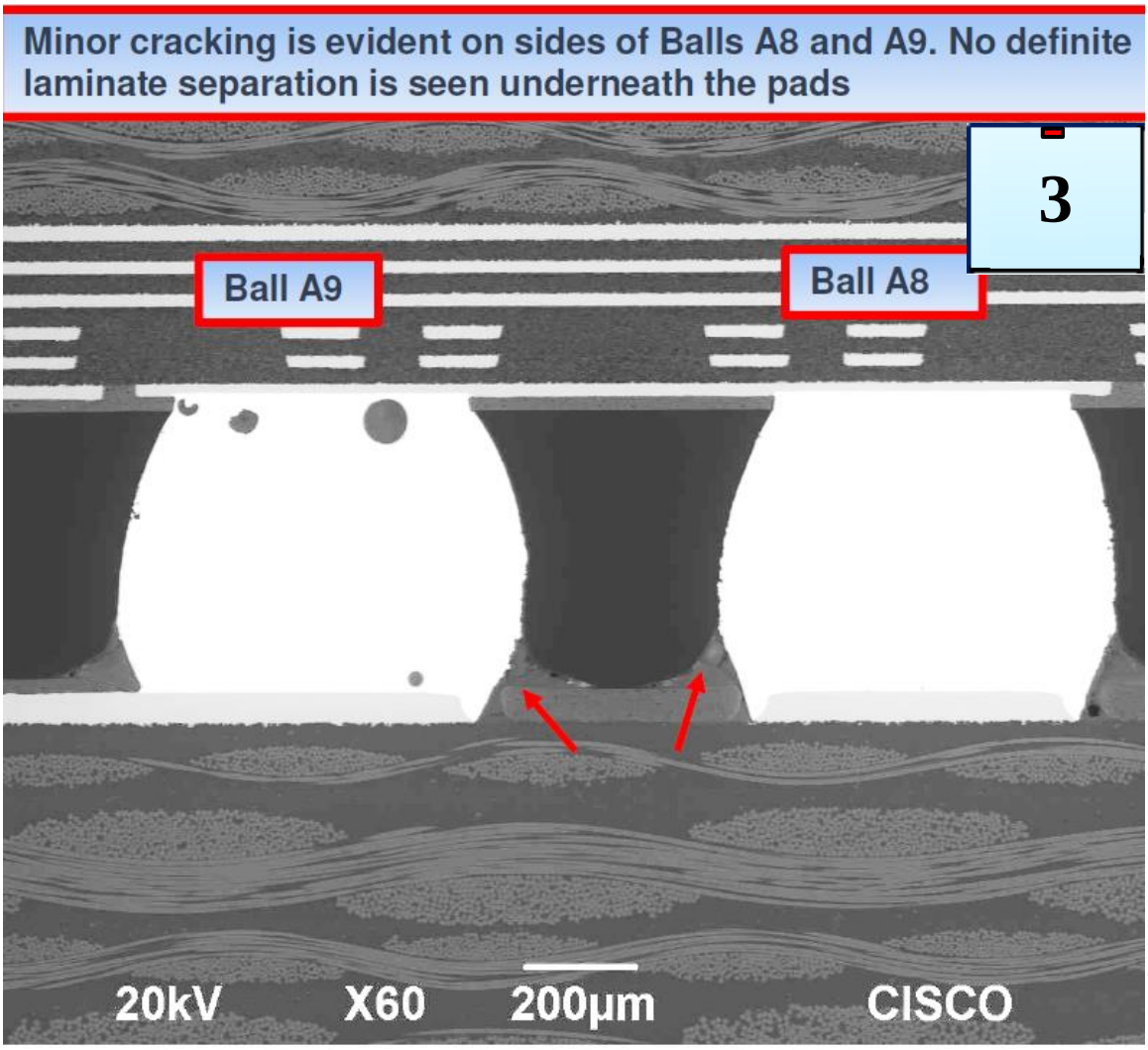

Figure 5.38: SEM of two solder balls in section 3 of board #29. Location of solder balls indicated by marker in the diagram at top right. Minor cracking correlates well to the LUI results

Figure 5.39 shows the LUI results of section 4 of board #29. The figure shows all low MCC values and, as expected, the SEM of the cross-section did not reveal any cracking or laminate separation.

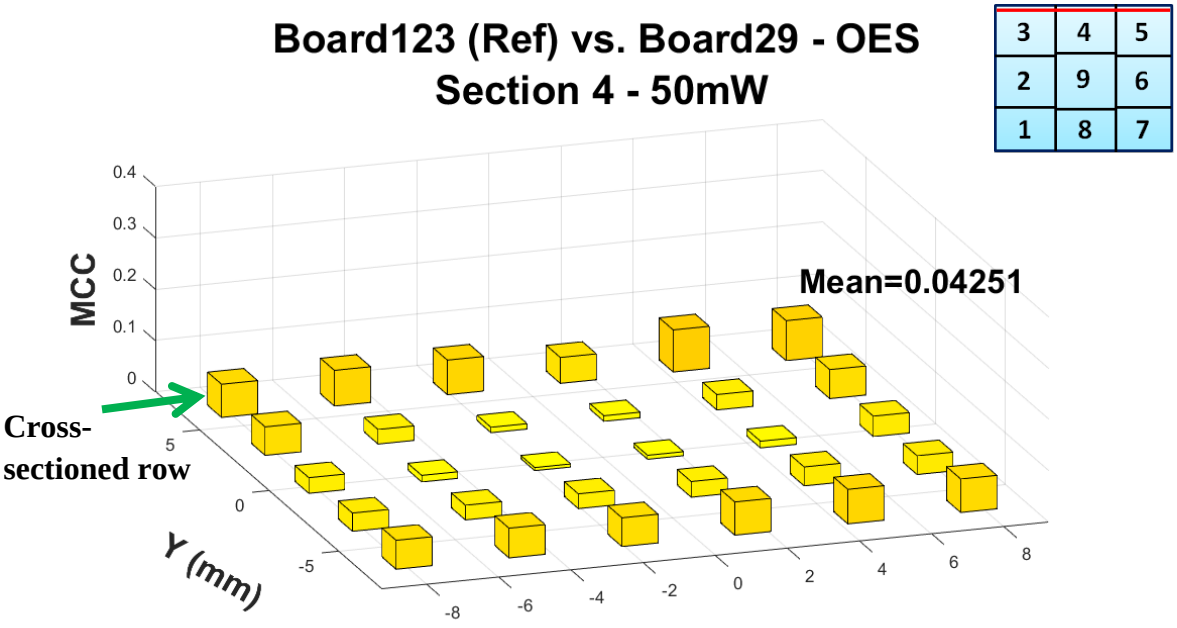

Figure 5.39: MCC graph from board #29, section 4. The line across the diagram in the top right corner shows location of cross-section cut

LUI of section 5 revealed very high MCC values throughout the area, and a large degree of cracking and laminate separation was expected. This was confirmed by the SEM of the cross-section. Note that the leftmost inspection point, corresponding to solder balls A35 – A37, has a lower MCC value than the rest. This is not surprising as the SEM showed more minor problems for these balls then for the rest. Serious laminate separation of the solder balls was found along the remainder of the cross-section.

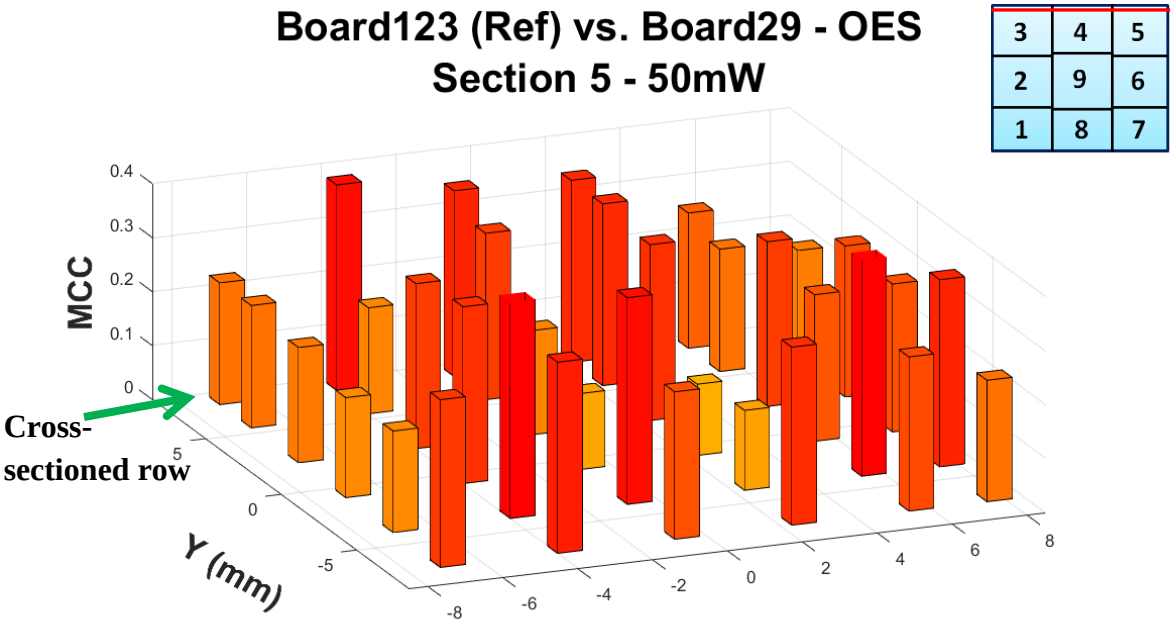

Figure 5.40: MCC graph from board #29, section 5. The line across the diagram in the top right corner shows location of cross-section cut

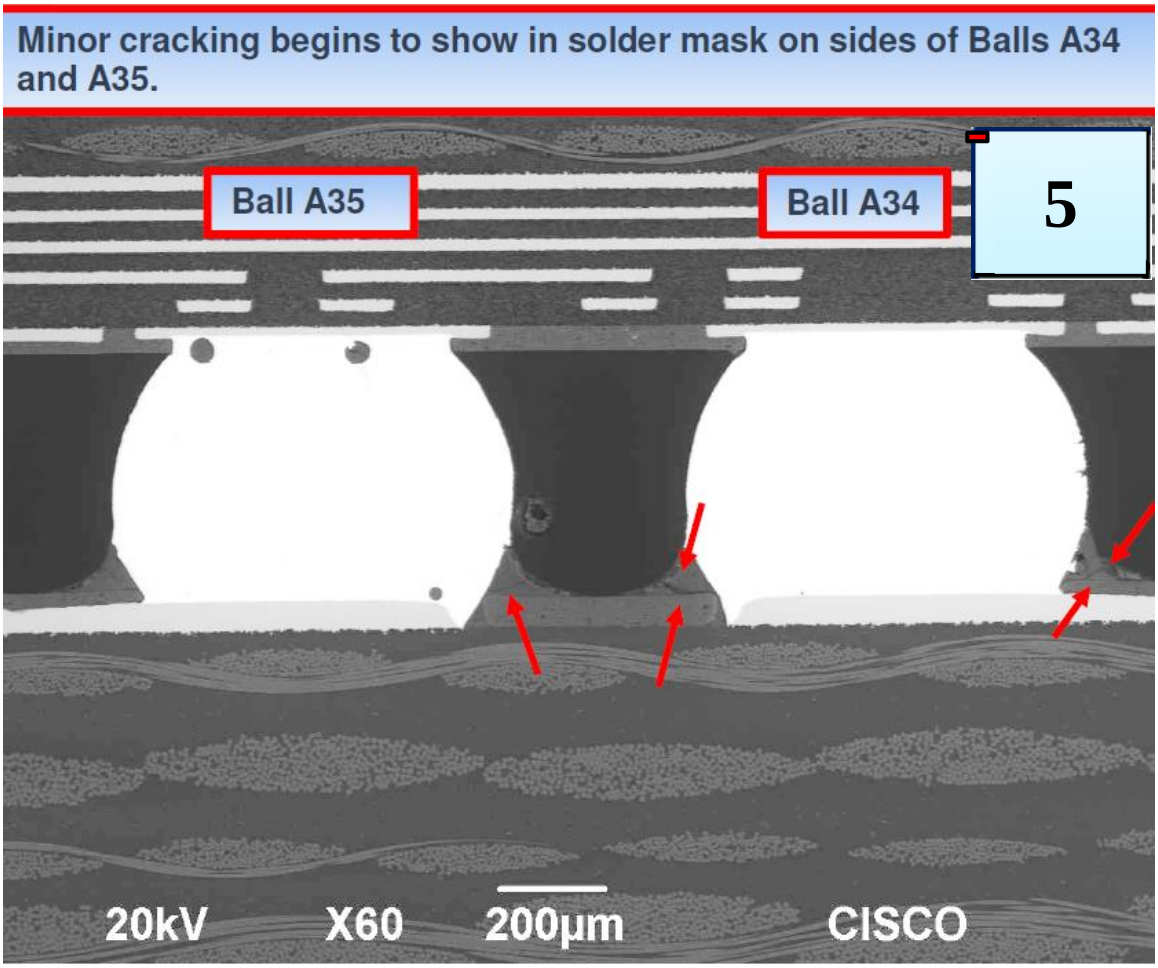

Figure 5.41: SEM of two solder balls in section 5 of board #29. Location of solder balls indicated by marker in diagram at top right. Minor cracking correlates well to the LUI results

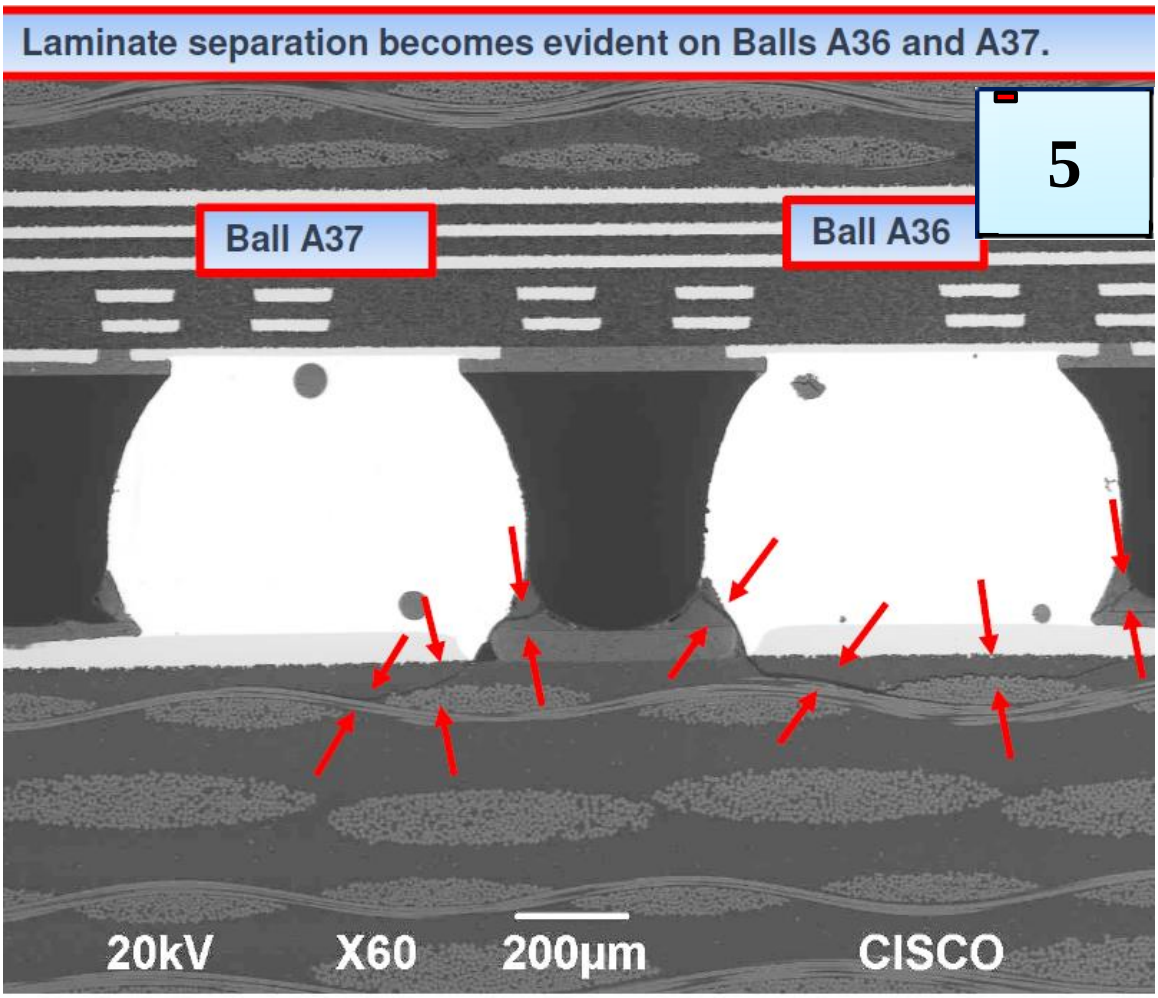

Figure 5.42: SEM of two solder balls in section 5 of board #29. Location of solder balls indicated by marker in diagram at top right. Moderate laminate separation correlates well to the LUI results

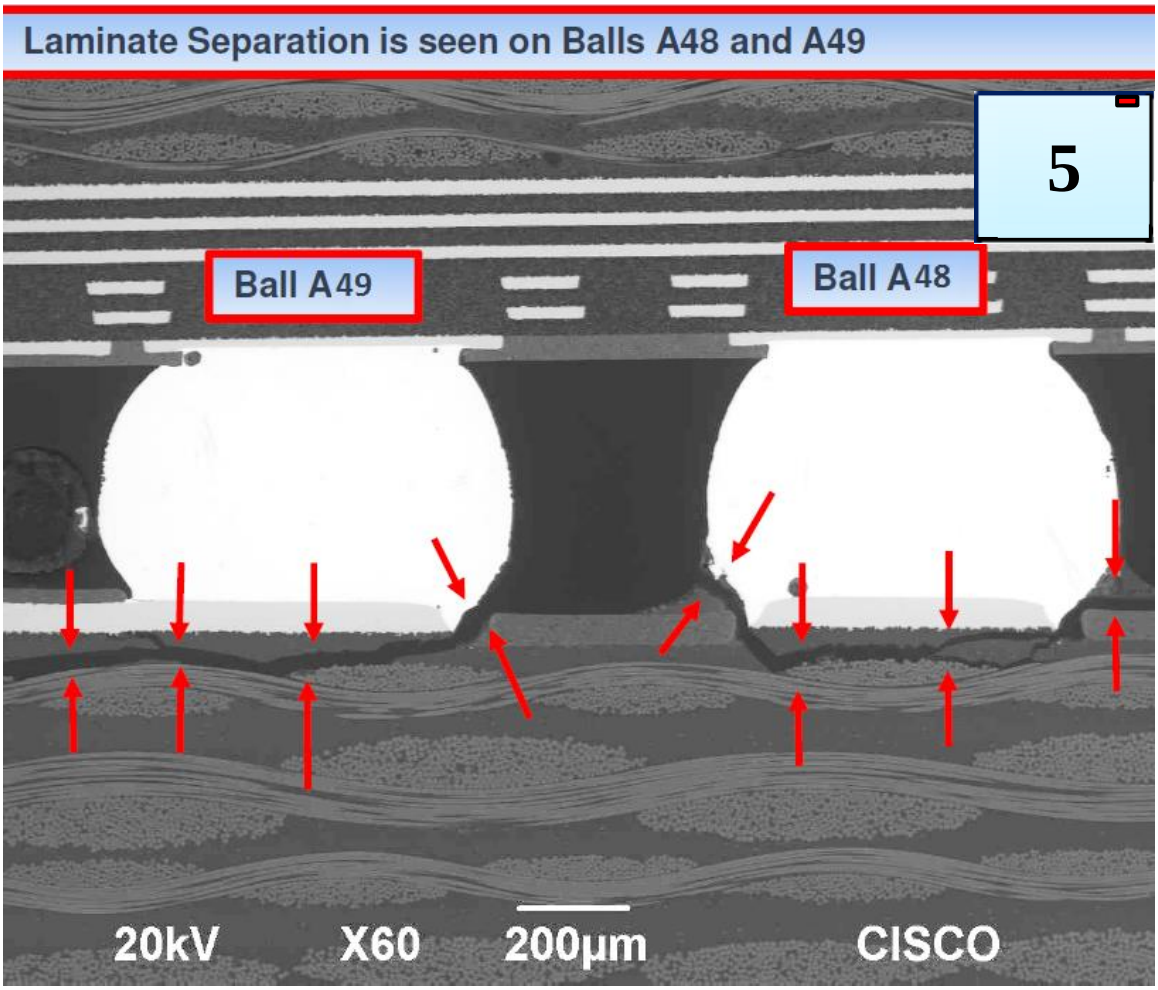

Figure 5.43: SEM of two solder balls in section 5 of board #29. Location of solder balls indicated by marker in diagram at top right. The laminate separation correlates well to the LUI results

In the cross-sectional SEM analysis of sections, 3, 4, and 5 of board #29, cracks and laminate separation were found that correlated well with the LUI results obtained. One inspection point in section 3 had a low MCC value even though SEM of the cross-section revealed some evidence of cracking. This slight discrepancy is thought to be due to inadequate excitation energy used in the inspection resulting in ultrasounds of insufficient strength to properly detect the minor crack formation.

5.6.2 LUI and cross-section results for board #3

For board #3, DES was used to allow for a higher excitation power to insure generation of ultrasounds of sufficient strength. CISCO labeled this board to have undergone a 3-point bend test. Table 5.7 shows the experimental parameters for this inspection. The results for the LUI and SEM are shown Figures 5.44-5.53.

Table 5.7: Experimental parameters for LUI of CISCO board #3

Parameter / Experiment	Total Laser Power (mW)	Sampling rate (MS/s)	# of samples	Signals average per inspection point
Board #3	80	50	3000	128

The MCC graph for section 3 is shown in Figure 5.44 Laminate separations of upwards of 150um (0.006in) were measured by SEM, and are shown in Figures 5.45 and 5.46, correlating well with the extremely high MCC values across the entire area.

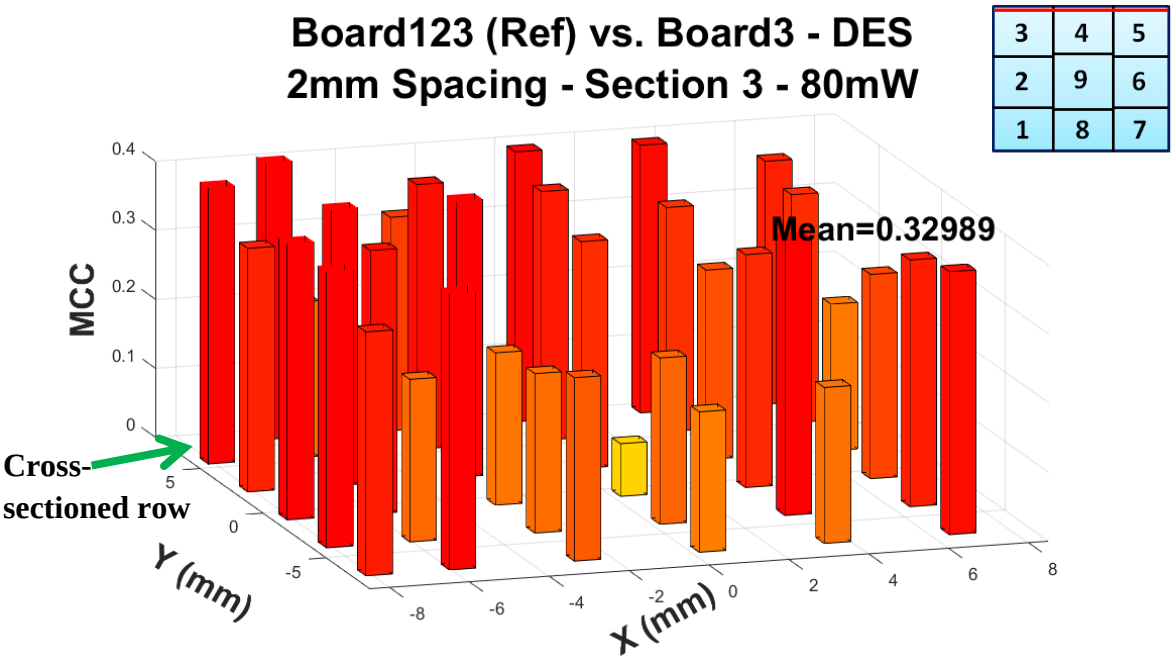

Figure 5.44: MCC graph from board #3, section 3. The line across the diagram in the top right corner shows location of cross-section cut

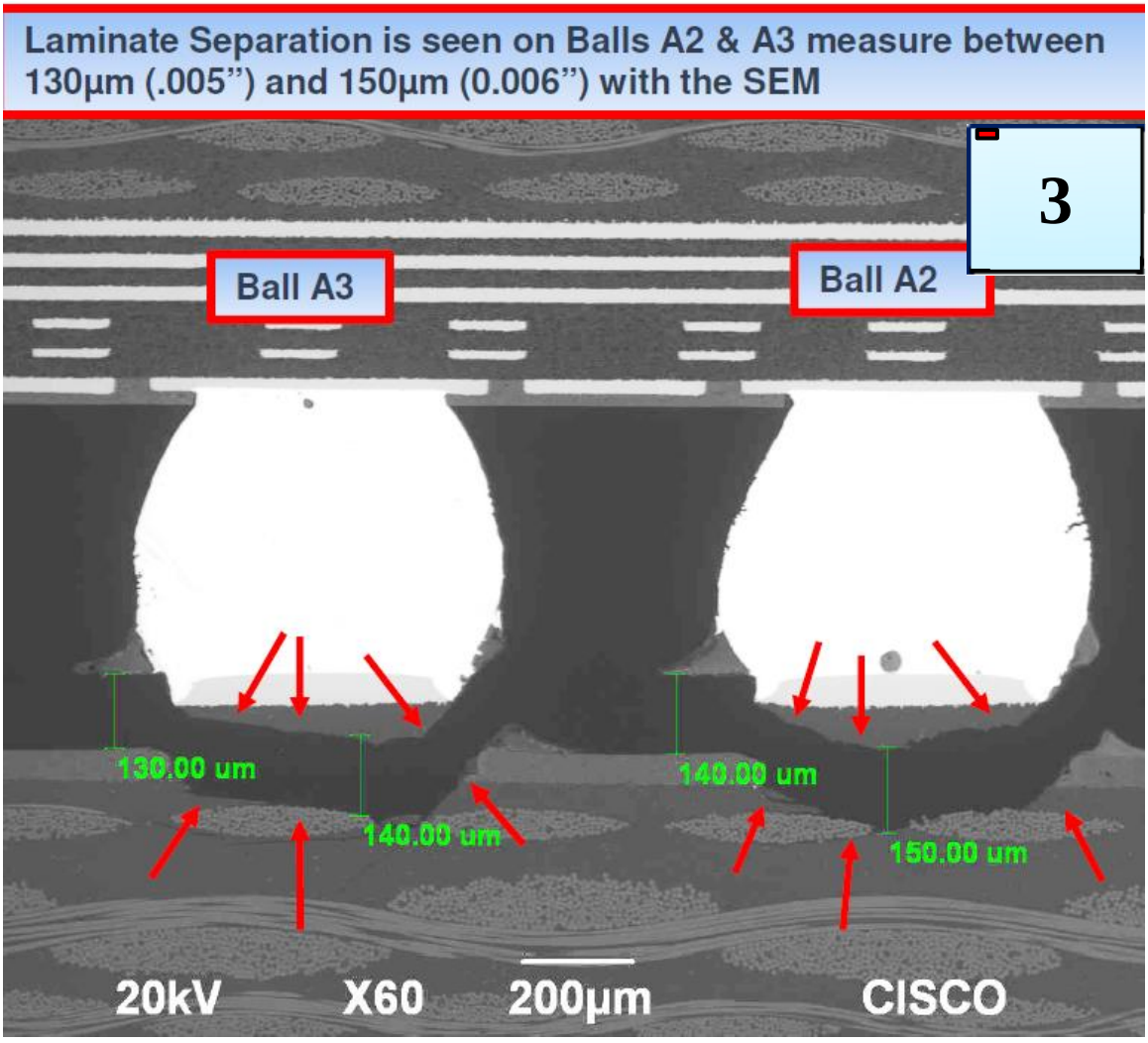

Figure 5.45: SEM of two solder balls in section 3 of board #3. Location of solder balls indicated by marker in the diagram at top right. Major laminate separation correlates well to very high MCC values for the area

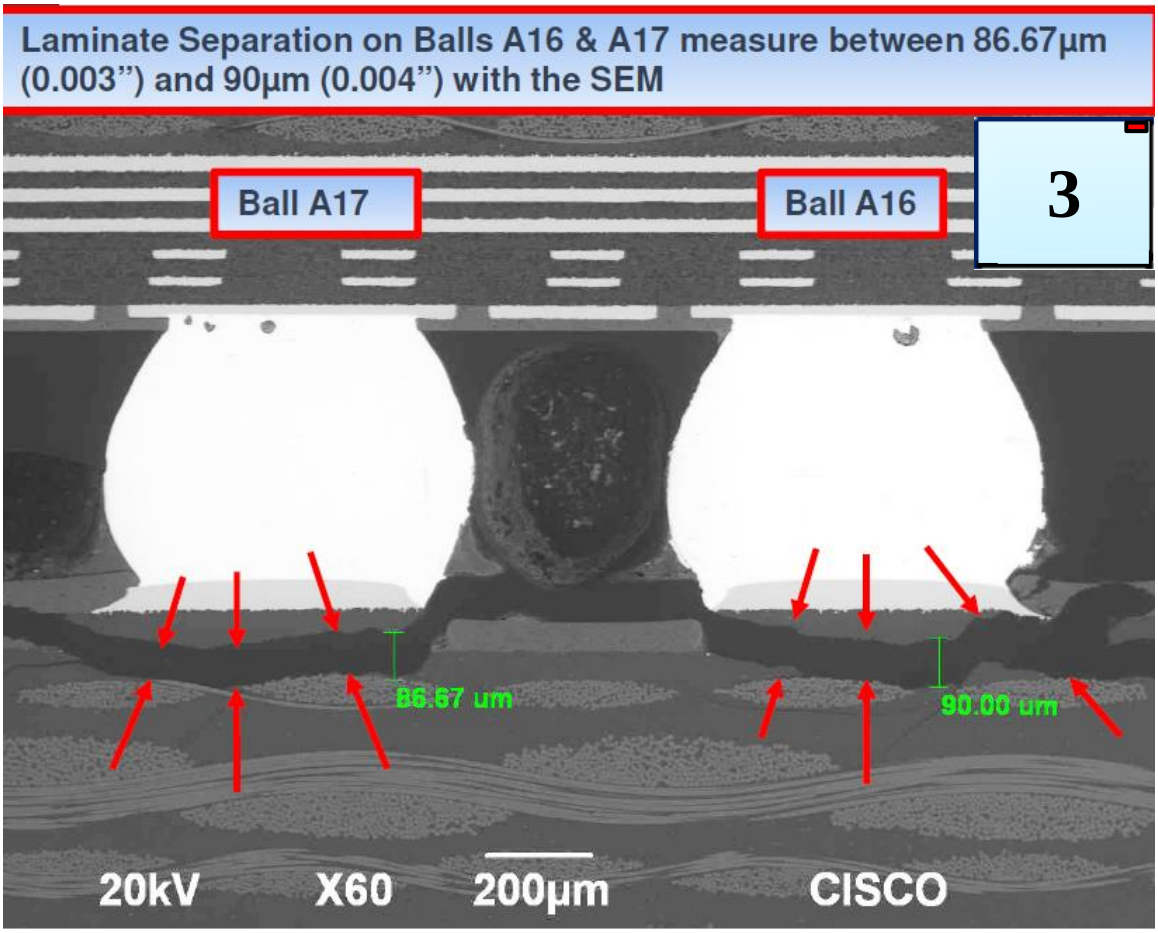

Figure 5.46: SEM of two solder balls in section 3 of board #3. Location of solder balls indicated by marker in the diagram at top right. The laminate separation reduces slightly correlating well to slightly lower MCC values for the area than solder balls A2 and A3

As shown in Figure 5.47, moving from left to right on section 4 revealed a decreasing trend in the MCC values. This trend matched with the results from the SEM, which showed the degree of laminate separation diminishing over the same area. Figure 5.48 shows the solder balls corresponding to the rightmost inspection point of section 4. Some laminate separation is seen for ball A34 while minimal cracking on only one side of ball A35 is observed. This reduced damage correlates with the lower MCC value seen this point as compared to the rest of the section.

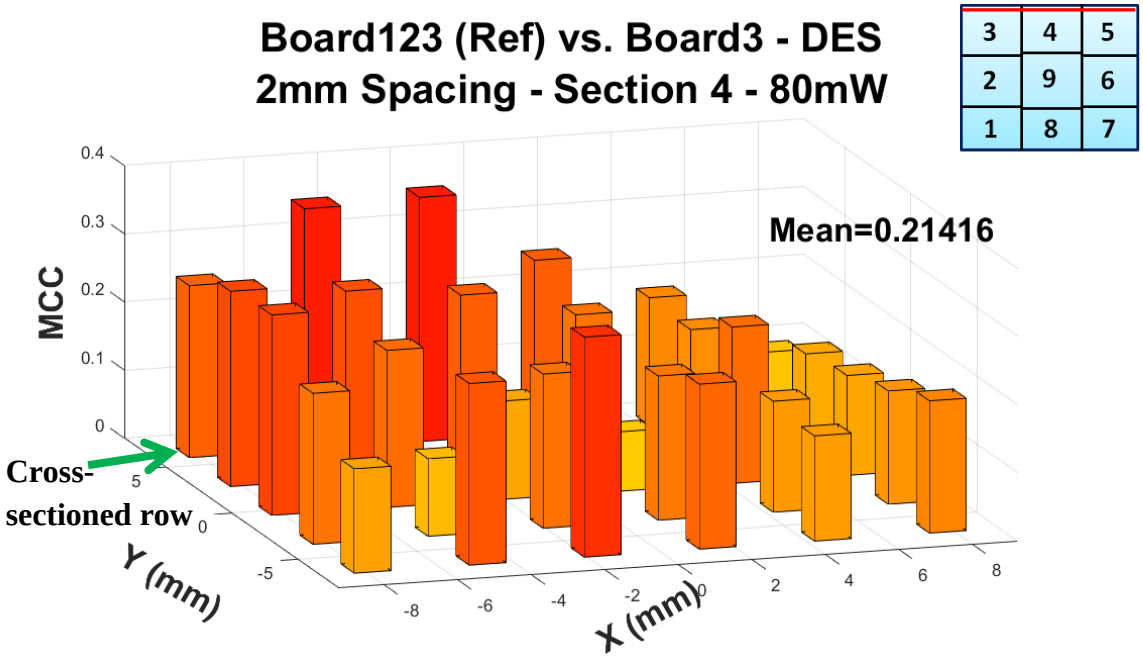

Figure 5.47: MCC graph from board #3, section 4. The line across the diagram in the top right corner shows location of cross-section cut

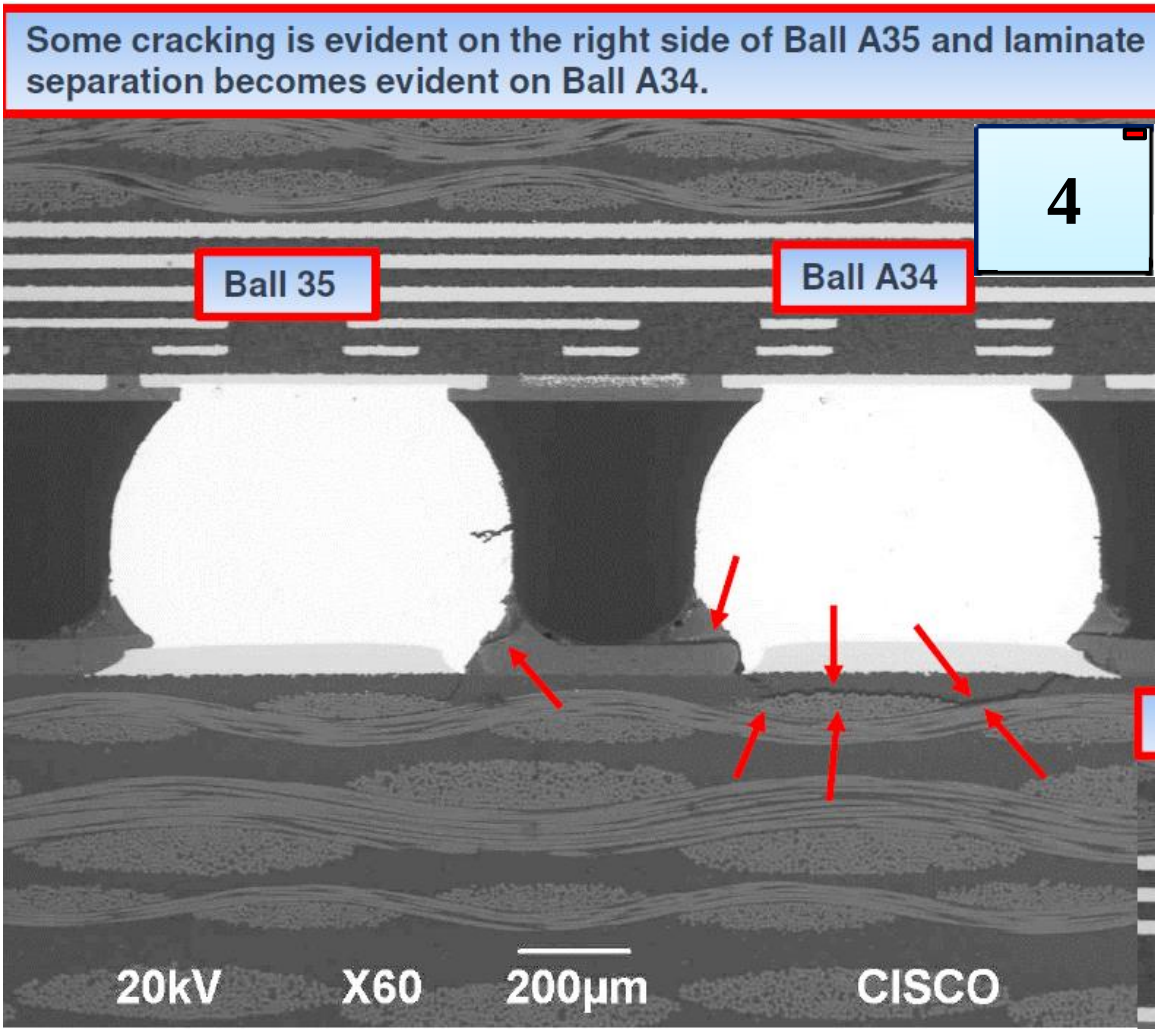

Figure 5.48: SEM of two solder balls in section 4 of board #3. Location of solder balls indicated by marker in the diagram at top right. Degree of laminate separation decreases approaching the right side of the section. This correlates well to the decreasing trend in MCC values

LUI results for section 5, shown in Figure 5.49, revealed low MCC values for the first two points, slight increase for the third point, and rising to high MCC values by the rightmost point. As seen in Figure 5.50, no cracking or laminate separation was seen for the solder balls A36 and A37, which belong to the area of the first two inspection points. The same was noted for the remaining solder balls at these locations. The slight increase

in MCC values for the third inspection point correlates to observed crack formation in solder ball A45. The laminate separation observed in the SEM for solder balls A48 – A50, shown in Figures 5.51 – 5.53, accounts for the sharp rise in the MCC value for last inspection point.

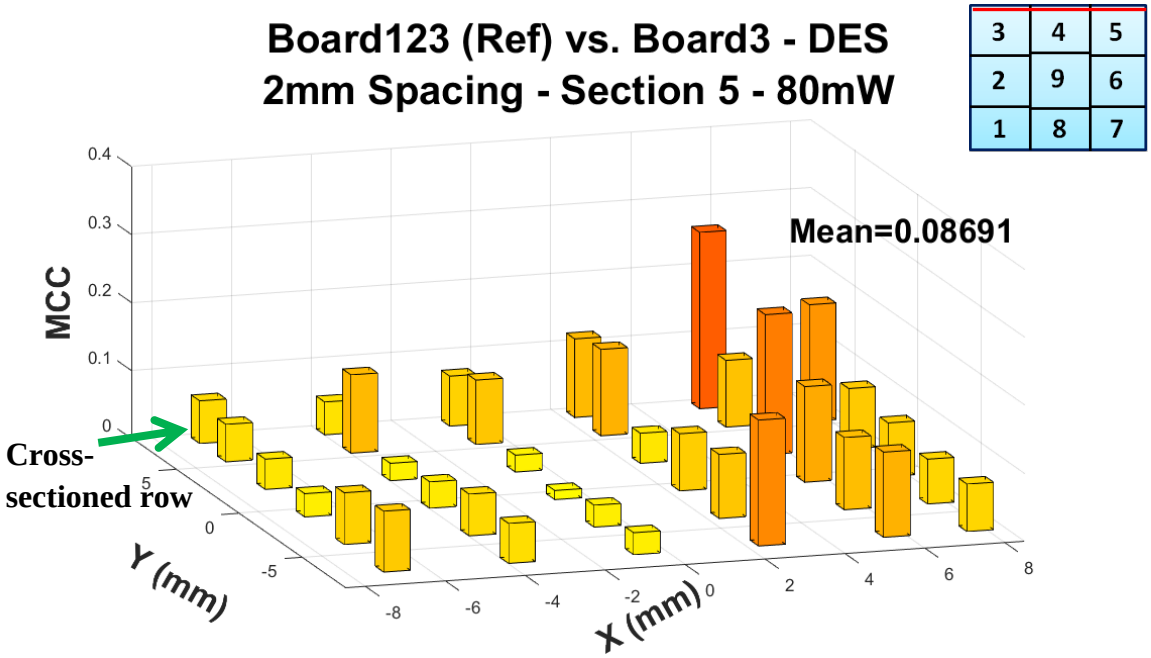

Figure 5.49: MCC graph from board #3, section 5. The line across the diagram in the top right corner shows the location of cross-section cut

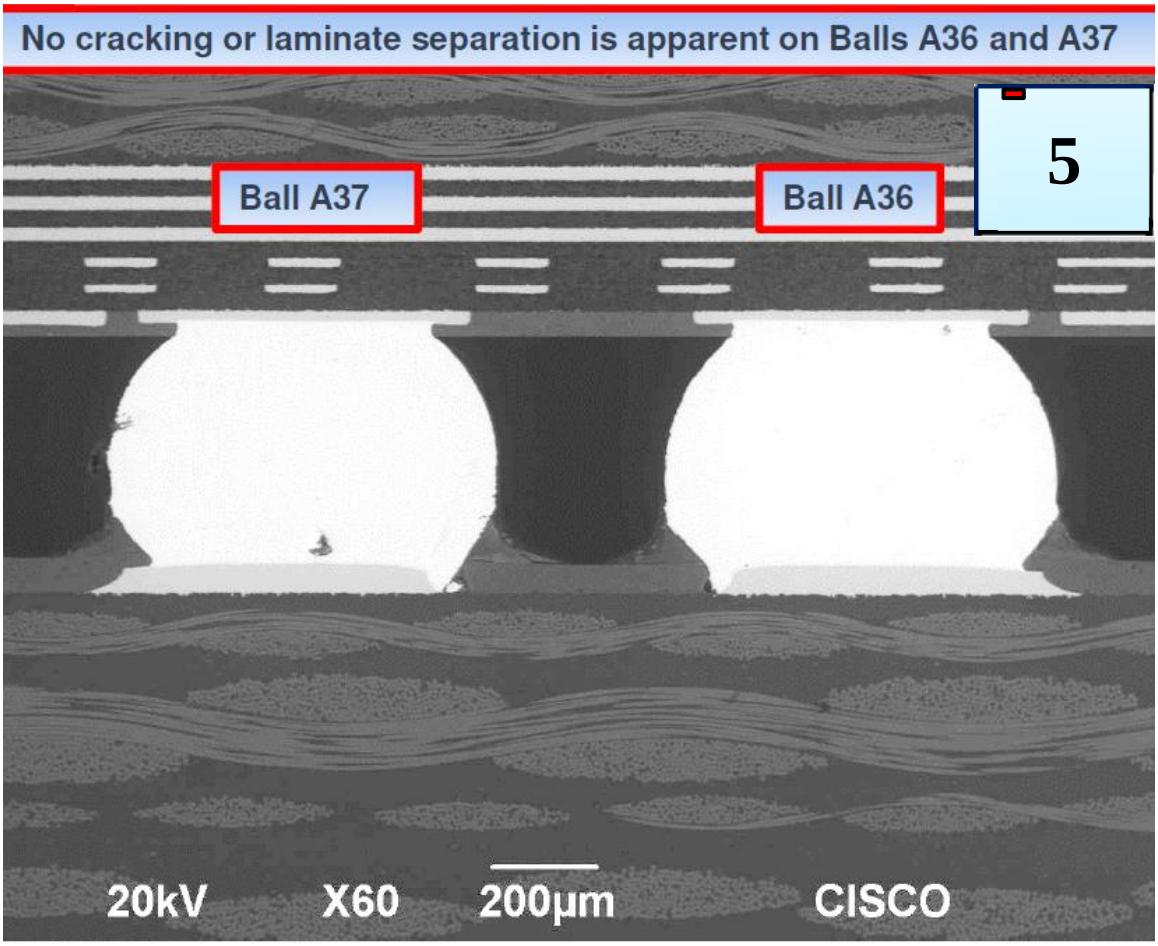

Figure 5.50: SEM of two solder balls in section 5 of board #3. Location of solder balls indicated by marker in the diagram at top right. Absence of laminate separation or cracking correlates well to the LUI results

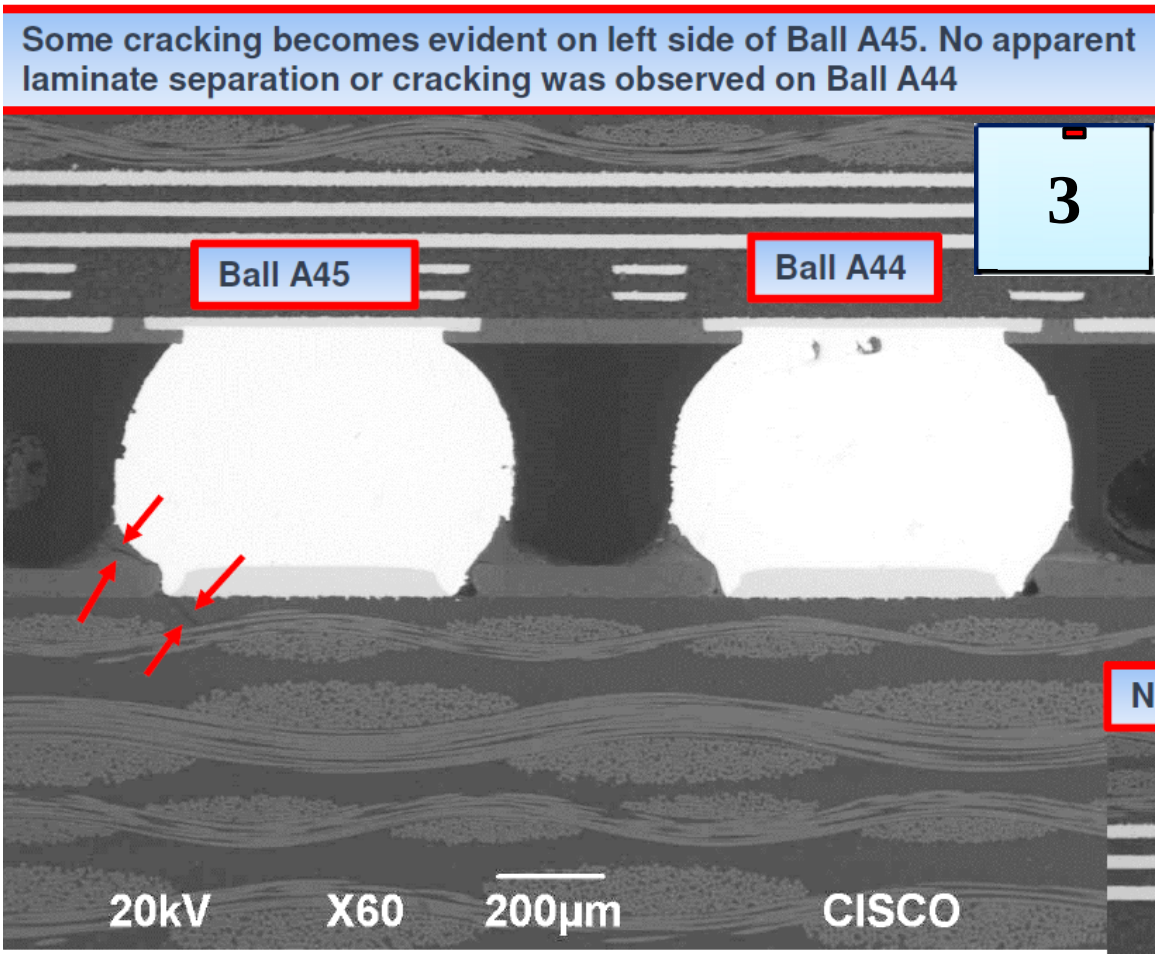

Figure 5.51: SEM of two solder balls in section 5 of board #3. Location of solder balls indicated by marker in the diagram at top right. A small amount of cracking is observed and correlates well to the increase in MCC value

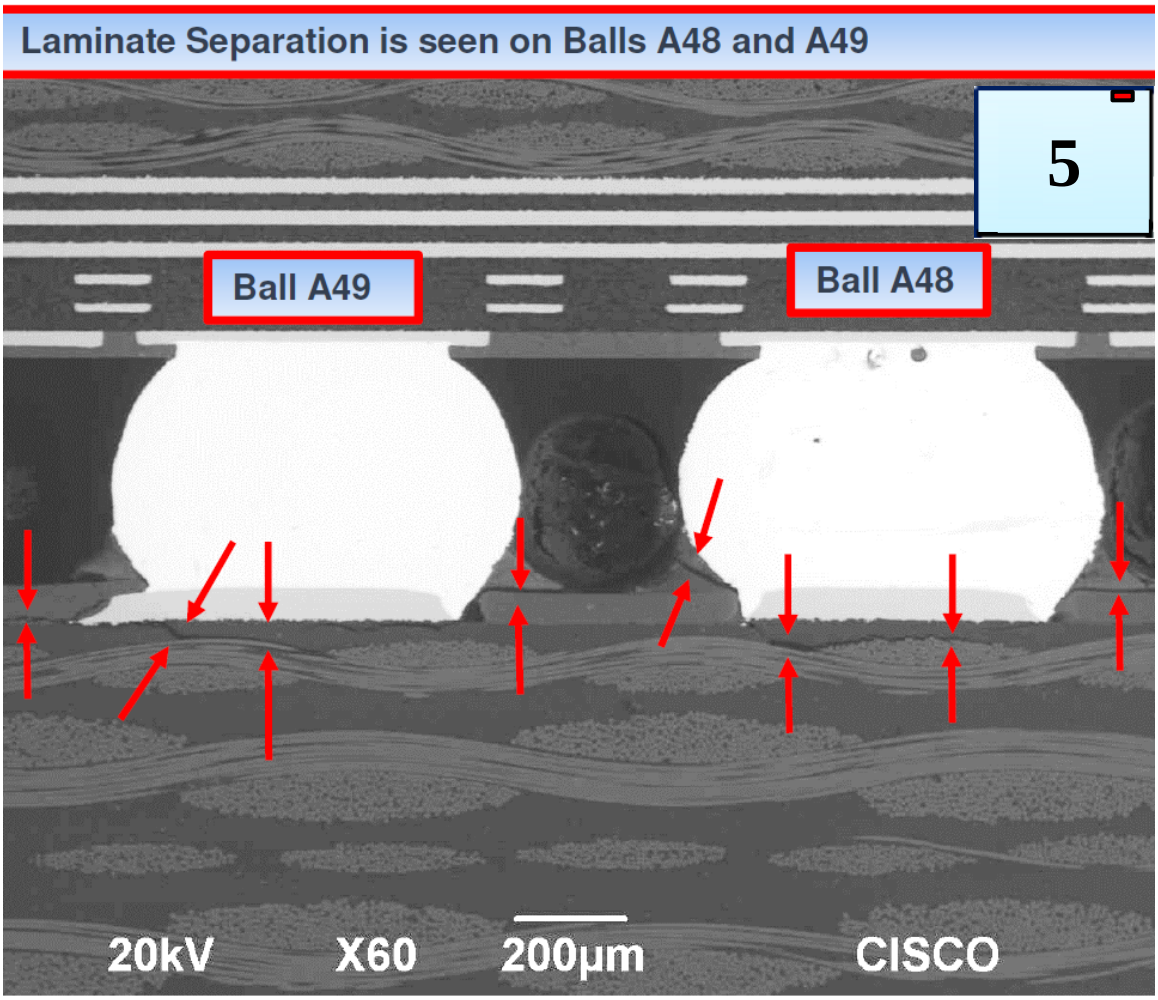

Figure 5.52: SEM of two solder balls in section 5 of board #3. Location of solder balls indicated by marker in the diagram at top right. Laminate separation of these balls correlates well to the spike in MCC value

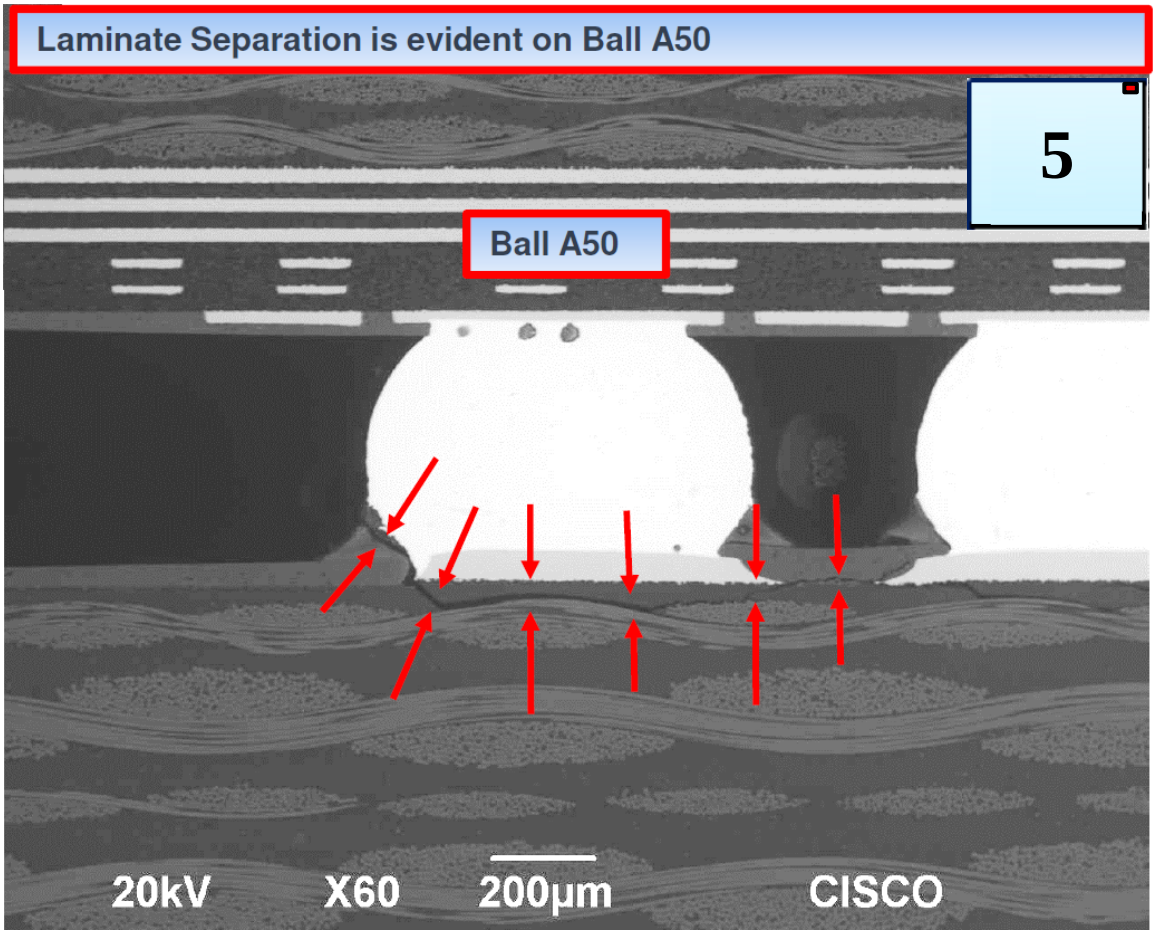

Figure 5.53: SEM of solder ball in section 5 of board #3. Location of solder ball indicated by marker in the diagram at top right. Laminate separation of this ball correlates well to the spike in MCC value

CHAPTER 6
CONCLUSION

The achievement of the research goals of this project has resulted in the development of a dual fiber array LUI system capable of increased flexibility in the size of chip packages it can inspect. The long term goal of this research is the development of a robust, low-cost non-destructive laser ultrasonic inspection system for evaluation of solder joint quality in microelectronic chip packages. The safety and performance of the system has been improved through hardware upgrades and software improvements. Various tests were conducted to evaluate the benefits derived from the improvements. Experiments were conducted on a new FCBGA from CISCO to determine the suitability of the system to inspect the package. The LUI results and corresponding SEM images for the cross-sectioned portions of board #29 and #3, show that the two correlate very well. More severe cracks and laminate separation correlated to high MCC values, while areas with solder balls absent of defects had correspondingly low MCC values. Therefore, from this analysis it can be seen that the new fiber array LUI system was able to accurately determine areas with defects in the new CISCO FCBGA package.

6.1 Summary of Important Contributions

(1) A laser multiplexer system was integrated into the existing LUI system. The multiplexer splits the beam coming from the laser and couples each beam into its own

fiber optic cable. As a result, the new system is capable of dual excitation points, which allows for stronger ultrasonic vibrations to be introduced. Additionally, smaller diameter fiber cores can now be used because the energy through each fiber is now half of what it might have been. The consequence of decreased core diameter is reduced minimum bend radii. This is important commercially, as it allows the system to be more compact.

(2) The implementation of rotational stages allows either single or multiple excitation points to be used during the inspection. Multiple excitation points allowed the entire FCBGA to be analyzed without the need to move the excitation points during the inspection. This was impossible with a single excitation point. The result of this is greater flexibility in the types of chip packages which can be inspected by the system as well as greater throughput.

(3) A collision prevention system for the end effectors and interferometer probe was designed and implemented. This system makes use of Hall Effect sensors to detect the proximity of magnets mounted on the end effectors. When the intensity of the magnetic field is too high (i.e. when the end effectors are too close to the interferometer probe), power to the system is cut. Collision prevention is of the utmost importance, as the impact from a crash results in multiple hours of system downtime while damage is assessed and calibration performed. Previously the system had only a laser tripwire which would prevent the Arcus stage from driving the end effectors into the interferometer

probe. However, this did nothing to prevent the sample positioning stage from causing such a crash. The new Hall Effect system protects against both avenues of collisions.

CHAPTER 7
RECOMMENDATIONS FOR FUTURE WORK

The improvements made to the system as part of this research open up many new avenues of investigation. Some potential areas are presented in this chapter.

7.1 Effect of Excitation Spot Size on Inspection Results

The new adjustable collimators increase the range of possible excitation spot sizes. In turn, this allows the experimenter to vary the energy density used to induce the ultrasonic vibrations. To better understand the benefits/disadvantages of a particular energy density, future work could be performed in which devices with known defects would be inspected with differing energy densities and the results cross compared. This would allow future experimenters to quickly decide on an energy density for a particular inspection that is most likely to produce accurate results.

7.2 Finite Element Analysis of Chip Excitation with Multiple Points

It has been hypothesized that multiple excitation points are likely to generate new, higher frequency vibrational modes [7]. These high frequency modes are very sensitive to defects that might otherwise not be detected [7]. Finite Element Analysis (FEA) could be used to predict the effect of dual excitation points as well as the effect the excitation point spacing might have on the vibrational response. Additionally, multiple excitation points

would induce more intense interference patters throughout the chip, which might interfere with defect detection at the areas of destructive interference. FEA would give clues as to the degree this might negatively impact the results, and experimental tests could be conducted to confirm this.

7.3 Sensitivity Studies with Increased Laser Power

In order to validate the findings of the FEA mentioned above, a series of experiments would need to be conducted to test the sensitivity of the new fiber array system to very small defects. This could be done by inducing defects of varying sizes and using the system to try to detect them. For example, a set of identical boards could be divided into groups and all but one group would be subject to a different severity of bend test (either varying the maximum deflection or number of cycles). The reserved group would be used to generate the reference signals. After each successive round of bending, the boards would be inspected with the fiber array system using a range of excitation energies, and the results would be compared to check for any difference in the MCC values. Additionally, a set of inspections would be conducted with a single excitation point. Cross-sectioning would be used to confirm the LUI results. If using higher energy levels and dual excitation points allow cracks/ laminate separation to be detected which were not observed when using the single excitation point, it would confirm the generation of higher frequency modes.

REFERENCES

[1] Li, Y., C.P. Wong, and D. Lu, 2009, *Electrical Conductive Adhesives with Nanotechnologie,* Springer.

[2] Tummala, R. R., Rymaszewski, E. J., and Klopfenstein, A. G., 1997, *Microelectronics Packaging Handbook: Semiconductor Packaging, Part II,* 2nd edition Kluwer Academic Publishers, Boston,.

[3] Harper, C. A., 2000, *Electronic Packaging and Interconnection Handbook,* 3rd edition, McGraw-Hill, New York.

[4] 2005, "Flip Chip Ball Grid Array Package Reference Guide" Texas Instrument's. Literature number: SPRU811A.

[5] Harper 1.51.

[6] K. Kotaka, Y. Abe, and Y. Homma, "The new underfill materials with high adhesion strength for flip-chip applications," 2nd 1998 IEMT/IMC Symposium (IEEE Cat. No.98EX225), Tokyo, Japan, 1998, pp. 369-373. doi:10.1109/IEMTIM.1998.704703

[7] Gong, J. 2014, "Quality Assessments of Solder Bump Interconnections in Ball Grid Array Packages Using Laser Ultrasonics And Laser Interferometer", Ph.D. Dissertation, Dept. of Mechanical Engineering, Georgia Institute of Technology.

[8] NPX Semiconductor, Inc. 2015, "Wafer Level Chip Scale Package (WLCSP)", Document Number: AN3846, from https://www.nxp.com/docs/en/applicationnote/AN3846.pdf

[9] Harper, 10.41.

[10] Ivankovic, A., 2015, "The (r)evolution of wafer-level packages", Chip Scale Review, vol. 19(6), pp. 4-7.

[11] A. C. Mackie, 2011, "Solder in the Age of 3D Semiconductor Assembly", Chip Scale Review, vol. 15(6), pp. 25-28.

[12] W. C. Lo et al., 2007, "3D Chip-to-Chip Stacking with Through Silicon Interconnects" 2007 International Symposium on VLSI Technology, Systems and Applications (VLSI-TSA), Hsinchu, pp. 1-2. doi: 10.1109/VTSA.2007.378925

[13] G. Patti., 2014, "3D Stacked ICs: From Vision to Volume", Chip Scale Review, vol. 18(6), pp. 32-35.

[14] P. Ramm, et al., 1997, "Three dimensional metallization for vertically integrated circuits, " Microelectron. Eng., Vol. 3738, pp.39-47.

[15] K. Takahashi, et al., 2001, "Current Status of Research and Development for Three-Dimensional Chip Stack Technology," Jpn. J. Appl. Phys., Vol. 40, No.4, pp.3032-3037.

[16] J. Barton, et al, 2003, "Development of Distributed Sensing Systems of Autonomous Micro-Modules" Proc 53rd Electronic Components and Technology Conf, New Orleans, Louisiana, pp. 1147-1152.

[17] W. C. Lo, et al., 2006, “An innovateive Chip-to-Wafer and Wafer-to-Wafer Stacking," Proc 57th Electronic Components and Technology Conf., pp. 337-342.

[18] Ellis, T. W., 2001, "Bond Integrity: Trade-Offs Between Electrical, Thermal and Mechanical Performance," Chip Scale Review, vol. 5(5).

[19] Harper, 8.72

[20] Hao, Xianmin, Yongcong, Gaofei, and Hongwei., 2013, Solder joint inspection based on neural network combined with genetic algorithm. Optik - International Journal for Light and Electron Optics, vol. 124(20), pp. 4110-4116.

[21] Maisl, M., Porsch, F., and Schorr, C., 2010, "Computed laminography for x-ray inspection of lightweight constructions." 2nd International Symposium on NDT in Aerospace.

[22] Krastev E, B.D., 2010, Modern 2D / 3D X-Ray Inspection - Emphasis on BGA, QFN, 3D Packages, and Counterfeit Components. in *SMTA Pan Pacific Symposium*.

[23] Canumalla, S., Resolution of broadband transducers in acoustic microscopy of encapsulated ICs: transducer selection. Components and Packaging Technologies, IEEE Transactions on, 1999. 22(4): p. 582-592.

[24] Chan, Y.C., K.C. Hung, and X. Dai, Nondestructive defect detection in multilayer ceramic capacitors using an improved digital speckle correlation method with wavelet packet noise reduction processing. Advanced Packaging, IEEE Transactions on, 2000. 23(1): p. 80-87

[25] Yuan, C. and L. Ping. The “popcorn effect” of plastic encapsulated microelectronic devices and the typical cases study. in Quality, Reliability, Risk, Maintenance, and Safety Engineering (ICQR2MSE), 2011 International Conference on. 2011.

[26] Guojun, H., et al., Numerical and Experimental Study of Interface Delamination in Flip Chip BGA Package. Journal of Electronic Packaging, 2010. 132(1): p. 011006-7.

[27] Zhang, L., Ume, C., Gamalski, J., and Galuschki, K. P., 2006, "Detection of flip chip solder joint cracks using correlation coefficient and auto-comparison analyses of laser ultrasound signals," IEEE Transactions on Components and Packaging Technologies, vol. 29(1) pp. 13-19.

[28] Teramoto, A., Murakoshi, T., Tsuzaka, M., and Fujita, H., 2007, "Automated Solder Inspection Technique for BGA-Mounted Substrates by Means of Oblique Computed Tomography," IEEE Transactions on Electronics Packaging Manufacturing, vol. 30(4), pp. 285-292.

[29] Yang, J., et al., 2010, "Board-Level Solder Joint Reliability Study of Land Grid Array Packages for RF Application Using a Laser Ultrasound Inspection System", Journal of Electronic Packaging, vol. 132(2): p. 021006.

[30] Lizheng, Z., et al., Study of Flip Chip Solder Joint Cracks Under Temperature Cycling Using a Laser Ultrasound Inspection System. Components and Packaging Technologies, IEEE Transactions on, 2009. 32(1): p. 120-126.

[31] Liu, S., Erdahl, D., Ume, C., 2001, "A Novel Approach for Flip Chip Solder Joint Quality Inspection: Laser Ultrasound and Interferometric System", *IEEE Tras on Com. And Pack. Tech*., vol 24(4).

[32] Turner, H., 2002, "Design Of an Advanced System for Inspection Of Microelectronic Devices And Their Solder Connections Using Laser-Induced Vibration Techniques" Masters Thesis, Dept. of Mechanical Engineering, Georgia Institute of Technology.

[33] Smith, V., and Do, B. T., 2008, "Bulk and surface laser damage of silica by picosecond and nanosecond pulses at 1064nm" Applied Optics, Vol. 47(26).

[34] Dixon, S., Edwards, C., Palmer, S. B., and Schindel, D. W., 1996, "Ultrasound generation in single-crystal silicon using a pulsed Nd:YAG laser," J. Phys., D, Appl. Phys., vol. 29, pp. 1345–1348.

[35] H. Sun, 2012, *Laser Diode Beam Basics, Manipulations and Characterizations* Springer

[36] Campbell, J. H., Rainer, F., Kozlowski, M., Wolfe, C. R., Thomas, I., and Milanovich, F., 1991, "Damage resistant optics for a megajoule solid-state laser," Proc. SPIE, vol. 1441, pp444-456